arXiv:0712.2733v3 [hep-ex] 1 Apr 2008

FERMILAB-PUB-08/028-E

Review of Top Quark Physics Results

R. Kehoe
Physics Department, Southern Methodist University, Dallas, Texas
Dallas, TX 75275, USA
kehoe@physics.smu.edu

M. Narain
Physics Department, Brown University
Providence, RI, 02912 USA
narain@hep.brown.edu

A. Kumar
Physics Department, State University of New York at Buffalo
Buffalo, New York 14260, USA
ashishk@fnal.gov

Received 14 December 2007
Published 12 February 2008

As the heaviest known fundamental particle, the top quark has taken a central role in the study of fundamental interactions. Production of top quarks in pairs provides an important probe of strong interactions. The top quark mass is a key fundamental parameter which places a valuable constraint on the Higgs boson mass and electroweak symmetry breaking. Observations of the relative rates and kinematics of top quark final states constrain potential new physics. In many cases, the tests available with study of the top quark are both critical and unique. Large increases in data samples from the Fermilab Tevatron have been coupled with major improvements in experimental techniques to produce many new precision measurements of the top quark. The first direct evidence for electroweak production of top quarks has been obtained, with a resulting direct determination of V_{tb}. Several of the properties of the top quark have been measured. Progress has also been made in obtaining improved limits on potential anomalous production and decay mechanisms. This review presents an overview of recent theoretical and experimental developments in this field. We also provide a brief discussion of the implications for further efforts.

Keywords: top quark; electroweak fit; fermion generations.

PACS numbers: 11.25.Hf, 123.1K

1. Introduction

The top quark has played a key role in particle physics for well over a decade. Its discovery[1,2] marks a triumph of the modern theoretical framework of $SU(3) \times SU(2) \times U(1)$ interactions. It also hallmarked a new generation of experimental approaches that will be central to the intensifying search for the Higgs boson and new physics. Subsequent analyses have measured the mass of the top quark with remarkable precision. What is more, this particle is uniquely placed to probe strong interactions, electroweak interactions, and the Higgs mechanism itself. Many challenges confront the experimentalist, particularly because of the diversity and complexity of the final state.

We review this exciting new field with the underlying goal of illustrating not only the measurements themselves, but also the techniques being developed to extract them. In the remainder of this section, we synopsize the role of the top quark within our understanding of fundamental interactions and particles. In subsequent sections we discuss production and decay expectations, as well as the experiments that study top quark events. Measurements of strong and electroweak production are reviewed in Section 4 and 5, respectively. Section 6 treats precision measurement of the top quark mass. This is followed in Section 7 with coverage of other properties of this particle. Lastly, we finish in Section 8 with searches for non-standard physics within the top quark sector and we conclude with some considerations for future efforts. There are excellent reviews of this subject which primarily cover results obtained at $\sqrt{s} = 1.8$ TeV from 1992-1996 [3,4], termed Run I of the Fermilab Tevatron. Informative reviews with a more phenomenological emphasis are also available[5,6]. We concentrate in this review on results obtained at $\sqrt{s} = 1.96$ TeV and much higher integrated luminosity in the Tevatron's Run II which started in 2001. We also make a point of including the later Run I results that may not have been completely discussed before. To provide completeness and also a better indication of the direction of the field, we include several preliminary results from CDF and DØ when published results are not yet available. As these results may change before publication, we indicate them in the text.

1.1. *Electroweak and strong interactions*

We now view the weak and electromagnetic interactions as different manifestations of the same underlying electroweak interaction. The crucial progress in this realization came with the development of a viable $SU(2) \times U(1)$ model[7]. This interaction is mediated by four gauge bosons. The $W^{\pm}$ bosons mediate the charge changing weak currents for left-handed fermions. The Z boson and the photon propagate the weak and electromagnetic neutral currents. The symmetry of the theory's Lagrangian is broken in the ground state of the system by introducing the Higgs field[8] which has a non-zero vacuum expectation value. This then provides mass to the $W^{\pm}$ and Z bosons. This model, originally designed around first and second generation leptons, was extended first to include two generations of quarks, and then a full third gen-

eration of fundamental fermions. The first generation consists of the electron (e) and its neutrino (ν_e) and the up (u) and down (d) quarks. The second generation includes the muon (μ), muon neutrino (ν_μ), charm (c) quark, and strange (s) quark and the third generation consists of the tau (τ), tau neutrino (ν_τ), top (t) quark, and bottom (b) quark. In each generation, the left-handed charged lepton and neutrino form a doublet under $SU(2)$ and so do the left-handed quarks. The quantum number associated with the $SU(2)$ symmetry is called weak isospin and the left-handed fermions have a third component of weak isospin, $t_{3L} = \pm\frac{1}{2}$. Right-handed fermions are isosinglets. The Higgs couples to these fundamental fermions f with Yukawa couplings, y_f. Each fermion propagates through the Higgs field and, by virtue of this coupling, acquires mass. The value of y_f is therefore related to the mass of the fermion, m_f, by $y_f = \sqrt{2}m_f/v$, where v is the vacuum expectation value of the Higgs field. The value of y_f is different for each fermion and is not predicted by the model. We can only ascertain its value by a measurement of each fermion's mass.

Strong interactions were given a coherent theoretical description by the non-abelian $SU(3)$ theory of quantum chromodynamics (QCD)[9] in conjunction with the quark model of hadrons[10]. Eight massless gauge bosons (gluons) propagate the interaction and carry a color charge. Quarks are the underlying constituents of hadrons. Their quantum numbers explain the isospin and baryon number properties of hadrons in nature. The strength of the strong interaction, governed by α_s, is large, making perturbative calculations difficult. The attraction between quarks exhibits asymptotic freedom, meaning that at large energies or very small distances, the interaction strength declines. The converse means that isolated quarks are prohibited from being extracted from hadrons. This 'confinement' means that bare colored particles are not observable in nature. Two colored partons receding from each other will produce a series of colorless hadrons in the final state. This process is called hadronization. These hadrons are collimated into jets moving roughly in the directions of the original partons. The process is understood phenomenologically by several models, eg. Ref. [11]. In the string fragmentation model, a narrow tube or 'string' connects two colored partons. As they recede, particles are created along the string which give rise to jets and energy flow along lines of color in an event. The physics of hadronization provides great challenges for precise measurements that involve jets, like those of the top quark.

1.2. *Top quark and the flavor spectrum*

The existence of the top quark is firmly placed in our picture of fundamental interactions. In our current understanding, all matter is made of fundamental fermion fields in two categories. Quarks are sensitive to the strong interaction; leptons are not. The electroweak eigenstates of quarks are a mix of the mass eigenstates, described by the CKM matrix[12]. As a result, generations that contain only a single quark lead to the expectation of flavor changing neutral current interactions. The absence of such interactions in experimental observations motivated the successful

prediction of the charm quark[13].

The discovery of the third generation tau lepton (τ)[14] and bottom quark (b)[15] led to the search for the top quark (t) as the $SU(2)$ partner of the bottom quark. Experimentally, several measurements showed that the bottom quark was a member of an $SU(2)$ doublet. Several early models[16–20] allowed for the absence of a sixth quark. If the bottom quark were an $SU(2)$ singlet, then flavor changing neutral current interactions would result in the B meson system. The limit on the branching fraction for $B \to \mu^+\mu^- < 10^{-3}$, however, put a stringent limit on these processes and ruled out the singlet hypothesis[21]. Measurements of B^0-$\bar{B}^0$ mixing[22] are sensitive to the magnitude of the CKM matrix elements V_{td} and V_{ts}. These were observed to be non-zero, indicating the existence of the top quark, although this could also be explained without the presence of a top quark[23]. Measurements of the third component of the weak isospin of the $b-$quark, t^b_{3L}, provided strong additional evidence. The $b-$quark coupling to the Z boson is dependent on $t^b_{3L} + \frac{1}{3}\sin^2\theta_w$, where θ_w is the weak mixing angle. Measurements of the $Z \to b\bar{b}$[24] rate, as well as the $b\bar{b}$ charge asymmetry in e^+e^- collisions[25,26] both probed this coupling. Both measurements indicated $t^b_{3L} = -\frac{1}{2}$[25], necessitating a $t_{3L} = +\frac{1}{2}$ partner to the b quark. A model was developed[23] to explain the Z width measurement without the top quark, but this could not account for the charge asymmetry measurement.

Theoretical arguments also favored the existence of a top quark once the τ lepton was identified. In the $SU(2) \times U(1)$ electroweak model, triangle diagrams with V and A couplings give rise to anomalies unless the total charge in a given generation sums to zero. With three color degrees of freedom per quark, anomalies are avoided in the first two generations. The existence of the τ (and its surmised neutrino) indicated the presence of a third generation quark doublet. Once the b quark was found, another quark of charge $= +\frac{2}{3}$ was required.

As a result, a search for the top quark was pursued from the late 1970's onward (e.g. Refs. 27–31). As accelerator energies continued to rise, the lower limits on the top quark mass increased. A fuller description of this period of research can be found in Ref. 3. By the mid-1990's, it was established that the top quark was very heavy[31]. This had the result of focusing the search strategies of the CDF and DØ collaborations and led to the discovery of top-antitop quark pair production in 1995 at the Tevatron[1,2].

1.3. *Top quark properties*

A massive top quark has several properties which make it quite interesting as a probe of known strong and electroweak physics, as well as a sensitive window to potential new physics. Perturbative QCD calculations of pair production can be carried out with significant precision. Electroweak production of single top quarks gives direct sensitivity to $|V_{tb}|$. The value of m_t places an important constraint on the mass of the Higgs boson. It has been speculated that the resulting top quark Yukawa coupling, $y_t \approx 1$, could point to new dynamics beyond the standard model[32]. The

exceedingly short predicted lifetime of the top quark of $O(10^{-25}s)$ is an order of magnitude smaller than hadronization timescales and this permits a glimpse of the properties of a bare quark. The decay modes of the top quark may harbor evidence of new physics if alternative models are correct. Measuring the charge of the top quark is important to establish that the top quark is as expected. A direct determination of the $|V_{tb}|$ matrix element probes for potential new physics.

2. Production and Decay of the Top Quark

For the next several years, the top quark will continue to be produced solely in hadron collisions, specifically involving protons. In such collisions, the top quark can be produced strongly in pairs or electroweakly alone. In general, the proton can be considered to harbor three 'valence' quarks (uud) which dictate its quantum numbers. These valence quarks typically carry much of the momentum of the proton. There are also virtual or 'sea' quarks and gluons in the proton which carry less momentum individually. When a proton and antiproton collide, a hard interaction occurs between one of the constituents ('partons') of the proton with a parton of the antiproton. Soft interactions involving the remainder of the hadron constituents produce many low energy particles which are largely uncorrelated with the hard collision. Because of the large mass of the top quark, production usually involves the higher momentum valence quarks at the Tevatron.

2.1. *Strong pair production*

Production of a top-antitop quark pair ($t\bar{t}$) occurs dominantly via strong processes. At leading order (LO), valence quarks supply the primary production probability at the Tevatron via quark-antiquark annihilation ($q\bar{q}$). Approximately 15% of the cross section comes from gluon (gg) fusion. Fig. 1 shows these diagrams.

In the center-of-mass frame in which the proton and antiproton are rapidly moving, the hard interactions between constituent partons are fast relative to the time for partons to interact. As a result, the hadronic collision can be factorized[33] into a parton collision weighted by 'parton distribution functions' (*pdf*'s), $F_i(x_i)$ which express the probability for parton i to carry momentum fraction, x_i, of its parent hadron. These *pdf*'s are properties of specific hadrons and are independent of the specific hard scatter interaction at parton level. They encompass non-perturbative soft processes. As a result, they are extracted from the examination of inelastic interactions involving hadrons. The pair production cross section is then calculated as

$$\sigma(p\bar{p} \to t\bar{t} + X) = \Sigma_{i,j} \int dx_i dx_j \times F_i^p(x_i, \mu_f) F_j^{\bar{p}}(x_j, \mu_f) \hat{\sigma}_{ij}(x_i, x_j, m_t^2, \mu_f^2) \quad (1)$$

where the sum runs over gluons and light quarks in the colliding proton and antiproton, and $\hat{\sigma}_{ij}$ is the perturbative cross section for collisions of partons i and j. The factorization scale, μ_F, defines the splitting of perturbative and non-perturbative

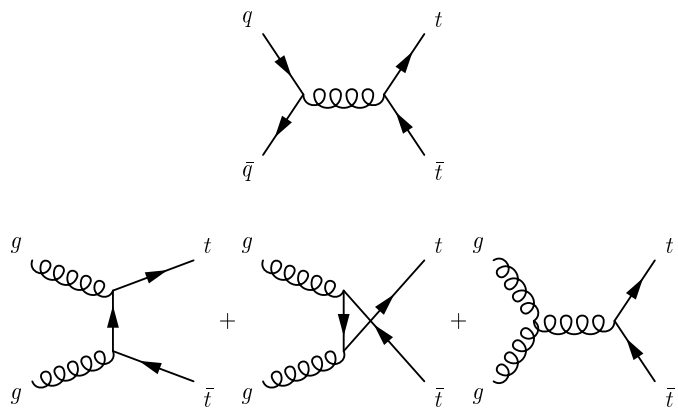

Fig. 1. LO Feynman diagrams for quark-antiquark annihilation ($q\bar{q}$) and gluon fusion (gg).

elements. It is common to treat this scale in common with the scale appropriate to the renormalization of the perturbative cross section, μ_R, since both parameters are arbitrary. This common scale, μ, is usually taken to be equal to the top quark mass (m_t). An exact calculation would not depend on these scales. Finite order calculations have a sensitivity that must be assessed as an uncertainty in the theoretical calculation, usually by bounding the predictions with $\mu = m_t/2$ and $\mu = 2m_t$ calculations.

Initial LO cross section calculations were performed in Ref. 34. Next-to-leading order (NLO) calculations[35,36] accounted for associated quark production and gluon bremstrahlung, and virtual contributions to the LO processes. Because top quark production at the Tevatron occurs near threshold, a large uncertainty in these calculations results from initial state soft gluon radiation. In order to fully account for this, several groups included resummation of dominant soft logarithms to all orders in perturbation theory for hadronic cross sections. Results from resummed Drell-Yan production[37,38] were generalized to handle the color elements in the initial heavy quark calculations[39–40]. While the corrections are small for $t\bar{t}$ production, the dependence of the cross section calculation on the choice of scale is reduced. This work has been improved with more recent *pdf's* and more accurate uncertainties in the determination of the pair production cross section[41]. The results of this calculation for Tevatron energies are given in Table 1. A total uncertainty of 10% to 15% is obtained for the NLO cross section[41]. Parton distribution functions, particularly for gluons at high x, provide the main source of theoretical uncertainty. The modest increase in collision energy from 1.8 TeV to 1.96 TeV causes a 30% increase in the production cross section. This is because of the substantial gain in valence quark phase space from the parton distribution functions.

Resummed calculations have also been performed including additional higher order terms[42,43]. Both Refs. 41 and 43 are based on 35, 36 with resummation at

Table 1. Calculated $t\bar{t}$ cross sections from Refs. 41, 43 assuming $m_t = 175\text{GeV/c}^2$. The former is a complete NLO calculation where the uncertainty is primarily from the choice in *pdf*. The latter provides an NLO calculation with additional higher order terms and an uncertainty taken from the choice in kinematic scheme. The rightmost column provides the change in calculated cross section ($\Delta\sigma$) appropriate to a change in m_t [41].

$\sqrt{s}$ (TeV)	Kidonakis, et al.[43]	Cacciari, et al.[41]	$\Delta\sigma$ (pb) ($m_t = 170, 180$ GeV)[41]
1.8	5.24 ± 0.31 pb	$5.19^{+0.52}_{-0.68}$ pb	+0.91, -0.76
1.96	6.77 ± 0.42 pb	$6.70^{+0.71}_{-0.88}$ pb	+1.13, -0.95

least to next-to-leading logarithms. A difference between them is that the former resums soft gluons to all orders, while the latter ignores small terms beyond next-to-next-to leading order. Because top quark production is at threshold and both calculations are not complete beyond NLO, there is an ambiguity in the soft-gluon resummation calculation. We do not attempt a detailed review of this topic here, but in short the situation is the following. These calculations are performed in terms of a choice of kinematic parameters, and different choices will give slightly different parton level calculations[42]. To address this, Ref. 43 has expanded the ersummed cross section to next-to-next-to leading order. The resulting corrections are small for choices of scale $= m_t$, but the observed dependence of the cross section on scale and kinematics is further reduced. The results of this calculation for $\sqrt{s} = 1.8$ and 1.96 TeV are given in Table 1. The remaining difference from choice of kinematics provides the uncertainty estimate [43].

Because of its short lifetime, the $t\bar{t}$ pair is not expected to form a bound meson. However, non-standard production mechanisms have been proposed which do form a $t\bar{t}$ resonance, eg. Ref. 44. Testing such production mechanisms will help determine if the top quark fills a special role among fundamental fermions. Such analyses will be discussed in Section 8.1.

2.2. *Electroweak production of single top quarks*

In addition to the pair production of top quarks via the strong interaction at the Tevatron, they can also be produced singly in electroweak interactions. There are three modes of single top quark production, which differ in the virtuality, Q^2, of the participating W boson, where Q^2 is the negative square of the W boson four momentum q. Two of the three modes are labeled by the corresponding $Mandelstam$ variables t and s involved in the transition matrix elements. The three dominant modes of single top quark production are listed below in descending order of their expected production cross section:

- t-channel: In the process $p\overline{p} \to tq\overline{b} + X$, the W boson is spacelike ($-Q^2 = q^2 = t < 0$). The predicted cross section for this channel, for the Tevatron center of mass energy $\sqrt{s} = 1.96$ TeV, computed at NLO is $1.98^{+0.23}_{-0.18}$ pb[45].

Inclusion of NNLO and NNNLO threshold soft-gluon corrections leads to a cross section of 2.30±0.14 pb[46]. Two Feynman diagrams, as shown in Fig. 2, contribute to this channel. In the leading order diagram, the b quark is from the sea of quarks in the proton or anti-proton which couples with the virtual W to produce a top quark. In the next-to-leading-order diagram, the anti-bottom ($\bar{b}$) quark comes from the splitting of the gluon into a $b\overline{b}$ pair. The b quark couples to the virtual W boson and produces the top quark. Thus this channel is also known as W-gluon fusion. The $\overline{b}$ quark in the final state has low transverse momentum (p_T) and is at high η. The t-channel denotes the processes with the following quarks in the final state: $tq\overline{b}, \overline{t}\overline{q}, t\overline{q}\overline{t}q$. We denote this channel as tqb.

- s-channel: In the process $p\overline{p} \to t\overline{b}+X$, the W boson is timelike ($-Q^2 = q^2 = s \geq (m_t + m_b)^2 > 0$). For this channel the predicted cross section at NLO for $\sqrt{s} = 1.96$ TeV is $0.88^{+0.08}_{-0.07}$ pb[45]. Corrections at NNLO and NNNLO leads to a predicted cross section of 1.08±0.08 pb[46]. The two initial-state quarks annihilate into a virtual W boson which decays into a top quark and a bottom quark, see Fig. 2. The s-channel includes both $t\overline{b}$ and $\overline{t}b$ and is also referred to as W^* production. We will refer to this channel as tb.
- associated single top quark production: In the process $p\overline{p} \to tW$, $Q^2 = m_W^2$, an on-shell W boson is produced together with a top quark. The production cross section for this channel is predicted to be very small, about 0.28±0.06 pb at NLO plus NNLO and NNNLO threshold soft-gluon corrections[46].

There are also other diagrams for single top quark production which involve $Wt\overline{s}$ or $Wt\overline{d}$ vertices, but they are highly suppressed due to the small CKM matrix elements. Their contribution to the cross section is expected to be less than a percent.

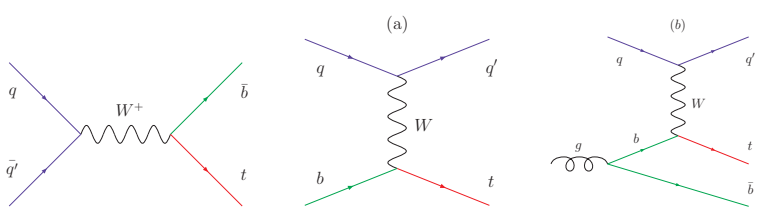

Fig. 2. Feynman diagram for leading order s-channel single top quark production (left) and t-channel single top quark production (middle and right). The middle diagram is the leading order and right one is the $O(\alpha_s)$ W-gluon fusion diagram .

One of the primary interests in establishing the cross section for single top quark production is that its production cross section is directly sensitive to the transition width of $t \to Wb$, and consequently to $|V_{tb}|$. The partial decay width of the top quark, $\Gamma(t \to Wb)$, can be measured, and hence it will be possible to measure the top quark lifetime. At the Tevatron, single top quark events have the

same final state signature as the production of a Higgs boson in association with the W boson, thus understanding single top quark productions is an important prerequisite for Higgs searches at the Tevatron. Single top quarks are also one of the irreducible backgrounds to associated Higgs production. Studies of single top quark events could lead to insights into the existence of non standard couplings (e.g. right-handed couplings and polarization) in the top quark decays to W boson and b-quark. Single top quark production is very sensitive to new physics. The s and t-channels are sensitive to different new physics and hence can be used to distinguish between various exotic models (Top Flavor, 4th generation or those which produce flavor changing neutral currents etc).

2.3. *Top quark decays and final states*

With three generations of quarks, the unitarity of the CKM matrix[48] in conjunction with the measured values of V_{ub} and V_{cb} means the decay probability of $t \to Wb$ is virtually 100%. The W decay is divided approximately equally between each of the three lepton-neutrino ($l\nu$) pairs and each of the three colored doublets of up-down quarks and of charm-strange quarks. The quarks will hadronize to produce jets and heavy flavor mesons from b quarks will decay. Typically, the $b-$jet and W decay products will have large momenta in the plane transverse to the beam ('transverse momentum', or 'p_T') because of the high value of m_t.

Events from top quark pair production consist of two W bosons, and two b-quarks: $t\overline{t} \to W^+bW^-\overline{b}$. Both W's may decay leptonically, one may decay leptonically and the other hadronically, or both may decay to hadrons. The first case, termed 'dilepton', gives a final state of $\ell^+\nu\ell^-\overline{\nu}b\overline{b}$ and manifests itself in the detector as two high p_T leptons, significant unobserved p_T from the νs ('$\not\!\!E_T$'), plus two b-quark jets. The second 'ℓ+jets' scenario provides $\ell^\pm\nu q\overline{q}'b\overline{b}$ and is observed as one high p_T lepton, large $\not\!\!E_T$, and four jets including two b-jets. The last decay chain is the 'all-jets' channel and it results in a $q_1q_2\overline{q}_3\overline{q}_4b\overline{b}$ final state appearing as six jets including two from b-quarks. If the leptons are restricted to e and μ, the usual case, then the total branching fractions are approximately 5%, 30% and 45% for dilepton, ℓ+jets and all-jets channels, respectively. Quark color degrees of freedom are primarily responsible for the substantially larger branching fraction of $t\overline{t}$ to the ℓ+jets and all-jets final states.

Final states arising from single top quark production consist of a top quark, a bottom quark and a light quark (t-channel or tqb), or a top quark and a b quark (s-channel or tb). To successfully identify single top quark production in the presence of backgrounds, the $W \to e\nu(\mu\nu)$ decays are required. Thus single top quark events contain an isolated hight p_T lepton, significant $\not\!\!E_T$ due to the neutrino, two b-jets (and a light quark jet in the t-channel production).

In addition, for both the $t\overline{t}$ and single top quark production events, the heavy flavor hadrons from b quark fragmentation will have a long lifetime. This means that final state particles will originate from a location which is some distance away from

the event primary vertex. Sometimes these b-jets will exhibit a soft, non-isolated e or μ from semileptonic b decay.

2.4. *Modeling top quark signal and background*

Measurements of the top quark require a firmly understood simulation of signal and background processes. This understanding includes a need for reliable estimates of event selection efficiency and the kinematic and angular distributions in the final state. Event generators are used to simulate the physics of production, decay and hadronization. Two kinds are employed. Exact leading-order calculations such as in ALPGEN 1.2[49] result in the partonic final states at the origin of observed events. ALPGEN in particular also includes the spins of the particles. Showering Monte Carlos such as PYTHIA 6.2[50] or HERWIG 6.4[51] simulate the hard scatter with leading order elements and employ a phenomenological showering mechanism to account for hadronization. An approximate perturbative QCD description of gluon radiation is implemented in these simulations. PYTHIA also adds the underlying event from the proton antiproton interaction. The two types of generator are often used sequentially so that the hard and soft physics are dealt with as completely as possible. In more recent experimental analyses, a significant effort is being made to correctly account for potential double-counting of soft QCD processes when this is done. A proposed mechanism to match observed jets with partons is now employed in these cases[52,53]. An alternative approach is also available[54]. Specialized simulators are also employed to perform important calculations for τ decays (TAUOLA[55]) or b and c quark decays (QQ 9.1[56], EVTGEN[65]). These generators are reviewed in detail in Ref. 66. The specifics of their use are documented in some of the papers reviewed below (e.g. Ref. 67).

Various Monte Carlo generators were used to model single top quark events. DØ uses the SINGLETOP package[68], based on the COMPHEP Monte Carlo generator[69] to produce the parton four-vectors of the single top quark signal events. This package uses a leading order simulation for the s-channel and a next-to-leading-order simulation for the t-channel processes. Spin information in both the production and decay is included. The matrix element event generator MADGRAPH/MADEVENT[70] is used by the CDF experiment to simulate the signal processes.

Most of the Run II CDF analyses described in this paper use these generators in the following way. In general, the CTEQ5L structure functions are used. Monte Carlo samples for $t\bar{t}$ to calculate acceptances and efficiencies, and to understand kinematic shapes, are generated with both PYTHIA and HERWIG. ALPGEN plus HERWIG is used with the parton matching algorithm to model the $W+$ heavy flavor backgrounds. Diboson backgrounds are also generally modeled with ALPGEN+HERWIG. Single top quark backgrounds for ℓ+jets channels, and $Z/\gamma*$ backgrounds for dilepton channels are studied using PYTHIA. In general, b and c quark decays are handled by the QQ generator[56].

The DØ Run II simulation generally uses ALPGEN fed into PYTHIA for signal

estimation. W+jets and diboson production are also simulated with ALPGEN and PYTHIA. $Z \to \tau\tau$ backgrounds are studied using PYTHIA. In general, TAUOLA and EVTGEN are used for τ and b/c hadron decays, respectively. The Q^2 scale used by DØ single top quark s-channel and $t\bar{t}$ samples is m_t^2, while the t-channel is generated at $(m_t/2)^2$. CTEQ6M (CTEQ6.1M) parton distribution functions are used for single top quark ($t\bar{t}$) events. The components of the W+jets process: heavy flavor process $\bar{q}q' \to Wg$ with $g \to b\bar{b}$ or $g \to c\bar{c}$, and $gq \to Wc$) are included in their relative proportions estimated using ALPGEN and normalized to the data.

3. Experimental Facilities and Reconstruction

3.1. *Experiments*

The Tevatron provides sufficient energy to create the extremely massive top quark. The two experiments at the Tevatron, DØ and CDF, are therefore unique in their ability to study the top quark directly. The accelerator complex at Fermilab accelerates protons through a linear accelerator and three synchrotrons, the Booster, the Main Injector, and the superconducting Tevatron ring[57]. The Main Injector was built for Run II to increase the number of antiprotons that can be injected into the Tevatron. Antiprotons are produced by extracting protons at intermediate energy onto a nickel target. They are selected from the secondaries that are produced and then cooled and accelerated before they are injected into the proton acceleration chain. Proton and antiproton beams are accelerated to a final energy of 980 GeV in the Tevatron to provide proton antiproton collisions at 1.96 TeV, up from 1.8 TeV in Run I. The use of antiprotons is important because it provides the ability to use valence quark annihilation, with available higher parton center of mass energies, for top quark production. Instantaneous luminosities are high, so far reaching $2.6 \times 10^{32}/cm^2/s$. Typically around three proton-antiproton interactions occur with each beam crossing.

Collisions occur in the two locations on the Tevatron Ring where the DØ and CDF experiments are located. Both detectors (see Fig. 3) have magnetic central tracking regions which include silicon microstrip trackers for precise vertex measurements. Field strengths of 1.4 T and 2.0 T are achieved via superconducting solenoids for CDF and DØ, respectively. The higher value for DØ partially compensates for a smaller tracking volume. Primary charged particle tracking is performed for CDF by a drift chamber which obtains 96 position measurements for each particle. Acceptance ranges to $|\eta| < 2.0$ for silicon and $|\eta| < 1.0$ for the drift chamber. DØ utilizes a scintillating fiber tracker composed of sixteen doublet fiber layers. In tandem with the silicon microstrip detector an acceptance of $|\eta| < 3.0$ is achieved. All trackers replace Run I equivalents[58,59], resulting in better b-tagging efficiency for CDF[60], and a new b-tagging and track momentum measurement capability for DØ[61].

Sampling calorimeters with large acceptance provide energy measurements for electrons, photons, and hadrons. DØ utilizes uranium absorber bathed in a liquid

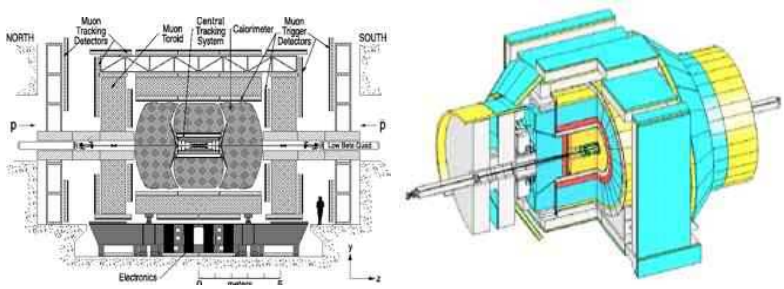

Fig. 3. The Run II DØ detector (left) and CDF detector(right). Each detector has an inner tracking region surrounded by calorimeters and outer muon spectrometers.

argon sampling medium to achieve near-compensating performance, good energy resolution and low backgrounds for the surrounding muon spectrometer[58]. Coverage extends to $|\eta| < 4.2$. Scintillator-absorber layers provide these measurements for CDF in the region $|\eta| < 3.6$[59]. New endplugs for CDF[60], and electronics and hardware trigger upgrades for DØ[61] deliver improved performance for the high instantaneous luminosities achieved in Run II.

Drift tubes and scintillator arranged in layers outside of the calorimeter are used for muon identification for both experiments[58,59]. In the DØ case, these layers are distributed in front of and behind thick background-suppressing magnetized iron toroids which provide a 1.8 T field for the full coverage to $|\eta| < 2$. The CDF detector has coverage to $|\eta| < 1.0$. The primary enhancements from Run I are improved forward coverage for both experiments[60,62].

Data are taken using a three-tiered trigger system composed of one hardware and two software levels. Luminosity is measured via gas Cerenkov or plastic scintillation counters mounted in the forward regions of CDF and DØ, respectively. Analyses utilize data taken from 2002 until Spring 2006. By Spring of 2007, each experiment had accumulated about 2.5 fb^{-1} of collision data.

3.2. *Reconstruction*

The effective identification of e, μ, ν, light quark jets, b jets and τs is crucial to the analyses reviewed in this paper. One cannot properly demonstrate the requisite understanding of signal and background efficiency without a thorough understanding of the performance of the detector to measure their energies or momenta, their efficiencies, and their rates to be incorrectly reconstructed. This subsection describes the methods of identification for these primary objects as well as the ways in which their performance is determined and propagated into experimental models of the processes being considered.

Electrons and Muons: Electrons are reconstructed as grouped or 'clustered' electromagnetic calorimeter (EM) elements which exhibit significant energy. Cells are the fundamental elements used by DØ. Three adjacent towers are used by CDF. These clusters are associated with a well-reconstructed charged particle track. A range of parameters are used to identify good electrons, including the ratio of EM to hadronic energy, isolation from more energy in a wider cone around the centroid, cluster energy divided by track momentum (E/p), and shower shape. CDF applies these cuts for 'tight' electrons, and omits the isolation requirement for 'loose' electrons. DØ applies basic cuts on electron candidates and then assembles a likelihood discriminant which combines these and other calorimeter and tracking parameters. For DØ, only isolation and EM-fraction cuts are applied for loose electrons. Muons are identified from track signatures in the outer muon spectrometers of each experiment, which are then matched to charged particle tracks. In the case of DØ, isolation cuts are applied based on tracks and calorimeter energy. Loose muons may pass a looser isolation selection.

The efficiency, momentum resolution and energy scale performance of e and μ in the detector are typically measured by examination of $Z \to ee, \mu\mu$ events. By requiring one 'tag' lepton to be well-identified, and employing other cuts to suppress non-Z backgrounds, the other 'probe' lepton can be measured in an unbiased way. The reconstructed mass of the Z boson is a direct reflection of the electron energy scale. Isolated leptons can be misidentified typically from jet activity. This can occur through fragmentation to $\pi^0 \to \gamma\gamma+$ track where the track is from a conversion or charged hadron overlap. Semileptonic decay of hadrons in the jet can also rarely provide isolated leptons with significant p_T. The probability at which jets mimic leptons is termed the 'fake rate'. It is often extracted from multijet samples where W and Z/γ^* contributions are suppressed. For instance, DØ uses such samples with leptons passing very loose requirements. It is important that signal trigger conditions on the faking lepton be reproduced.

These selections are applied to find leptons from the W bosons in top quark decay. It is also important to be able to identify leptons from semileptonic heavy flavor meson decay. Such leptons can be used to flag a reconstructed jet as having come from the fragmentation of a $b-$quark. These 'soft leptons' do not have to satisfy the isolation requirements. Estimation of the rate in data to tag $b-$jets with a soft lepton is usually ascertained from a dijet sample where one jet is tagged and a non-isolated lepton is sought in the other. The rate for typical jets, primarily light flavor jets, to produce a 'mistag' is measured from a multijet sample, such as $\gamma + jet$ events.

Jets, τs and $\not\!\!E_T$: An iterative, fixed-cone algorithm[63] is applied to electromagnetic and hadronic calorimeter elements to reconstruct jets. Because of the high jet multiplicity in top quark events, cone sizes used are generally small: for DØ (CDF) most analyses use $\Delta R = \sqrt{\Delta\phi^2 + \Delta\eta^2} = 0.5(0.4)$. Jet energies are corrected for various effects such as non-linearities in single particle response, unregistered energy

at detector element boundaries and cracks, particle showers, and underlying event and multiple interactions. The jet energy scale is ultimately measured using $\gamma+$ jets events where the photon in the electromagnetic calorimeter section is calibrated via the $Z \to ee$ resonance. The general approach compares the momentum of the jet in the transverse plane ('transverse momentum', or 'p_T') to the reference provided by the photon p_T, although in practice several effects mean that a direct p_T comparison is not optimal[64]. A subset of jets can be further identified as originating from the fragmentation of heavy quarks, particularly $b-$quarks, if they encompass an associated, non-isolated low p_T electron or muon from semileptonic decay or if they match a secondary vertex. Hadronic τ lepton decays are also identified as jets. In this case selections are applied based on shower profile in the calorimeter, as well as requirements of one or three tracks in the jet cone.

Neutrinos escape the detectors undetected. Their presence can be inferred from a significant imbalance in the p_T of all observed particles in an event. Recall that, since most final state particles are essentially massless compared to the magnitudes of their momenta, $p \sim E$. So the event-wide p_T imbalance is generally termed missing E_T, or $\not{E}_T$. The $\not{E}_T$ is calculated as the negative of the vector sum of the E_T's of individual calorimeter elements. This quantity is then corrected for the p_T's of any reconstructed μ's in the event, as well as the energy scale corrections for jets and electrons.

Vertices: The $p\bar{p}$ collision point is called the event primary vertex. It is reconstructed with well-measured tracks that are consistent with origination from the same point. In many cases, more than one primary vertex are reconstructed. These may be due to extra $p\bar{p}$ interactions resulting from the high operating instantaneous luminosity. There will generally be only one vertex corresponding to the hard scatter giving rise to a top quark.

The secondaries from the decay of long-lived B hadrons produce charged particle tracks that originate from a vertex that is displaced from the primary vertex. Both CDF and DØ employ algorithms that identify ("tag") jets as originating from $b-$quarks by reconstructing such secondary vertices within a particular jet ('secondary vertex tag'). Such secondary vertices are reconstructed from at least two well-reconstructed tracks with $p_T > 1.0$ GeV that match a jet. These tracks must have an impact parameter in the transverse (x, y) plane with a significance of $> 3\sigma$ with respect to the primary vertex for CDF. DØ applies a 3.5σ cut. CDF adds a second, three-track vertex with relaxed track p_T and impact parameter cuts. The vertex reconstructed from these tracks must be significantly displaced from the primary vertex in the transverse plane, given the known tracking resolutions and it must be on the same side of the primary vertex as the jet, to tag a jet as a b-jet.

Other tagging algorithms exist. For instance, an 'impact parameter tag' algorithm has been used by DØ which is based on counting the number of tracks with impact parameter significance above a certain value. Both experiments have also implemented 'jet probability taggers'. These use the knowledge of track resolutions

to calculate a probability that tracks in jets originate from an event primary vertex and compute a jet probability based on the combined track probabilities. The jets are tagged if the jet probability has a low value, indicating an inconsistency with the hypothesis for that jet to originate from the primary vertex. DØ and CDF also use neural networks to combine the various parameters associated with a b-tag such as impact parameter, momentum and invariant mass of all tracks associated with the vertex, vertex displacement, etc. into a more powerful discriminant.

It is important to understand the efficiency for $b-$jets to be tagged, and light quark and gluon jets to be mistagged. Jets from $c-$quarks and their relevant tagging rates must also be accounted for. The efficiency for a particular $b-$tagging algorithm is generally measured in heavy-flavor enriched inclusive jet samples in data. Such an enrichment can be achieved by lepton-tagging a jet for which the $b-$tag efficiency is to be measured. Monte Carlos are used to obtain an estimate of the residual $c-$quark content and other selection biases. The mistag rate to falsely identify light quark or gluon jets as $b-$jets is estimated from samples of inclusive jet events. The primary backgrounds produce displaced vertices that are equally probable to be 'behind' the primary vertex (negative tags) from the point of view of the jet they correspond to, and 'in front of' the primary vertex (positive tags). However, heavy flavor will produce an asymmetric distribution with more positive vertex displacements. The negative tag rate is a useful first approximation to the mistag rate. It must be corrected for heavy flavor in the jet samples, as well as for long-lived particles in actual light flavor jets that are not reflected in the negative tag rate. Final tag and mistag rates are parametrized as functions of p_T and η.

Performance and parametrization of simulation: The final element tying the simulation of signal and background samples to the data involves the simulation of the detector. For CDF and DØ , GEANT3[71] is used with a full detector simulation. At this stage minimum bias Monte Carlo events were added to the hard scatter such that the Poisson distribution mean matches the average instantaneous luminosity of the data sample.

In general, the simulation does not replicate exactly the detailed performance parameters of the detector. The parameters of interest are: e and μ identification efficiency, momentum resolution and energy/momentum scale; jet efficiency, energy resolution and energy scale; $\not\!\!E_T$ resolution; and $b-$tag algorithm efficiency. As a result, it is necessary to quantify each element of performance in the simulation and in the actual detector using isolatable control samples. For leptons, these are generally the $Z \rightarrow ee, \mu\mu$ samples. For jets, an important sample is the γ+jet sample. $b-$tagging requires simulated inclusive jet samples. The simulation is then corrected so that the performance for real data is replicated. A few performance measures must be measured only for use in data. These are generally the lepton fake rates and the $b-$tagging mistag rates.

4. Top Quark Pair Production Cross Section Measurements

Measurement of the top quark pair ($t\bar{t}$) production cross section permits a unique test of perturbative QCD predictions. Unveiling discrepancies between measured rates and expectations for various final state channels provides a potential indication of new physics. The selection of clean, well-understood analysis channels facilitates the measurement of the top quark mass and other properties. In this section, we discuss the primary channels that have been employed for the cross section measurement. These consider variants of the dilepton, ℓ+jets and all-jets channels. Analyses of τ channels, while they have been pursued, have not yet provided significant constraints on $\sigma_{t\bar{t}}$ and are omitted from this section.

Two primary aspects of these analyses are general in their impact. The event selection that is used for all top quark measurements has been developed based on extensive studies of the expected properties of $t\bar{t}$ events as well as those from known backgrounds. The lepton, jet and $\not\!\!E_T$ cuts are derived from these studies, as are more sophisticated parameters which consider angular correlations, scalar E_T sums, or event topology. Given a particular event selection, the behavior of signal and background events in terms of these variables must be understood well enough to keep uncertainties in the measurements under control. It is particularly important that the background models be validated wherever possible to optimize the analysis sensitivity. Achievement of an effective selection whose performance can be confirmed not only ensures an optimal cross section measurement, but it also serves as the foundation for measurements of the properties of the top quark. We discuss these two issues in this section and then review the individual measurements from DØ and CDF.

4.1. *Selection variables*

Events containing a $t\bar{t}$ pair have several distinctive characteristics that are not reflected by the anticipated backgrounds. In general, the total scale of energy in the event, particular in jets, is quite large. Decay products are roughly isotropically distributed in top quark events. These two qualities follow largely from the high mass of the $t\bar{t}$ pair. A third category comes from the observation that some backgrounds come from mismeasurement and this reflects itself in angular correlation between objects. The discriminating variables used fall into the following categories:

Energy scale: Due to the large mass of the top quark, the characteristic energy scale of the $t\bar{t}$ event is significantly larger than that of the average QCD background event. This means that $t\bar{t}$ events generally have more energetic jets and larger multi-jet invariant masses. This is especially true of the leading two jets from the b quarks which come directly from top quark decay. This total energy scale is most often expressed as a scalar sum of object $E_T(p_T)$s, termed H_T. Sometimes the discriminating power can be increased by also adding observed lepton p_Ts and perhaps also the $\not\!\!E_T$. Invariant mass parameters, such as for the leading two jets ($M_{min}^{1,2}$), the second leading two jets ($M_{min}^{3,4}$) or all of the objects (ℓ, jets, $\not\!\!E_T$), also indicate the production of a high mass state.

Event topology: In general, backgrounds with jets originating from gluon radiation provide steeply falling p_T spectra for jets. The manner in which color flows in such events tends to produce particles that congregate in a planar geometry. Additionally, QCD events usually have a more back-to-back spectrum because of their hard scatter origin. The jets from $t\bar{t}$ decay, on the other hand, are almost isotropically distributed. These differences can be quantified using event-shape parameters, such as sphericity, $\mathcal{S}$, and aplanarity, $\mathcal{A}$, calculated from the normalized momentum tensor[72]. Top quark events tend to have higher $\mathcal{A}$ and $\mathcal{S}$ than the background events.

Rapidity spectrum: $t\bar{t}$ events on average are expected to have more jets of higher energy and with less boost in the beam direction, resulting in events with many central jets. The QCD background tends to have jets that are more forward-backward in rapidity. One variable considered is the centrality ($\mathcal{C}$), defined as $\mathcal{C} = \frac{\sum E_T}{\sqrt{\hat{s}}}$, where $\sqrt{\hat{s}}$ is the total energy in the event (or it may represent the scalar sum of the momenta (energies) of jets ΣE^{jets}). Another variable is $< \eta^2 >$, the p_T-weighted mean square of the η of the jets. The QCD multijet background is expected to have a broader distribution in $< \eta^2 >$ than the $t\bar{t}$ signal.

Angular Correlations: Several of the backgrounds arise because the $E_T(p_T)$ of one or more objects in candidate events have been significantly mismeasured. Often, this mismeasurement will create the appearence of $\not{E}_T$ either in the azimuthal direction of the offending object, or opposite it. Jet energy and μ momentum resolutions are most often the cause. As a result, cuts are placed on the angular correlation of objects: $\Delta\phi(x, y_i)$ is the azimuthal angle between the transverse momentum vector of objects x and y_i. Here, the subscript i denotes leading, second leading, etc. of object y. Common uses are $\Delta\phi(\not{E}_T, \mu_1)$ or $\Delta\phi(\not{E}_T, j)$ where μ_1 is the leading muon or j is a jet.

4.2. *Background extraction from data*

Production of top quark pairs presents a unique set of final states. However, the high mass of the top quark also means that the production cross section is quite small. Use of the variables discussed in Section 4.1 entail a heavy reliance on measurements of jets and $\not{E}_T$. These are complex observables defined by sophisticated algorithms and subtle physics at a hadron collider. Simulation of background processes must be complemented by study of those processes in the data. Often, the attempt to validate the background model will result in corrections to the simulation that will improve agreement. In other cases, the background will be taken from the data alone or in combination with the simulation. The simulation can still provide a valuable cross-check of the model, since it represents the best attempt to estimate the background from first principles. This in turn gives confidence in the signal model which can only be obtained from Monte Carlo. Common schemes to be elaborated in the following

sections are:

Modeling Jet Production: The physics behind jets involves soft processes and the algorithms used to reconstruct jets have complex behavior. For all analyses, it is therefore important to demonstrate an understanding of the background (and signal) at all jet multiplicities. In low jet multiplicities, background will dominate. Agreement between models and data provides a confirmation of the background model in the signal rich bins. Typically this will be reflected as an estimate of the sum of signal and background ('$S + B$') vs. jet multiplicity, with the observed data in comparison. Another approach is to consider the agreement of the modeled and observed jet p_Ts. This has occasionally been used, for instance, to determine the background level from a fit to the leading jet p_T.

Lepton Backgrounds: Jets also impact analyses because they can mimic charged leptons or evidence of νs. In the former case, it is difficult to precisely model those jets that shower in the detector to look like electrons, or that produce a lepton from semileptonic decay which can pass lepton isolation and p_T cuts. The rate for jets to fake leptons is obtained in data as mentioned in Section 3.2. Two things are crucial in the use of these rates. First, samples must be identified in data which have negligible signal contribution. Second, it is important that the faking, which is a result of hadronization or decay, be uncorrelated with the kinematics of the event. Typically, samples are selected with all kinematic selections and one lepton identification relaxed. In the case of $\not\!\!E_T$, the rate to satisfy certain $\not\!\!E_T$ cuts in a ν-less process (termed the '$\not\!\!E_T$ fake rate') is studied in $Z \to \ell\ell(\ell = e, \mu)$.

Jet Flavor Modeling: Identification of $b-$jets from evidence of displaced secondary vertices or non-isolated soft leptons plays an important role in selecting a sample enriched with top quark events. In all $b-$tag analyses, the rate for light quark or gluon jets to accidentally satisfy the soft lepton or displaced vertex criteria is called the 'mistag rate' as described in Section 3.2. The application of these mistag rates to an untagged background sample can be somewhat more complicated than for the leptons. The reason is that jets arising from the hadronization of $c-$quarks can also harbor high impact parameter tracks. Also, all backgrounds contain some relative fraction of light quark, c and b jets. In $W+$jets production, most of the associated jets arise from light quarks or gluons. Occasionally, gluon splitting will generate a $b\bar{b}$ or $c\bar{c}$ pair which give rise to heavy flavor jets. More rarely, sea $s-$quarks radiate a W boson giving a single $c-$quark and subsequent jet. It is common in this instance to use Monte Carlo to provide some estimate of the relative flavor content, and then to apply the mistag rates or tagging efficiencies to the relevant background fractions.

4.3. *Dilepton final states*

The signature of two isolated, high p_T leptons and $\not\!\!E_T$ in association with two high E_T jets is a striking consequence of the $t\bar{t}$ quark decay chain where both W bosons decay leptonically. The only processes exhibiting the leptonic signature are diboson production, particularly WW where both W's decay leptonically as in the $t\bar{t}$ case, or $Z \to \tau\tau$ production where both τ's decay leptonically. Diboson cross sections are of the same order as that expected for $t\bar{t}$ production. $Z \to \tau\tau$ production is much greater but the dilepton branching fraction is small and the charged lepton and ν p_T's are soft. In both cases, additional jets are only produced at a rate of approximately α_s each and so jets become a primary discriminator of these backgrounds.

Beyond these processes, it is possible to mimic the top quark signature through instrumental mismeasurement. The chief background arising this way comes from $Z/\gamma^* \to ee, \mu\mu+$ jets production. Here the reconstructed $\not\!\!E_T$ is the result of tails in the jet or lepton energy or momentum resolutions. An important background also comes from $W \to e, \mu+$ jets production where one of the jets fakes an isolated lepton. QCD multijet production is a background when both leptonic and $\not\!\!E_T$ mismeasurement occur.

In order to extract a measurement of the top quark production cross section in the dilepton channels, different techniques have been developed. One of the most widely used has been a selection where loose and tight versions of the lepton identification are employed. For 'explicit' dileptons, these distinctions still refer to selections requiring convincing signals in the subdetectors responsible for lepton identification, particularly the electromagnetic layers of the calorimeter and the outer muon spectrometers. However, these detectors have significant gaps and holes in their coverage, and lepton identification and isolation requirements are inefficient. The resulting loss in acceptance seriously reduces the signal event yield in the dilepton channel. In the most extreme 'implicit' dilepton strategies, identification requirements are relaxed to mere requirements of an isolated, high p_T track or even to no evidence of a second lepton at all. Such an approach can accept dilepton events where one of the leptons is a τ which decays hadronically. Event-wide kinematic variables and tagging of jets from $b-$quarks are valuable ways to isolate the dilepton final state, particularly when the lepton requirements are relaxed and backgrounds are higher.

4.3.1. *Explicit channels*

Explicit dilepton analyses are defined as those in which both leptons are fully reconstructed as either e or μ. $W \to \tau \to e, \mu$ decay modes cannot be distinguished from, and so are grouped with, the direct $W \to e$ or $W \to \mu$ channels. Three channels have been examined by both Tevatron experiments: $ee, e\mu$ and $\mu\mu$.

The DØ experiment has used explicit channels to produce a cross section measurement at $\sqrt{s} = 1.96$ TeV with 243 pb^{-1} of data [73]. Events were triggered with

two leptons in the first level hardware trigger and one or two leptons in the higher level software triggers. In general, the Run II measurements derive many techniques from the Run I analyses[74] (see final combined Run I cross section in Table 5). Although the differences are less than in Run I, momentum resolutions are significantly different for e's and μ's. This means event selections across the three channels are somewhat varied. Also, because b-jets carry away a large momentum directly from top quark decay, DØ uses relatively soft lepton p_T cuts and stiff jet E_T cuts. The primary background which arises after these cuts is mainly $Z/\gamma*$+jets production. A substantial cut on $\not\!\!E_T$ reduces this background considerably, but it is still the primary background in the like-flavored channels. Suppression of this background involves rejecting events with dielectron or dimuon invariant mass (M_{ee} or $M_{\mu\mu}$) consistent with that measured for the Z boson M_Z[75]. In the ee channel, the excellent electron energy resolution allows a narrow window to be drawn around the reconstructed M_{ee}. The cut on $\not\!\!E_T$ is elevated for events within this window. For the $\mu\mu$ channel, the muon momentum resolution from the tracker degrades at higher p_T and has significant non-gaussian tails. Instead of a window cut, a kinematic fit is employed which quantifies a χ^2 test with respect to M_Z, $\chi^2_{M_Z}$. In Run I, this test used the muon and calorimeter measurements and knowledge of their resolutions. The improved Run II detector has permitted a simpler test based on the muon momentum measurements alone.

The selections were optimized to produce the smallest fractional statistical uncertainty on the cross section, taken to be proportional to $S/\sqrt{S+B}$. These optimizations used several variables, including event shape variables, dilepton mass and $\not\!\!E_T$ cuts. The most important of these variables have been the jet E_T and H_T. The final selection criteria are given in Table 2.

Instrumental backgrounds consist of $Z \to ee, \mu\mu$ background events where the $\not\!\!E_T$ may be mismeasured, and W+jets and multijet events where the jets fake leptons. These are generally determined from data. Lepton backgrounds are estimated by folding fake rates into a signal-like sample with one tight lepton. For the $Z \to ee$ background, the rate for $\not\!\!E_T$ to pass the DØ cuts is assessed in a sample of $\gamma + 2$ jets events that are kinematically similar to the $Z + 2$ jets sample. Agreement in the $\not\!\!E_T$ spectrum is observed for the Z+jets data sample confined to the region 80 GeV$< M_{ee} <$ 100 GeV and a high statistics γ+jets sample. The $\gamma + 2$ jets behavior also agrees well with a high statistics $Z(\to ee) + 2$ jets Monte Carlo sample where all known effects on the $\not\!\!E_T$ resolution in data have been accounted for. The ratio of events to pass divided by those that fail the $\not\!\!E_T$ cut is extracted from the data and multiplied by the number of ee events failing the $\not\!\!E_T$ cut in data. The $Z \to \mu\mu+$ jets background is estimated by extracting the $\not\!\!E_T$ fake rate from fully simulated Alpgen Monte Carlo and multiplying that by the number of observed $\mu\mu$ events in data.

Physics backgrounds are those in which the full signature from the top quark pair is mimicked at the particle level. These are $Z \to \tau\tau \to ll + 2\nu$s, $WW \to 2\ell + 2\nu$ and $WZ \to 3\ell + \nu$. The former is the dominant background for the $e\mu$ channel. These

backgrounds were estimated from Monte Carlo corrected for efficiencies measured in data.

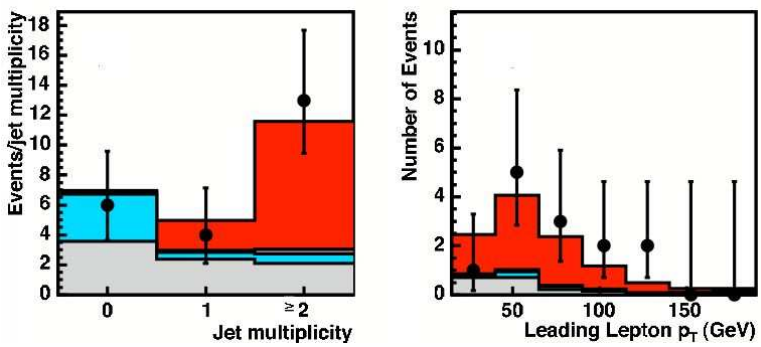

Fig. 4. Kinematic characteristics of dilepton events in 243 pb^{-1} of DØ data [73]. Event jet multiplicity (left) and leading lepton p_T (right) are shown. Data are indicated by points and error bars, and the sums of signal and background distributions are overlaid as solid histograms.

The cross section for $\sqrt{s} = 1.96$ TeV is taken by maximizing the likelihood among the three channels that, given a value of the assumed cross section, the estimated backgrounds and top quark efficiencies can produce the number of observed events. The cross section is $8.6^{+3.2}_{-2.7}(stat) \pm 1.1(sys) \pm 0.6(lum)$ pb. Fig. 4 indicates the jet multiplicity of the dilepton sample with all other selections applied. The excess of events over background in the 2-jet bin is consistent with the expected top quark contribution. Fig. 4 also provides the p_T distribution for the leading lepton in the final event sample. Kinematic distributions of dilepton events have been of some interest. The CDF collaboration has observed some unexpected properties of their dilepton samples in Run I and Run II[76]. The DØ distributions are consistent with standard model effects. The dominant uncertainties for the DØ measurement are roughly equal from lepton identification and triggering, and from jet reconstruction and energy scale.

This basic analysis has been performed in 425 pb^{-1} of data with somewhat modified selection on the $e\mu$ and $\mu\mu$ channels. In the latter case, substantial improvement was made in the rejection of Z bosons. Figure 5 shows the H_T distribution for the $e\mu$ data, and for $t\bar{t}$ and background expectations. Good agreement is observed and the statistical sample is starting to permit a fairly distinct $t\bar{t}$ component to become more evident. In combination with the ℓ+track channels described in the next section, a combined cross section measurement of $7.4 \pm 1.4(stat) \pm 1.0(sys)$ pb was obtained [77]. A preliminary result in 1 fb^{-1} from the dilepton and ℓ+track channels has given $6.2 \pm 0.9(stat)^{+0.8}_{-0.7}(sys) \pm 0.4(lum)$ pb [78]. These results are given in Table 5.

For Run II, CDF has analyzed an explicit dilepton data sample from 197 ± 12

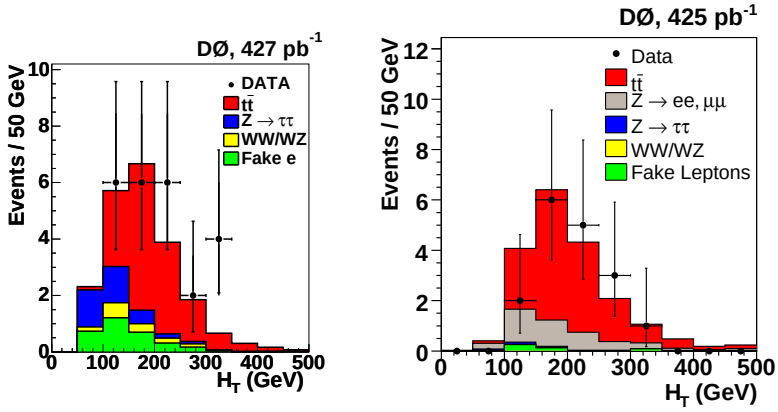

Fig. 5. Kinematic characteristics of dilepton and ℓ+track events in DØ analysis of 425 pb^{-1} sample [77]. Event H_T distributions are shown for the $e\mu$ channel (left) and the combined ℓ+track channel (right). Data are indicated by points with error bars, the estimated signal and background contributions are shown via overlaid histograms.

pb^{-1}[79]. Triggering involved one high p_T lepton, e or μ. In general, the CDF analyses are characterized by a common approach across channels which aids in background understanding and justification of event selection. The selection in Run II is similar to that used in Run I [80] (see combined measurement in Table 5). Top quark events were selected by requiring two leptons with $p_T > 20$ GeV, plus two energetic jets with $p_T > 15$ GeV and large $\not\!\!E_T$(>25 GeV). One of the two leptons must satisfy a tight selection, while the other may pass looser cuts. For both the ee and $\mu\mu$ channels, events are rejected if the dilepton invariant mass, M_{ll}, is near the Z boson mass, M_Z, to suppress Z backgrounds. The basic kinematic selection is given in Table 2. An opposite sign requirement for the two leptons is applied. Events were removed when $\Delta\phi(\not\!\!E_T, j)$ is small and when $\Delta\phi(\not\!\!E_T, \ell) < 20\,\mathrm{deg}$. CDF did not require that explicit and implicit channels have orthogonal event selection.

Remaining backgrounds from Z/γ^* were estimated by comparing the number of dilepton events in each jet multiplicity in the data and using that to normalize a fully simulated Pythia sample. Lepton instrumental backgrounds were estimated by folding fake rates measured in data with a sample selected to be kinematically signal-like, but without lepton identification selection on one of the leptons. Diboson backgrounds were estimated from events simulated with Alpgen plus Herwig or Pythia. Fig. 6 shows the $\not\!\!E_T$ and H_T distributions of the dilepton events after the application of all the selections.

The Run II explicit dilepton channels were incorporated into a $t\bar{t}$ cross section measurement from all dilepton channels, as shown in Table 5. In this channel, 13 events were observed with expected signal of 8.2 events and expected background of 2.7 events. Since the selections overlap, explicit channels have significant correlation

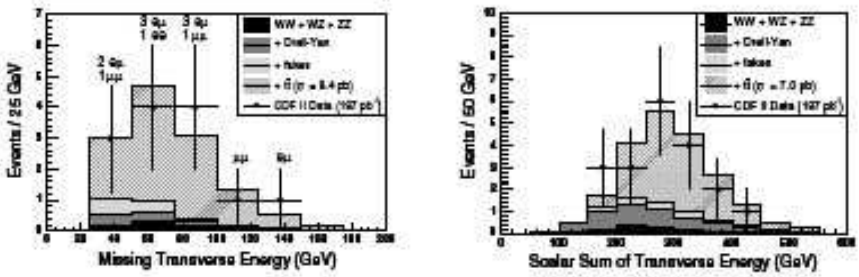

Fig. 6. Kinematic characteristics of dilepton events for CDF analysis in 197 pb^{-1}. The $\not\!\!E_T$ for explicit dilepton events (left) and the event H_T for ℓ+track events (right) are shown [79]. Data are indicated by points with error bars, and estimated signal and background contributions are shown via overlaid histograms.

with the implicit channels described in Section 4.3.2. The combined dilepton cross section for Run II is provided in Table 5. The cross section measurement was repeated for subsamples that have at least one $b-$tag, and that have two-tight leptons, and were found to be consistent with these results. Preliminary analyses of 360 pb^{-1} [81] and 1.2 fb^{-1} [82] have been pursued by CDF. The former combined both dilepton and ℓ+track measurements to obtain a cross-section of $8.5^{+2.6}_{-2.2}(stat)^{+0.7}_{-0.3}(sys)$ pb. The latter resulted in a measurement of $6.2 \pm 1.1(stat) \pm 0.7(sys) \pm 0.4$ pb.

4.3.2. *Implicit channels*

Analysis of a dilepton channel where one lepton is not identified began with an initial effort by DØ in Run I[74] which looked for one isolated, high p_T electron plus exceptionally high $\not\!\!E_T$. For a concise review of this analysis, see Ref. 3. A cross section for this channel alone was obtained to be 9.1 ± 7.2 pb, which is incorporated into the final DØ Run I result given in Table 5.

In Run II, CDF has performed a cross section measurement in 197 ± 12 pb^{-1} using an implicit dilepton selection[79]. A tight lepton (e or μ) was required with strict calorimeter, muon system or tracking requirements, and an isolation cut. Another high p_T track isolated from significant momentum in nearby tracks was also required. This lepton plus track (ℓ+track) approach provides measurement of all final state particles, aside from νs. Thus, top quark properties, such as m_t, can be measured with techniques appropriate to an explicit dilepton analysis. The cost of the looser lepton selection can be borne by tighter requirements on other quantities, such as jet E_T or jet $b-$tagging.

As with the explicit channels, $Z/\gamma*$ backgrounds were estimated by comparing the number of dilepton events in each jet multiplicity in the data and using that to normalize a PYTHIA plus full detector simulation sample. Instrumental backgrounds were extracted from a kinematically signal-like sample in data without final identi-

Table 2. Selection cuts for DØ and CDF Run II dilepton and ℓ+track cross section measurements. Variables are described in the text.

cut	CDF dilepton	CDF ℓ+track	DØ dilepton	DØ ℓ+track
$N_\ell(N_{tracks})$	2	1 (1)	2	1 (1)
$p_T^{\ell_2}$ (GeV)	> 20	> 20	> 15	> 15
$\lvert\eta_e\rvert$	< 2.0	< 2.0	< 2.5	< 2.5
$\lvert\eta_{\mu,track}\rvert$	< 1.0	< 1.0	< 2.0	< 2.0
$N_{jets}(N_{tags})$	$> 2(0)$	$> 2(0)$	$> 2(0)$	$> 1(1)$
p_T^j (GeV)	> 15	> 20	> 20	> 20
$\lvert\eta_j\rvert$	< 2.5	< 2.0	< 2.5	< 2.5
$\not{E}_T$ (GeV)	> 25	> 25	> 25	> 15 (e) > 25 (μ)
$\Delta\phi(\not{E}_T, j)$	$\neq 0$	$\neq 0$		
$\Delta\phi(\not{E}_T, \ell/track) >$	$20\deg w/l$	$5\deg w/track$	0.2 $w/\mu(e\mu)$ not $180\deg(\mu\mu)$	
H_T (GeV)	> 200	—	> 140 ($e\mu$)	—
Z rejection:				
$M_{\ell\ell}$ (GeV)	$76 - 106$	$76 - 106$	$80 - 100(ee)$	$70 - 100(e)$ $70 - 110(\mu)$
$\chi^2_{M_Z}$	—	—	$> 2(\mu\mu)$	—
$\not{E}_T$ near M_Z	∞	> 40	∞	> 20 (e) > 35 (μ)

fication cuts on one of the lepton candidates. Diboson backgrounds were estimated using ALPGEN with HERWIG or PYTHIA. The $t\bar{t}$ signal was simulated using PYTHIA.

The data yield 19 events for the ℓ+track selection with expected signal of 11.5 events and an expected background of 6.9 events. The implicit and explicit channels share a significant number of events. The combined dilepton cross section measurement is given in Table 5. The cross section measurement was repeated for $b-$tagged, and two-tight lepton subsamples and found to be consistent with these results. Preliminary analyses in 360 pb^{-1} and 1 fb^{-1} of data were performed for the ℓ+track channel. The former yielded a combined measurement with dilepton channels[81] as shown in Table 5. The 1fb^{-1} analysis provided a much more precise measurement of $8.3 \pm 1.3(stat) \pm 0.7(sys) \pm 0.5(lum)$ pb[82]. Figure 7 shows the agreement between the jet multiplicity and $\not{E}_T$ distributions for the 1fb^{-1} ℓ+track data and the signal and background expectations.

The DØ experiment has performed an ℓ+track analysis in 425 pb^{-1} of data[77]. At trigger level, single lepton plus jet triggers are employed. To offset the higher background resulting from the omission of the lepton identification cuts, $b-$tagging of jets using a secondary vertex algorithm is employed to produce a reasonable S/B. This allows the analysis to have significantly looser kinematic selection than DØś explicit dilepton channels. Signal and Z/γ^* samples are modeled using ALPGEN fed into PYTHIA. Diboson samples are modeled with PYTHIA. The primary background is instrumental from $Z \to ee, \mu\mu$ with fake $\not{E}_T$. The data and Monte Carlo $\not{E}_T$ distributions were observed to be in agreement, and so this background is extracted

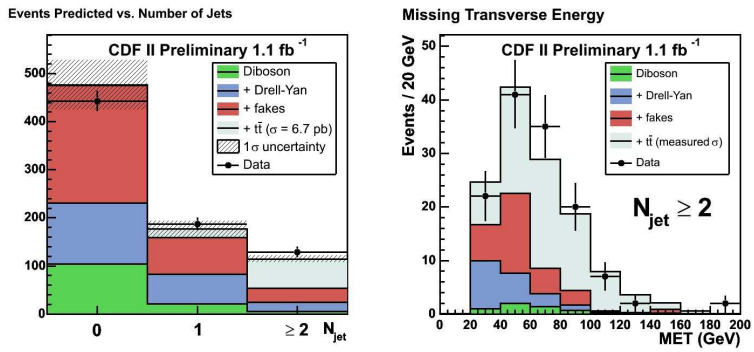

Fig. 7. Distributions of jet multiplicity in CDF ℓ+track events in the 1 fb^{-1} sample (left). The $\not\!\!E_T$ distribution is shown for two jet events (right). The data is indicated by points with errors, and signal and background expecations are overlaid. [82].

from the simulation after normalizing the event yield to that observed in the data for low $\not\!\!E_T$. A significant background from fake leptons or fake tracks exists for this analysis. This background is estimated in the untagged sample by constructing four samples in data with loose and tight selections on the lepton and track. From these samples, $b-$tag rates appropriate to W+jets events, and knowledge of lepton efficiencies and fake rates, the number of lepton instrumental backgrounds is inferred. Figure 5 shows the H_T distribution of ℓ+track events, with $t\bar{t}$ signal and background estimates overlaid. There is good agreement of these expectations with the data. The ℓ+track channel was also analyzed in a preliminary measurement in 1 fb^{-1}[78]. The $t\bar{t}$ cross sections determined in combination with the explicit dilepton channels are shown in Table 5.

4.4. *Single lepton channels*

Since top quark analyses have been statistically limited until recently, the extra rate has caused the ℓ+jets channel to be key in studying the entire top quark sector. Generally, backgrounds are easier to control if the lepton is an e or μ, although τ-based analyses have been implemented (e.g. Ref. 84). This section will concentrate on analyses using leptons of the first two generations.

With four quarks from $t\bar{t}$ decay, top quark events are fairly crowded in the central region of the detector. Initial state gluons can land near these quarks. Final state gluon radiation can take momentum away from the quarks. The resulting jets may overlap and get merged, or may split into extra jets. As a result, a substantial fraction of top quark events will exhibit only three jets, and a significant number will have more than four. The physics processes which can produce the ℓ+jets signature are W+jets production in association with jets and, at a much lower level, diboson (WW, WZ) production. Single top quark production is also a background to the ℓ+jets $t\bar{t}$ cross section measurement. The largest instrumental background comes from multijet production where the lepton and $\not\!\!E_T$ are fake.

Strategies for measuring top quark pair production in the ℓ+jets channel have employed three general techniques. At the selection level, the balance of efficiency and background level is crucial. A purely kinematic, or 'topological', approach uses the unique kinematic signature of the top quark to isolate it from background via a multiparameter discriminant. Semileptonic decays of b-quarks occur at a significant rate. The backgrounds do not have nearly as high a b-jet content as top quark events. So a second strategy involves use of the excellent capabilities of the DØ and CDF detectors to tag jets with leptons from semileptonic decay of $b-$quarks. The third strategy, which is the primary approach for the most precise measurements of the $t\bar{t}$ cross section, involves lifetime tagging $b-$jets to suppress backgrounds.

Table 3. Selection cuts for CDF and DØ Run II ℓ+jets cross section measurements.

cut	CDF $\ell + jets$	DØ $\ell + jets$
Trigger:	$1\ e, \mu$	$1\ e, \mu + 1$ jet
$b-$tag selection:		
p_T^l (GeV)	> 20	> 20
$\lvert\eta_e\rvert$	< 1.1	< 1.1
$\lvert\eta_\mu\rvert$	< 1.0	< 2.0
N_{jets}	> 3	> 3
p_T^j (GeV)	> 15	> 15
$\lvert\eta_j\rvert$	< 2.0	< 2.5
$\not{E}_T$ (GeV)	> 20	> 20
H_T (GeV)	> 200	> 0
topological:		
N_{jets}	> 3	> 4
H_T (GeV)	> 0	> 0
$\Delta\phi(\not{E}_T, j_1) \neq$	$0, \pi$	

4.4.1. *ℓ+jets Channels using kinematic selection*

The kinematics of the final state products from top quark decay are quite striking compared to those produced by other standard model processes. It is therefore natural that CDF and DØ have devised selections relying solely on these properties. In the ℓ+jets channel, the backgrounds are much higher than the dilepton channel. As a result, significantly more complex approaches have been required to isolate a clean signal. A value of such a selection is that it does not rely on the assumption that $BR(t \to Wb) = 1.0$. Sensitivity is retained for models which produce different final state jet flavor content (e.g. Ref. 85).

The initial untagged ℓ+jets analyses were performed by DØ in Run I and contributed the primary significance to their top quark discovery analysis[1]. This laid the basis for a final measurement at $\sqrt{s} = 1.8$ TeV[74], as well as a measurement with 226 pb^{-1} of data at $\sqrt{s} = 1.96$ TeV[87]. To control backgrounds, four jets were

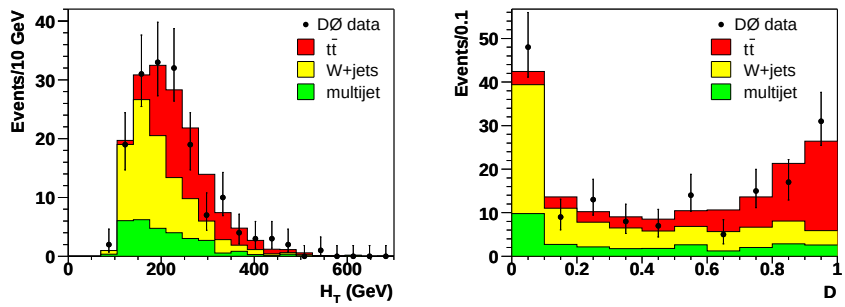

Fig. 8. Distribution of H_T for combined ℓ+jets events in 230 pb^{-1} of DØ Run II data (left). The sum of $t\bar{t}$ and backgrounds are overlaid. At right is the multi-parameter likelihood discriminant for data and also overlaid with signal and background expectation[87].

required. The specific event selection used in the Run II analysis can be obtained from Table 3. The $t\bar{t}$ acceptance and efficiencies were estimated from the Monte Carlo.

Theoretical calculations yield substantial uncertainties in the production of background processes. As a result, methods are needed by which the normalization of the background can be calculated from data. The multijet background kinematic shapes were taken from the data by requiring the lepton to fail the tight identification requirement. To estimate the normalization of the background and signal estimates, two steps were employed. First, loose and tight cuts for the lepton identification were defined to permit a variation of the level of QCD multijet background relative to the W processes (W+jets and $t\bar{t}$). Efficiences for real leptons and the fake leptons in the QCD sample were measured in data. Then one can solve the resulting two event yield equations in two unknowns: N_s for top quark plus W events, and N_b for the multijet yield. This is termed the 'matrix method'. In Run I, the apparent scaling of jet multiplicity (sometimes called 'Berends scaling' [90]) was used to anchor the W+ four jet multiplicity normalization with the yields observed for background-rich low jet multiplicities. The Run II measurement, however, extracts the level of multijet background from the matrix method and obtains the W normalization as described in the next paragraph. The W+jets kinematic shapes are taken from the Monte Carlo.

A multiparameter discriminant was constructed to identify the top quark signal in the data. For the Run II analysis, this was formed from six observables: H_T, $\Delta\phi(\not{E}_T, \ell)$, $\mathcal{C}$, $\mathcal{S}$, $\mathcal{A}$ and $K_{Tmin} = \Delta R_{jj}^{min} p_T^{min}/E_T^W$. The latter is calculated by determining the jet pair with minimum separation in $\eta - \phi$ (ΔR_{jj}^{min}), the p_T of the second leading jet of that pair, and the scalar sum of the lepton and $\not{E}_T$, E_T^W. The discriminant function is:

$$D = [\Pi_i s_i(x_i)/b_i(x_i)]/[\Pi_i s_i(x_i)/b_i(x_i) + 1] \tag{2}$$

where s_i and b_i are the normalized distribution for each variable, i, for signal and

background, respectively. An assumption was made of uncorrelated variables. Figure 8 shows the event H_T and the likelihood discriminant for data with $t\bar{t}$ signal and background superimposed. The discriminant function in data was fit to extract a measurement of $\sigma_{t\bar{t}}$ and the number of W backgrounds. The measurement for $\sqrt{s} = 1.96$ TeV was $\sigma_{t\bar{t}} = 6.7^{+1.4}_{-1.3}(stat)^{+1.6}_{-1.1}(sys) \pm 0.4(lum)$ pb[87]. This analysis has been updated in 425 pb^{-1} to yield $\sigma_{t\bar{t}} = 6.4^{+1.3}_{-1.2}(stat) \pm 0.7(sys) \pm 0.4(lum)$ pb [88]. A preliminary result using 900 pb^{-1} has also been obtained [89]. Statistical uncertainties of approximately 15% are being achieved, and the measurement in the latter sample was $6.3^{+0.9}_{-0.8}(stat) \pm 0.7(sys) \pm 0.4(lum)$ pb.

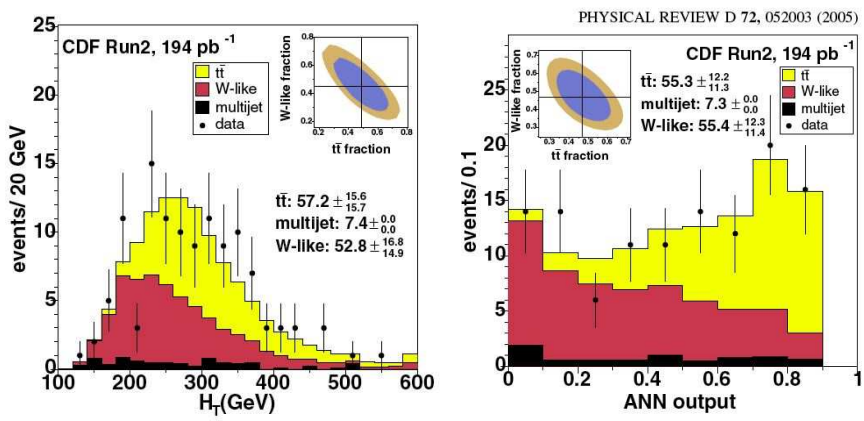

Fig. 9. Distribution of H_T for combined ℓ+jets events in CDF data (left). The sum of $t\bar{t}$ and backgrounds are overlaid. At right is the likelihood for data and also overlaid with signal and background expectation[86].

CDF pursued this 'topological' approach with 194 pb^{-1} of collisions at $\sqrt{s} = 1.96$ TeV[86]. Only three jets were required. Events were rejected if $\Delta\phi(\not{E}_T, j_1) \sim 0$ or π. The W+jets background shape is extracted from the Monte Carlo, and the normalization is obtained by maximizing a binned likelihood:

$$L(\bar{n}_{t\bar{t}}, \bar{n}_W, \bar{n}_q) = \Pi_{i=1}^{N_{bins}}(e^{-\bar{n}}\bar{n}_i^{d_i})/d_i! \tag{3}$$

where the $\bar{n}$'s are the means for top quark ($\bar{n}_{t\bar{t}}$), W ($\bar{n}_W$) and QCD ($\bar{n}_q$) yields, and $\bar{n}_i$ expresses the expected number of events in an ith bin given the probabilities for the signal and background contributions to populate that bin. d_i is the number of events observed in the ith bin. The value of $\bar{n}_q$ is fixed based on a 'sideband' method where the data are divided into quadrants in the lepton isolation versus $\not{E}_T$ plane. The number of events with non-isolated leptons and high $\not{E}_T$ is scaled by the ratio of isolated-to-non-isolated events in a W-poor, low $\not{E}_T$ region. The value of $\bar{n}_{t\bar{t}}$ extracted from the fit is used to determine $\sigma_{t\bar{t}} = \bar{n}_{t\bar{t}}/\epsilon_{t\bar{t}}\mathcal{L}$. The cross section is calculated using two different kinematic discriminants: H_T and a variable from a

seven-parameter artificial neural network technique. The parameters were: H_T, $\mathcal{A}$, $1/\mathcal{C}$, the minimum dijet mass from the three leading jets M_{jj}^{min}, the pseudorapidity of the leading jet η^{j1}, the minimum $\eta - \phi$ separation of two jets among the leading three, and the H_T calculated from the third leading and lower p_T jets. The values of both of the discriminants for the data sample, with signal and background superimposed, are shown in Fig. 9. The neural network approach included additional information besides H_T to provide approximately 30% better statistical uncertainty than H_T alone. These variables were each cross checked in the W+jets samples. The cross section was actually estimated using these and other kinematic variables individually (see Fig. 10), and a full range of systematic uncertainties were obtained for the H_T case in the three-jet and four-jet inclusive bins. The full analysis provided a measured cross section of $6.6 \pm 1.1(\text{stat}) \pm 1.5(\text{sys})$ pb.

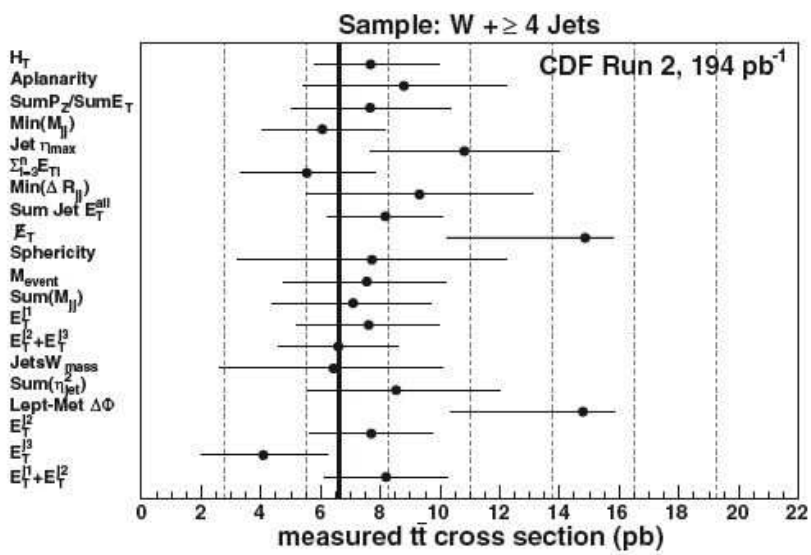

Fig. 10. Cross section for $t\bar{t}$ in 194 pb^{-1} of $\ell + 4$jets events considering topological properties of events[86].

ℓ+jets Channels using soft lepton tagging

Hadrons containing $b-$quarks undergo semileptonic decay at a rate of approximately 17% for each charged lepton type. When decays through $c-$quarks are included, approximately 40% of $t\bar{t}$ events have a soft non-isolated μ, for instance. In contrast, typical background processes produce primarily 'light flavor' partons ($u/d/s$ quarks and gluons) and the heavy flavor contribution is small. So requiring a soft lepton in a jet can provide a strong background suppression. While the unbiased flavor selection is important in its generality, the ability to demonstrate the presence of $b-$quarks

in the top quark candidate sample has also been crucial to validate whether the observed signal adhered to standard model expectations.

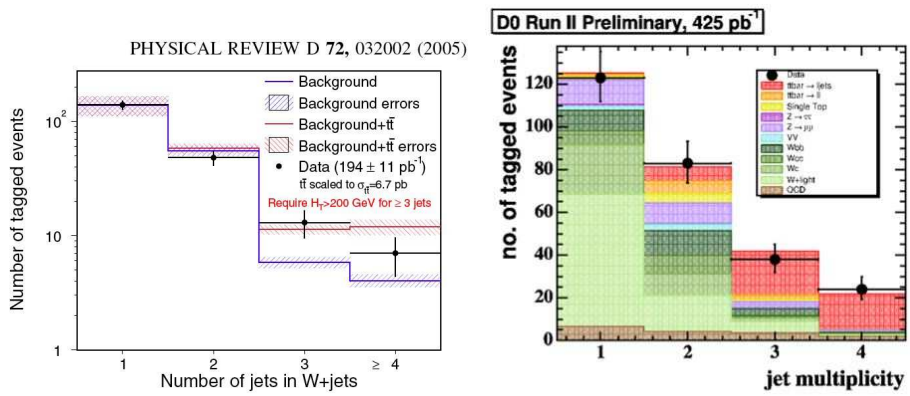

Fig. 11. Jet multiplicity distribution for CDF 194 pb^{-1} soft-lepton tagged data sample (left) [92]. Estimated backgrounds are overlaid as a solid histogram. At right is the DØ distribution in a preliminary analysis of 425 pb^{-1} of data[94].

Both Tevatron experiments have pursued strategies of selecting events where at least one jet is 'tagged' with a soft, non-isolated lepton. CDF has produced estimates of $\sigma_{t\bar{t}}$ using both soft muon and soft electron semileptonic decay modes[91]. In Run II, the soft muon variant was employed in 194 pb^{-1} of data[92]. In order to optimize their analysis, CDF chose a cut on $H_T > 200$ GeV that maximizes the significance of signal $= S/\sqrt{S+B}$.

Signal efficiencies were estimated in Monte Carlo with tag efficiencies scaled from data. In the Run I analysis, efficiencies for leptons from heavy flavor, as well as backgrounds, were estimated using inclusive jet events from data. Cross checks were performed in a sample of $Z \to \ell\ell + jets$ events with soft lepton and secondary vertex tags which have a much smaller fraction of top quark signal. The calculated yield from background in these channels agreed well with observed numbers. In Run II, the W and QCD backgrounds are estimated from data in two steps. The multijet background is estimated with the sideband method mentioned above. The product of this yield with the correct tag rate gives the background estimate. The applicability of the measured tag rate for the W component of the background is verified by using it to estimate the tagged yield in several different jet samples. By comparing this estimate with the observed tagged event statistics, the rates are validated. The final W+jets yield is estimated using untagged samples corrected for the expected QCD contribution and multiplied by the mistag rate from γ+jet events. Other backgrounds are much smaller than the W and QCD backgrounds.

Dominant systematic uncertainties arise from the modeling of top quark acceptance as well as the signal and background tag rate estimates. The jet multiplicity

distribution for the data, as well as the estimated backgrounds are shown in Fig. 11. The final cross section estimate for $\sqrt{s} = 1.96$ TeV is $5.3 \pm 3.3(stat)^{+1.3}_{-1.0}(sys)$ pb. A preliminary measurement of the $\sigma_{t\bar{t}}$ in 760 pb^{-1} of $\mu-$tag events has also been executed by CDF, yielding a value of $7.8 \pm 1.7(stat)^{+1.1}_{-1.0}(sys)$ pb [93].

Soft muon tagging has also been utilized by DØ to identify $b-$jets in $\ell+jets$ data from both Tevatron runs. The Run II analysis[94] constitutes a preliminary result in 425 pb^{-1} of collider data. These analyses benefited from the large coverage of the muon system ($|\eta| < 2.0$ in Run II). They also benefited from the depth in interaction lengths of the material in front of the muon chambers, particularly the layers outside of the muon iron toroid, which reduced the instrumental fake muon background to exceptionally low levels. Only three jets were required. The Run II analysis improves over the earlier one by no longer requiring an H_T cut or a selection for the $\mu + jets/\mu - tag$ channel of a cut on the χ^2 of a kinematic fit to a $Z \to \mu\mu$ hypothesis.

Signal and physics background (W+jets, diboson and single top quark events) efficiencies and yields were estimated using Alpgen plus CTEQ5L and Pythia. The primary backgrounds are: $Z \to \mu\mu$ where one μ is lost or overlays a jet and mimics a $b-$tag, QCD multijet background, and W+jets. The former was obtained from Monte Carlo but the yield was normalized using the measured Z boson cross section. The multijet background in the tagged sample was isolated from the $W-$like events, which include W+jets and $t\bar{t}$ components, using the 'matrix method'. W+jets events were estimated by extracting the yield from the same method in the untagged sample. The Monte Carlo was used to ascertain the flavor composition of this sample. This is an improvement over the Run I approach in which the event kinematic shapes were also extracted from the Vecbos Monte Carlo. The appropriate tagging efficiencies or mistag rates for each flavor component were corrected to reflect performance in data and applied to the untagged yield. The jet multiplicity distribution of the selected sample is shown in Fig. 11.

The cross section was determined from a maximum likelihood fit to the observed number of events in three and four jet samples of the e+jets and μ+jets channels. In each subsample, the backgrounds were constrained by the values from the matrix method. A gaussian term was used for each systematic uncertainty such that the mean cross section could shift if the expected signal and backgrounds were varied over the ranges allowed by the uncertainties. The cross section was measured to be $7.3^{+2.0}_{-1.8}(stat + sys) \pm 0.4(lum)$ pb.

ℓ+jets Channels using secondary vertex tagging

Displaced vertex $b-$tagging as applied to top quark candidate samples was first performed by CDF in the analysis of 1.8 TeV collisions[2]. An initial cross section measurement from CDF using Run II data[95,96] employed a ℓ+jets selection with at least one jet tagged with a secondary vertex using 162 ± 10 pb^{-1}. The leading jet p_T was used as a discriminating variable in a likelihood to extract a top quark fraction

in data. The shape of the W boson p_T spectrum was obtained by selecting a W+jets sample in data where no jets were $b-$tagged to reduce top quark contamination. The instrumental background was obtained in the high $\not\!\!E_T$ sample by reversing the isolation cut on the lepton. The kinematic distributions were observed to be insensitive to the heavy flavor composition of the sample. To validate the background model, untagged $W+$ one or two jets events were scaled by the tag rate. Agreement with the b-tagged sample in data was observed in the jet p_T distribution. An unbinned likelihood fit was performed to the observed jet p_T distribution given the expected signal and background shapes. A signal fraction of $R_{fit} = 0.68^{+0.14}_{-0.18}$ was obtained. The top quark cross section was obtained from $\sigma(t\bar{t}) = N_{obs}R_{fit}/A_{t\bar{t}}\epsilon_{t\bar{t}}L$ where A is the signal acceptance, $\epsilon_{t\bar{t}}$ is the estimated efficiency, and N_{obs} is the observed yield of events in data. The systematic uncertainty for this analysis is dominated by that from the jet energy scale calibration. Other significant contributors come from the $b-$tagging efficiency and the luminosity estimate. The estimated cross section and uncertainty are $6.0 \pm 1.6(\text{stat}) \pm 1.2(\text{sys})$ pb and are given in Table 5.

In order to employ ℓ+jets events in measurements beyond the cross section, a more general approach is needed to determine backgrounds. CDF has used a method in 162 pb^{-1} of data which is more similar with the lifetime tagging approach in Run I [97,98]. The background estimation method was designed to account for the different flavor compositions of multijet and W+jets samples. The fraction of the W+jets background that contains heavy flavor was estimated from Monte Carlo. The mistag rate was applied to the QCD background and to the fraction of W+jets background not arising from $b\bar{b}$ and $c\bar{c}$ associated production. The measured heavy flavor tag rate was applied to the estimated $W+$ heavy flavor jet fraction. In Run I, this approach provided good agreement of background estimation and observed yield in $W+$ one and two jet samples. In combination with the soft-lepton tag selection, the b-tagged Z+jets sample was also observed to provide agreement between observed and expectation at all jet multiplicities.

Signal efficiencies were calculated after correcting for the observed ratio of the tag rate for jets tagged with soft electrons in data and a parallel Herwig sample. Systematic uncertainties include the residual flavor composition of the data sample, as well as potential differences between soft electron tagged $b-$jets vs. $b-$jets generally. The multijet background was estimated in tagged and untagged samples using the sideband method in the $\not\!\!E_T$ vs. lepton isolation plane. The heavy flavor fraction of the W+jets background was estimated from Monte Carlo. This fraction was calibrated using an MC-to-data correction factor based on data and MC jet samples. The yield of $W+$ heavy flavor events was estimated by multiplying the heavy flavor fraction by the number of events in the untagged sample, and then applying the $b-$tag efficiencies to that. Mistagged W+jets background was estimated by weighting each jet in the untagged sample by the mistag rate. A correction was applied to remove the estimated QCD multijet background in this sample. Other small backgrounds were estimated from the Monte Carlo. The background estimation method for the W+jets sample was cross-checked by applying similar

techniques to a Z+jets sample where there would be little top quark contribution. Agreement of data with the expected background contributions was observed. The cross section was estimated in the single tag sample to be $5.6^{+1.2}_{-1.1}(stat)^{+0.9}_{-0.6}(sys)$ pb. A measurement carried out in the double-tag sample was consistent.

Using a larger data sample of 318 pb^{-1}, CDF has produced an extensive suite of measurements with different tagging treatments. The secondary vertexing scheme was updated using a newer tagger that has higher efficiency, particularly at high p_T [101]. Event selection remained the same. The signal efficiencies and background estimates were also performed similarly to the earlier analysis. The primary exception was that the backgrounds were adjusted with an iterative algorithm to correct for the top quark contribution in their control samples until the cross section measurement varied by less than a percent. The cross section result was $8.7\pm0.9(stat)^{+1.1}_{-0.9}(sys)$ pb. A complete measurement was also performed in the same data sample with a jet probability tagger[102]. Two different selections ($< 1\%, < 5\%$) were used to vary the purity and check the consistency of their results. Event selection was the same as in the secondary vertex analysis with the addition of a cut on the transverse mass of the $l\nu$ pair $M_T^W > 20$ GeV. Signal efficiency and background levels were estimated as in the secondary vertex tag analyses. For the multijet background, the definitions of the sidebands were adjusted to provide a 50% systematic uncertainty in both the untagged and tagged samples. Control samples of events with one or two jets validated the background modeling approach. The background estimate was corrected iteratively to account for top quark contamination until the cross section measurement was stable to within 0.1%. For the most sensitive jet probability tag selections, the cross section is $8.9 \pm 1.0(stat)^{+1.1}_{-1.0}(sys)$ pb. Cross sections measured in the separated electron and muon channels, and in the double-tagged subsample, are all consistent with these results. The results in 318 pb^{-1} are somewhat higher than the theoretical value. Cross checks in the data using the earlier secondary vertex algorithm, as well as looking in the double tagged sample provided consistent values of the cross section. In 1.1 fb^{-1} of ℓ+jets events, CDF has produced a preliminary measurement with substantially better statistical precision: $8.2 \pm 0.5(stat) \pm 0.8(sys) \pm 0.5$ pb [99].

DØ has published two determinations of the cross section in collisions at $\sqrt{s} = 1.96$ TeV using single lepton channels with secondary vertex tagging. The first utilized 230 pb^{-1} of collider data[100], and the second incorporated 425 pb^{-1} [103]. A preliminary result based on 900 pb^{-1} has also been pursued [104]. Trigger requirements of one lepton and one jet are the same as for the ℓ+jets analysis with topological selection. The data were separated into events with single tags, and double tags.

In the 230 pb^{-1} analysis, signal efficiencies were established by applying a tag rate from soft muon tagged dijet events corrected from a Monte Carlo study so that it applied to inclusive $b-$jets. The simulation also provided the $c-$jet tagging rate, and that was corrected for the semileptonic tag efficiency in data vs. Monte Carlo.

For the 425 pb^{-1} measurement, separate multijet samples were defined which had different levels of $b-$jet content. One required a non-isolated μ in one jet of a dijet pair, the other was the subset of this sample which also had a secondary vertex tag of the jet opposite this μ. Event yields were extracted in subsets of these two samples with and without either lifetime or soft-lepton tags. Eight equations were formed from these yields which allow the extraction of the b-tagging efficiency for semileptonically decaying b-quarks. The tagging efficiency for inclusive $b-$jets was obtained from $b\bar{b}$ Monte Carlo and scaled to a factor from the same eight equation separation scheme.

To estimate the multijet background, the matrix method was employed in tagged and untagged events. All other backgrounds, including Z+jets and diboson components, were estimated from the simulation. NLO calculations of cross sections were used to normalize the rates of these backgrounds. The W+jets background was found by subtracting the above contributions from the untagged sample and then multiplying the remainder by the tag rate appropriate to the flavor mix in W+jets events. This composition is evaluated from the ALPGEN W+jets simulation. In the 425 pb^{-1} analysis, an alternative parton matching scheme was used to estimate a 20% systematic uncertainty on the flavor fractions of the W+jets sample.

For the 230 pb^{-1} analysis, Fig. 12 illustrates the distributions for H_T and a multiparameter kinematic discriminant for data, signal and background expectations.

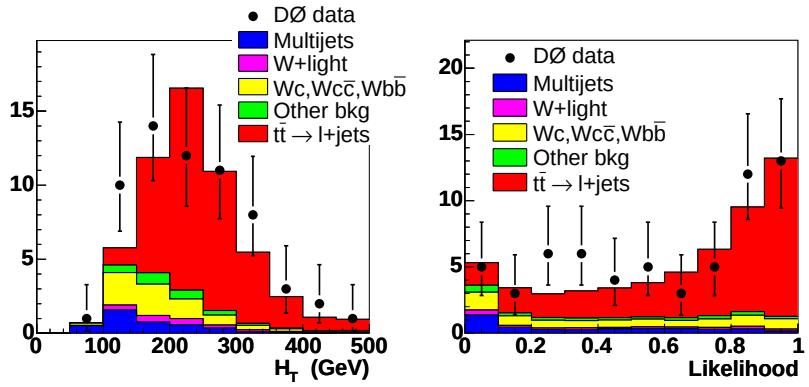

Fig. 12. Distribution of event H_T (left) for the DØ ℓ+jets 230 pb^{-1} sample with secondary vertex tag, and likelihood (right)[100]. Data are indicated with points and error bars, while the expectation for signal plus background are shown via solid histograms.

Figure 13 shows the jet multiplicity distribution for the single tag and double tagged samples in the 425 pb^{-1} analysis. The one-jet and two-jet bins exhibit good agreement with the expectation, thus validating the background estimation method. An excess is observed in the three and four jet bins which is attributed to top quark production.

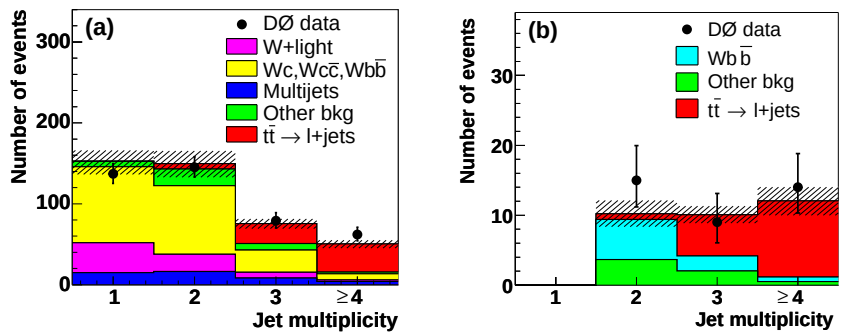

Fig. 13. The jet multiplicity distribution for the DØ 425 pb^{-1} ℓ+jets sample with secondary vertex tag for single tagged (left) and double tagged (right) events[103]. Data are indicated by points and error bars, while signal and background expectations are shown via solid histograms.

The measured cross section from the earlier data sample is $8.6^{+1.6}_{-1.5}(stat+sys) \pm 0.6(lum)$ pb. An alternative approach using an impact parameter tag was also used to calculate the cross section. This method produces very compatible results with the secondary vertex approach and is actually fairly uncorrelated with it in terms of event sample. As with the soft-lepton tag analysis in 425 pb^{-1}, the cross section was extracted by maximizing a likelihood given the observed number of events. Each systematic uncertainty was implemented as a Gaussian which could alter the fitted cross section. This provided a cross section measurement of $6.6 \pm 0.9(stat+sys) \pm 0.4(lum)$ pb. The measurement in 900 pb^{-1} uses much the same techniques and gives $8.3^{+0.6}_{-0.5}(stat)^{+0.9}_{-1.0}(sys) \pm 0.5(lum)$ pb.

Substantial uncertainties for all DØ and CDF single lepton mode analyses arise from tagging efficiency uncertainty, and from the jet energy scale uncertainty. In addition, the secondary vertex analyses have significant uncertainty from the background modeling. Both CDF results have approximately a five percent lepton identification uncertainty. The 425 pb^{-1} DØ measurement has significant uncertainties from *pdf*'s, factorization scale and heavy quark (b and c) mass.

4.5. *All-jets channel*

The all-jets channel is the most copious $t\bar{t}$ final state with a branching fraction of $\sim$46%. Without any energetic neutrinos in the final state, the all-jets mode is also the most kinematically constrained, and this allows a full reconstruction of the $t\bar{t}$ signal. However, the signal suffers from an overwhelming background from QCD multijet production, with a cross section many orders of magnitude larger, making the extraction of $t\bar{t}$ events extremely challenging. To improve the signal-to-background ratio, S/B, a set of requirements exploiting the kinematic and topological characteristics of standard model $t\bar{t}$ events is applied to the data. Unlike the ℓ+jets topological selection described in Section 4.4.1, kinematic properties alone are not

sufficient to isolate the top quark. They are coupled with the use of $b-$tagging to separate the heavy-flavor poor background from the $t\bar{t}$ signal. The CDF and DØ experiments have previously measured the $t\bar{t}$ production cross section ($\sigma_{t\bar{t}}$) in the all hadronic channel in Run I[105,106]. The strategies employed by their measurements in Run II [107,108] rely heavily on the techniques developed during their Run I analyses. Table 4 gives an overview of the various selection requirements applied by the CDF and DØ analysis discussed in this section.

Table 4. Selection cuts for Run II all-jets cross section measurements by CDF[107] and DØ [108].

cuts	CDF	DØ
preselection		
primary event vertex ($Z_{vert} <$)	60 cm	50 cm
lepton veto	yes	yes
$p_T^{jets} >$ (GeV)	15	15
$\eta^{jets} <$	2	2.5
$N_{jets} \geq$	6	6
$H_T^{jets} >$ (GeV)	125	90
topological selection		
variables	H_T^{3j}, $\sum E_T$ C,A (kinematic selection)	H_T, A, $E_T^{5,6}$ $< \eta^2 >$, $M_{min}^{3,4}$, $\mathcal{M}$ (neural net selection)
$b-$ tagging	yes	yes

Discriminating event characteristics

In addition to the discriminating variables already discussed in section 4.1, the all-jets channels also employ some more jet-based variables. The QCD multijet production is dominated by a $2 \rightarrow 2$ parton process producing two hard leading jets with extra jets produced through gluon radiation. Therefore, the additional jets are expected to be softer in QCD background than in $t\bar{t}$ signal. The parameters used are H_T^{3j}, the scalar sum of all jet p_T's except the two leading jets, and $E_T^{5,6}$, the geometric mean of the transverse energies of the 5th and 6th leading jets. The properties which are typical for the top quark event structure, owing to the presence of W-bosons and b-quarks, are also used. The variables used are the mass-likelihood $\mathcal{M}$ and the second-smallest dijet mass in the event M_{min}^{2nd}. $\mathcal{M}$ is defined as $\mathcal{M} = (M_{W_1} - M_W)^2/\sigma_{M_W}^2 + (M_{W_2} - M_W)^2\sigma_{M_W}^2 + (m_{t_1} - m_{t_2})^2/\sigma_{m_t}^2$ where M_{W_1} (M_{W_2}) is the mass of the two jets corresponding to the W boson from the first (second) top quark, of mass m_{t_1} (m_{t_2}). The parameters $M_W = 79$ GeV and $\sigma_{M_W} = 11$ GeV are the central value and resolution of W boson mass peak, obtained from $t\bar{t}$ all-hadronic Monte Carlo along with the resolution of the top quark mass, $\sigma_{m_t} =$

21 GeV. $\mathcal{M}$ is calculated for each possible assignment of jets to the Ws and b-quarks, while only the permutation with the smallest $\mathcal{M}$ is used as the discriminator. $\mathcal{M}$ provides good discrimination between signal and background by requiring two jet pairs that are consistent with the W boson mass, and two W+jet pairs that are consistent with a single top quark mass of any value. The presence of two W bosons in $t\bar{t}$ events provides significant rejection against the QCD background. A further requirement that the two reconstructed top quarks have equal masses provides some additional discrimination. The discriminating performance of the two chosen kinematic variables, $\sum E_T$ and $\mathcal{C}$ can be seen in Fig. 14.

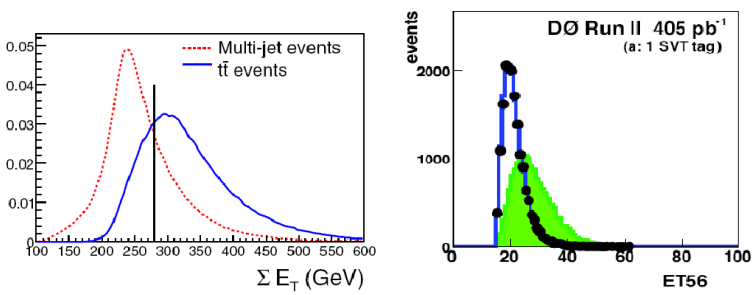

Fig. 14. Kinematic variable distributions ($\sum E_T$ (left) used by CDF analysis[107] and $\sum E_T^{56}$ (right) used by DØ analysis[108]) in multijet data and $t\bar{t}$ Monte Carlo simulation.

Measurement by CDF:

In Run II, CDF[107] has performed the measurement of the $t\bar{t}$ cross section ($\sigma_{t\bar{t}}$) in this channel utilizing approximately 311 pb^{-1} of data sample selected by dedicated multijet triggers. Events with at least four jets with p_T ≥10 GeV and large H_T ≥125 GeV are selected at the trigger level with S/B ∼1/3500. The offline preliminary signal selection requires events with a large jet multiplicity, $6 \leq N_{jets} \leq 8$, with p_T ≥15 GeV and $|\eta|$ <2. Application of a veto on isolated high-p_T leptons allow to keep the analysis orthogonal to those involving leptonic channels. After these requirements 364,006 events are selected for further analysis.

The $t\bar{t}$ events are modeled with PYTHIA and HERWIG using m_t =178 GeV. In order to improve the S/B, the analysis employs a kinematic and topological event selection based on H_T, H_T^{3j}, $\mathcal{C}$, and $\mathcal{A}$ optimized to achieve the maximum signal significance for $t\bar{t}$ events, defined as the ratio between the expected signal and the statistical uncertainty on the sum of the signal and background. The values for the cuts after optimization are: $\mathcal{A} + 0.005 H_T^{3j}$ ≥0.96, $\mathcal{C}$ ≥0.78, and H_T >280 GeV. Application of the kinematic selection yields 3315 events in data with an efficiency of 6.7±1.4% for the $t\bar{t}$ signal and a S/B ∼1/25. In order to further enrich the sample

with top-like events, events are required to have at least one $b-$tagged jet which leaves 695 events containing 816 $b-$tags, thus reaching a S/B of about 1/5.

The background sources for this final state are due mainly to QCD production of heavy quark pairs ($b\bar{b}$ and $c\bar{c}$) and false tags from light-quark jets. The mistag rate is evaluated in the exclusive four jet data sample before the kinematic selection and is parameterized in terms of jet E_T, track multiplicity N_{trk}, and number of primary vertices in the event N_{vert}. To estimate the background, each multijet event in the signal sample is weighted by its $b-$tag probability. The sum of these weights for the multijet events gives the expected number of tags from the non-signal processes. Before the kinematic selection, when the multijet sample is still predominantly composed of background events only, the predicted and observed number of tagged jets for different jet multiplicities agree very well as can be seen in Fig. 15, giving confidence in the constructed mistag rate.

The cross section measurement is performed using the total number of tagged jets (not events) in order to avoid the explicit calculation of the background for double tagged events. The average number of tags in a $t\bar{t}$ event passing the kinematic selection is $n_{tag}^{ave} = 0.846\pm\ 0.073$, measured in $t\bar{t}$ simulation by taking into account the different tagging efficiencies for $b-$, $c-$ and light-flavored-jets and correcting for the difference in efficiencies in data and Monte Carlo events. After application of the kinematic selection, a total of N_{obs} =816 candidate tags are observed, whereas the expected number of tags from background sources in the signal region amounts to N_{bkg}=684±38 tags, after correcting for the presence of $t\bar{t}$ events in the pretag sample. The resulting excess in data of tagged jets in the signal region is ascribed to $t\bar{t}$ production. The $t\bar{t}$ production cross section is determined by $\sigma_{t\bar{t}} = \frac{N_{obs}-N_{bkg}}{\epsilon_{kin}\times n_{tag}^{ave}\times\mathcal{L}}$ and is found to be $\sigma_{t\bar{t}} = 7.5 \pm 2.1(stat.)^{+3.3}_{-2.2}(sys)^{+0.5}_{-0.4}(lum)$ pb for m_{top}=178 GeV. The dominant systematic uncertainty of ∼20% arises from the dependence of selection efficiency on the jet energy scale. In Fig. 15, the distribution of the number of observed tags and background is compared to the $t\bar{t}$ signal expectation assuming the measured cross-section 7.5 pb.

Measurement by DØ :

In Run II, DØ [108] has measured the $t\bar{t}$ cross section ($\sigma_{t\bar{t}}$) in this channel based on ∼405 pb^{-1} of data collected using specific multijet trigger. The analysis proceeds on a methodology similar to that used in Run I[105]. In addition to the single-tagged events, the measurement has been extended to the double-tagged events. The analysis proceeds with the preselected data sample composed of events with ≥6 reconstructed jets with p_T ≥15 GeV, $|\eta|$ <2.5 and H_T >90 GeV. The bulk of the background is rejected by requiring the presence of secondary vertex tagged jets In order to maximize acceptance and sensitivity, separate samples with one tagged jet, or two tagged jets were analyzed. In the former, a tight requirement ($L_{xy}/\sigma_{L_{xy}} > 7$) was placed on the tag to control backgrounds. In the latter case, a looser requirement ($L_{xy}/\sigma_{L_{xy}} > 5$) was used to maximize efficiency.

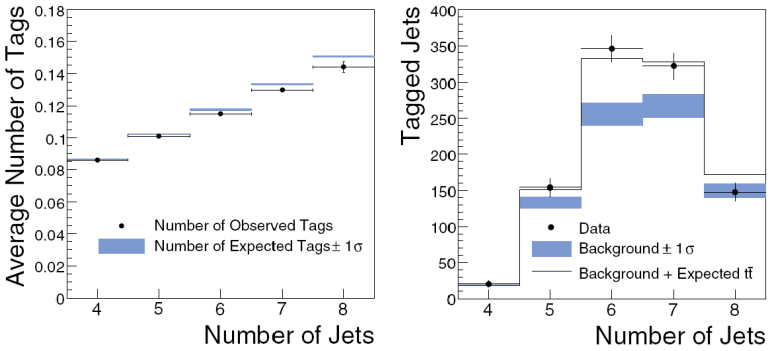

Fig. 15. Left: Average number of tags per event observed in the multijet sample before kinematic selection compared with the estimate from the tag rate parameterization in the CDF analysis[107]. Right: Number of tags observed in multijet data after kinematic selection compared with the expected background in the CDF analysis[107]. The $t\bar{t}$ expectation refers to the measured cross-section of 7.5 pb.

Further suppression of the multijet background is achieved by applying a neural network (NN) selection based on six discriminating kinematic variables: H_T, $\mathcal{A}$, $E_T^{5,6}$, $< \eta^2 >$, $M_{min}^{3,4}$, $\mathcal{M}$, taken from the equivalent Run I analysis[105].

The NN is trained to force its output near 1 for $t\bar{t}$ events and near -1 for QCD multijet events, using the multilayer perceptron network in the ROOT analysis program[109]. The very small S/B in the untagged data sample provided the background input for the training of NN, while $t\bar{t}$ Monte Carlo simulation using ALPGEN and PYTHIA with m_t =175 GeV was used for the signal. Fig. 16 shows the performance of the NN in discriminating $t\bar{t}$ signal from the multijet background for both single- and double-tag samples. The NN distributions vary for the two samples due to the variation of their flavor content. Overall, the NN displays significant discriminating power for the single- and double-tag events, although it exhibits a better discrimination for single-tag samples.

The top quark cross section is extracted from the output of the NN. The background dominated preselected sample is used to estimate the background. For the loose and tight tags, the mistag rate is derived from the data with $N_{tags} \leq$1. It is parameterized in terms of the p_T, rapidity y, azimuthal angle ϕ of the jet and the location of primary vertex along the beam direction z_{PV}, in four different H_T bins. Fig. 17 show the distributions of the NN output for the data, the Monte Carlo simulation prediction for $\sigma_{t\bar{t}}$ =6.5 pb, the predicted background, and the predicted signal+background. It can be seen that background keeps dominating over the signal even at large values of NN. The output of the NN is used to select the sample enriched in $t\bar{t}$ signal by applying the cut $NN \geq$0.81 (0.78) for the single (double)-tag analysis, optimized to minimize the fractional statistical error on the cross section measurement.

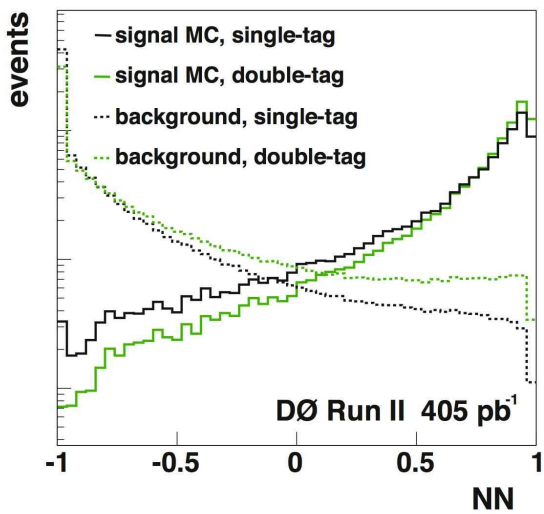

Fig. 16. The neural network (NN) discriminant for $t\bar{t}$ signal and multijet background in single- and double-tag analysis by DØ [108].

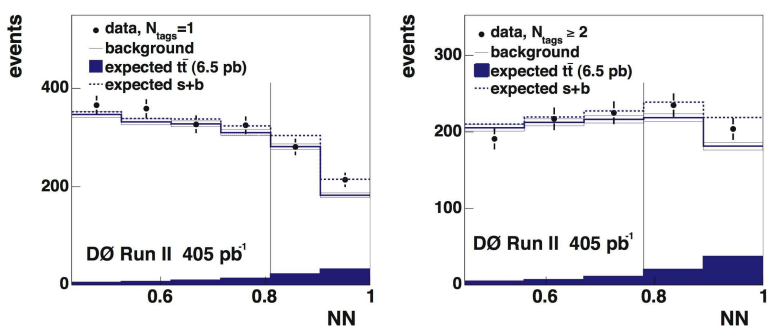

Fig. 17. The distribution of NN output for single- (double)-tag events in the DØ analysis[108]. Shown are the data (points), background (the line histogram), signal (filled histogram) and signal+background (dashed histogram). The vertical line represents the used cut of NN>0.81 (0.78).

After the NN requirement, 495 (439) events are observed while the predicted number of background events is 464±4.6 ($400^{+7.3}_{-6.2}$) in the single (double)-tag analyses. The kinematic selection efficiency times branching ratio for the $t\bar{t}$ signal in the two analyses are $\epsilon_{t\bar{t}} = 0.0242^{+0.0049}_{-0.0058}(0.0254^{+0.0065}_{-0.0070})$, respectively. Based on the clear excess of observed events over the predicted background, DØ has measured a cross-section of $\sigma_{t\bar{t}} = 4.1^{+3.0}_{-3.0}(stat.)^{+1.3}_{-0.9}(sys) \pm 0.3(lum)$ pb for the single-tag analysis and

$\sigma_{t\bar{t}} = 4.7^{+2.6}_{-2.5}(stat.)^{+1.7}_{-1.4}(sys) \pm 0.3(lum)$ pb for the double-tag analysis. A combined cross-section measurement of $\sigma_{t\bar{t}} = 4.5^{+2.0}_{-1.9}(stat.)^{+1.4}_{-1.1}(sys) \pm 0.3(lum)$ pb is obtained for a m_t =175 GeV. The major systematic uncertainty in the analysis arises from the dependence of selection efficiency on the jet calibration and identification.

4.6. *Combined cross section*

The most sensitive of each type of cross section measurement discussed in this section are given in Table 5. For collisions with $\sqrt{s} = 1.8$ TeV, the quoted measurements are final results. Work is still progressing on the $\sqrt{s} = 1.96$ TeV measurements. The input m_t is 175 (178) GeV for many of the DØ (CDF) measurements. Generally, the measured cross section will be higher if m_t is lower because the efficiency to select top decreases somewhat with m_t. For the dilepton and ℓ+jets channels, the slope of measured cross section with difference in mass from the input value ($\Delta\sigma/\Delta m$) is ~ 0.1. The all-jets channels exhibit significantly more variation. The range over which the $\Delta\sigma$ is quoted at least includes $170 - 180$ GeV, and several measurements test from 160 to 190 GeV. Currently, the total uncertainty is reaching the 15% level. This should still be reduced as higher statistics are accumulated. More events will also translate into somewhat lower systematic uncertainties, largely because of the increase in samples dedicated to parametrizing detector performance such as the jet energy scale.

5. Single Top Quark Searches

Twelve years after the discovery of the top quark via strong pair production, the first evidence of electroweak production of single top quarks has been reported by the DØ collaboration[110]. This search is much more challenging than $t\bar{t}$ production due to smaller cross sections and larger backgrounds. A general overview of single top quark production is given in Sec.2.2. Here we discuss the signatures and backgrounds associated with the analyses and review the results by both the CDF and DØ experiments. We review these results with a historical perspective and begin with early single top quark search analyses which resulted in an upper bound on the production cross section (section 5). Later, in section 5.2, we review the analyses which led to the evidence for the single top quark production.

Signal Kinematics Figure 18 shows some of the features of the single top quark events produced in the s- and t-channels. The plots of transverse momentum and the pseudorapidities of objects in the single top quark events shown in this figure reveal that for the t-channel process the b-quark has very low transverse momentum and is peaked at large pseudorapidity (forward region). Thus the b-quark in the t-channel is difficult to detect.

Table 5. Measured cross sections for Tevatron experiments, including the function for different top quark masses. The channel, experiment, collider energy and integrated luminosity are listed in the first four columns. The measured cross section is in column 5. Preliminary results are indicated by * in column 1.

Channel	Expt.	$\sqrt{s}$ (TeV)	Lum. (pb^{-1})	$\sigma_{t\bar{t}}$ (pb)
all-jets/μ−tag [105]	DØ	1.8	110	$7.1 \pm 2.8(stat) \pm 1.5(sys)$
all-jets/b−tag [106]	CDF	1.8	110	$10.1 \pm 1.9(stat)^{+4.1}_{-3.1}(sys)$
$\ell\ell, \ell$+jets, all-jets [74]	DØ	1.8	125	$5.69 \pm 1.21(stat) \pm 1.04$(sys)
$\ell\ell, \ell$+jets, all-jets [91]	CDF	1.8	110	$6.5^{+1.7}_{-1.4}$(stat+sys)
$\ell\ell, \ell$+track [79]	CDF	1.96	197	$7.0^{+2.4}_{-2.1}(stat)^{+1.6}_{-1.1}(sys) \pm 0.6$ (lum)
$\ell\ell, \ell$+track [77]	DØ	1.96	425	$7.4 \pm 1.4(stat) \pm 1.0(sys)$
$\ell\ell$* [82]	CDF	1.96	1200	$6.2 \pm 1.1(stat) \pm 0.7(sys) \pm 0.4(lum)$
ℓ+track* [82]	CDF	1.96	1000	$8.3 \pm 1.3(stat) \pm 0.7(sys) \pm 0.5(lum)$
$\ell\ell, \ell$+track* [78]	DØ	1.96	1000	$6.2^{+0.9}_{-0.8}(stat)^{+0.8}_{-0.7}(sys) \pm 0.4(lum)$
ℓ+jets/topo [86]	CDF	1.96	194	$6.6 \pm 1.1(stat) \pm 1.5(sys)$
ℓ+jets/topo [88]	DØ	1.96	425	$6.4^{+1.3}_{-1.2}(stat) \pm 0.7(sys) \pm 0.4(lum)$
ℓ+jets/topo* [89]	DØ	1.96	900	$6.3^{+0.9}_{-0.8}(stat) \pm 0.7(sys) \pm 0.4(lum)$
ℓ+jets/μ−tag [92]	CDF	1.96	194	$5.3 \pm 3.3(stat)^{+1.3}_{-1.0}(sys)$
ℓ+jets/μ−tag* [93]	CDF	1.96	760	$7.8 \pm 1.7(stat)^{+1.1}_{-1.0}(sys)$
ℓ+jets/μ-tag* [94]	DØ	1.96	425	$7.3^{+2.0}_{-1.8}(stat + sys) \pm 0.4(lum)$
ℓ+jets/b−tag-kin [95]	CDF	1.96	162	$6.0 \pm 1.6(stat.) \pm 1.2(sys)$
ℓ+jets/jprob [102]	CDF	1.96	318	$8.9 \pm 1.0(stat)^{+1.1}_{-1.0}(sys)$
ℓ+jets/b−tag [101]	CDF	1.96	318	$8.7 \pm 0.9(stat)^{+1.1}_{-0.9}(sys)$
ℓ+jets/b-tag [103]	DØ	1.96	426	6.6 ± 0.9(stat + sys) ± 0.4(lum)
ℓ+jets/b−tag* [99]	CDF	1.96	1100	$8.2 \pm 0.5(stat) \pm 0.8(sys) \pm 0.5(lum)$
ℓ+jets/b-tag* [104]	DØ	1.96	900	$8.3^{+0.6}_{-0.5}(stat)^{+0.9}_{-1.0}(sys) \pm 0.5(lum)$
all-jets/b−tag [107]	CDF	1.96	311	$7.5 \pm 2.1(stat)^{+3.3}_{-2.2}(sys)^{+0.5}_{-0.4}(lum)$
all-jets/b−tag [108]	DØ	1.96	405	$4.5^{+2.0}_{-1.9}(stat)^{+1.4}_{-1.1}(sys) \pm 0.3(lum)$

Background processes Associated production of a W boson with jets (W+jets) and pair production of top quarks ($t\bar{t}$) are the two most dominant processes which mimic the single top quark signatures. Events with heavy flavor produced in association with a W boson give rise to irreducible backgrounds. These are $Wb\bar{b}$ and $Wb\bar{b}g$ for the s- and t-channel respectively. In general, the $t\bar{t}$ events have larger jet activity, but they can result in signatures similar to the single top quark in case the jets are merged, mis-reconstructed or are outside the fiducial volume. Leptons can also be lost in the detector cracks or lie outside the fiducial volume considered. $t\bar{t}$ decays can look very similar to single top quark events when one W boson decays to $e\nu$ or $\mu\nu$ and the other decays to $\tau\nu$. Additional multijet background comes from events containing a mis-identified isolated lepton (e or μ) associated with hadronic jets. Z/γ^*+jets contribute to the backgrounds if one of the two leptons from Z decaying to e^+e^- or $\mu^+\mu^-$ is lost. Diboson events (WW, WZ) also contribute to the background, though at a much smaller level.

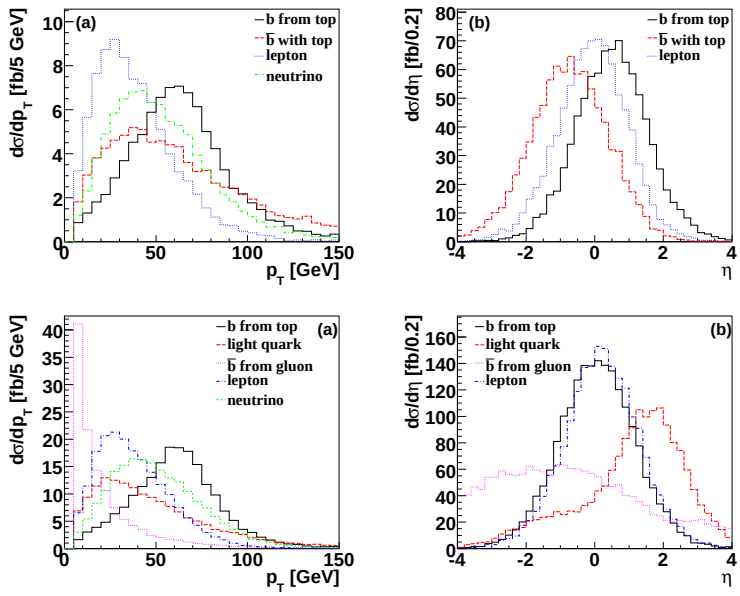

Fig. 18. Distributions of transverse momenta (a) and pseudorapidity (b) for the final state partons in s-channel single top quark events (top row) and for t-channel single top quark events (bottom row). The histograms only include the final state of t, not $\bar{t}$ [111].

Modeling single top quark and backgrounds The two main sources of background are examined: $t\bar{t}$ production and non-top quark backgrounds. The non-top quark backgrounds include W+jets and mis-identified multijet events. W+jets (including heavy flavor process $\bar{q}q' \to Wg$ with $g \to b\bar{b}$ or $g \to c\bar{c}$, and $gq \to Wc$) are included in their relative proportions estimated using ALPGEN[49] and normalized to the data.

Both the CDF and DØ collaborations have performed searches for single top quark production in the data samples gathered in Run I (1992-1996)[112,113]. Data collected during the first few years of RunII have led to updated analyses by CDF and DØ. All of these measurements have led to upper limits on the production cross section of the single top quark as listed in Table 6. These are reviewed below.

Table 6. 95% C.L. upper limit on single top quark production cross section (in pb).

	Theory	Run I		Run II					
		CDF	DØ	CDF			DØ		
				$Q \times \eta$	NN	LD	Cut	NN	LD
Luminosity (pb^{-1})			160	695	955	230	230	230	
s-channel	0.88 (±8%)	< 18	< 17	< 14	< 3.2	$0.1^{+0.7}_{-0.1}$	< 10.6	< 6.4	< 5.0
t-channel	1.98 (±11%)	< 13	< 22	< 10	<3.1	$0.2^{+0.9}_{-0.2}$	< 11.3	< 5.0	< 4.4

5.1. *Search strategy*

In this section we review the searches for the single top quark by the CDF and DØ experiments in Run II. The CDF experiment published a search for the single top quark using a data sample corresponding to an integrated luminosity of 160 pb^{-1}[114] and had provided updated results with 600-955 pb^{-1} of data in the year 2006. The DØ experiment performed a search for the single top quark using 230 pb^{-1} of data[111,115].

The strategy of the analyses pursued during Run II is as follows: First a set of events with the signal topology is selected. Next, they are separated into independent sets based on the flavor of the lepton (e or μ) and the number of b-quark jets (exactly one b-jet or two or more b-jets). The different sets are analyzed independently by statistical techniques to enhance the signal. They are then combined in the final stage. Finally, in the absence of any significant observed signal, binned likelihood fits are performed on the outputs of the statistical analysis methods to obtain limits on the production cross section for single top quarks.

The single top quark search starts with the selection of events with at least one high p_T lepton (electron or muon), significant $\not\!\!E_T$ and between two to four jets. At least one of the jets is $b-$tagged to separate signal events with heavy flavor from the $W+$light jet background event. Separation of samples into s-channel events and t-channel searches is accomplished by requiring at least one untagged jet in the t-channel analysis. For both the channels, selected samples are further subdivided into four orthogonal sets based on the flavor of the lepton (e or μ) and the number of b quark jets: "single tagged" (with exactly one b-tagged jet) or "double tagged" (two or more b-tagged jets) samples. At this initial event selection the background is still expected to be about 90% of the sample.

5.1.1. *Collection of input variables*

To further reduce the backgrounds, both kinematic (object and global event) and topological information is used. Some of the many variables which are used for discriminating against the backgrounds are: jet p_T for different jets; $b-$tag information of the jet; H (total energy); H_T (total transverse energy); M (invariant mass); M_T (transverse mass); summing over various objects in the event; jet-jet separation; jet pseudorapidity (t-channel); top quark spin; etc. They are selected based on extensive analysis of the Feynman diagrams of signals and backgrounds[116]. The list of variables used by DØ analyses is shown in Table 7 (CDF analyses use a subset). The best jet is defined as the jet which together with the W boson leads to an invariant mass closest to the top quark mass of 175 GeV. In the $s-$channel ($t-$channel) analysis, the top quark is reconstructed from the W boson and the 'best jet' (the leading $b-$tagged jet). The W boson is reconstructed from the isolated lepton and the $\not\!\!E_T$. The z-component of the neutrino momentum is calculated by constraining the lepton and neutrino to the W boson mass, and the solution with smaller z-component of the neutrino momentum is chosen from the two possible solutions.

Table 7. List of discriminating variables. A check mark in the final four columns indicates in which signal-background pair of the neural net analysis the variable is used [111].

Variable	Description	Signal-Background Pairs s-channel $Wb\bar{b}$	s-channel $t\bar{t}$	t-channel $Wb\bar{b}$	t-channel $t\bar{t}$
	Individual object kinematics				
$p_T(\text{jet1}_{\text{tagged}})$	Transverse momentum of the leading tagged jet	√	√	√	—
$p_T(\text{jet1}_{\text{untagged}})$	Transverse momentum of the leading untagged jet	—	—	√	√
$p_T(\text{jet2}_{\text{untagged}})$	Transverse momentum of the second untagged jet	—	—	—	√
$p_T(\text{jet1}_{\text{non-best}})$	Transverse momentum of the leading non-best jet	√	√	—	—
$p_T(\text{jet2}_{\text{non-best}})$	Transverse momentum of the second non-best jet	√	√	—	—
	Global event kinematics				
$\sqrt{\hat{s}}$	Invariant mass of all final state objects	√	—	√	√
$p_T(\text{jet1}, \text{jet2})$	Transverse momentum of the two leading jets	√	—	√	—
$M_T(\text{jet1}, \text{jet2})$	Transverse mass of the two leading jets	√	—	—	—
$M(\text{alljets})$	Invariant mass of all jets	√	√	√	√
$H_T(\text{alljets})$	Sum of the transverse energies of all jets	—	—	√	—
$p_T(\text{alljets} - \text{jet1}_{\text{tagged}})$	Transverse momentum of all jets excluding the leading tagged jet	—	√	—	√
$M(\text{alljets} - \text{jet1}_{\text{tagged}})$	Invariant mass of all jets excluding the leading tagged jet	—	—	—	√
$H(\text{alljets} - \text{jet1}_{\text{tagged}})$	Sum of the energies of all jets excluding the leading tagged jet	—	√	—	√
$H_T(\text{alljets} - \text{jet1}_{\text{tagged}})$	Sum of the transverse energies of all jets excluding the leading tagged jet	—	—	—	√
$M(W, \text{jet1}_{\text{tagged}})$	Invariant mass of the reconstructed top quark using the leading tagged jet	√	√	√	√
$M(\text{alljets} - \text{jet}_{\text{best}})$	Invariant mass of all jets excluding the best jet	—	√	—	—
$H(\text{alljets} - \text{jet}_{\text{best}})$	Sum of the energies of all jets excluding the best jet	—	√	—	—
$H_T(\text{alljets} - \text{jet}_{\text{best}})$	Sum of the transverse energies of all jets excluding the best jet	—	√	—	—
$M(W, \text{jet}_{\text{best}})$	Invariant mass of the reconstructed top quark using the best jet	√	—	—	—
	Angular variables				
$\eta(\text{jet1}_{\text{untagged}}) \times Q_\ell$	Pseudorapidity of the leading untagged jet × lepton charge	—	—	√	√
$\Delta\mathcal{R}(\text{jet1}, \text{jet2})$	Angular separation between the leading two jets	√	—	√	—
$\cos(\ell, \text{jet1}_{\text{untagged}})_{\text{top}_{\text{tagged}}}$	Top quark spin correlation in the optimal basis for the t-channel[117], reconstructing the top quark with the leading tagged jet	—	—	√	—
$\cos(\ell, Q_\ell \times z)_{\text{top}_{\text{best}}}$	Top quark spin correlation in the optimal basis for the s-channel[117], reconstructing the top quark with the best jet	√	—	—	—
$\cos(\text{alljets}, \text{jet1}_{\text{tagged}})_{\text{alljets}}$	Cosine of the angle between the leading tagged jet and the alljets system in the alljets rest frame	—	—	√	√
$\cos(\text{alljets}, \text{jet}_{\text{non-best}})_{\text{alljets}}$	Cosine of the angle between the leading non-best jet and the alljets system in the alljets rest frame	—	√	—	—

5.1.2. *Analysis methods*

Several different analysis techniques are employed to separate the signal from the background: Cut based, Neural Networks (NN), Likelihood and Matrix Element based analyses. Generally the analyses are optimized separately for s-channel and

t-channel analyses. For example, the DØ Neural Network analysis focuses on rejecting dominant backgrounds (W+jets and $t\bar{t}$) by training the neural networks or optimizing the cuts separately for each background and for each lepton type. This leads to eight separate sets of cuts or networks (two leptons (e, μ) $\times$ number of tagged b jets ($= 1, \geq 2$) *times* signal type (s, t-channel)).

- **Cut Based analysis:** This is the traditional method of applying simple selection requirements on a set of variables. In the DØ analysis, each of the input variables is assigned a performance metric which is evaluated by computing the best expected limit for a given cut on each of the variables. The variables with the best performance are then combined by a simple AND in order of an assigned rating based on their relative sensitivity. An optimal cut point is also evaluated for each intermediate set of combined variables. Again, the set with the best expected limit is chosen for the final analysis. This optimization is performed for each of the channels separately. For each channel, the optimal sets of variable and cuts are listed in Ref. 111.
- **Template Fit Analysis:** Another technique used by CDF involves a maximum likelihood fit to the distribution of $Q \cdot \eta$, where Q is the lepton charge and η the pseudorapidity eta of the light quark jet of the events, in order to extract the s-and t-channel signal from the data. The variable $Q \cdot \eta$ is chosen as it shows the largest difference in kinematics between s and $t-$channel events (see two left plots of Fig. 19). Templates of $Q \cdot \eta$ distributions from expected s and $t-$channel signals, and the two expected background sources are used for the likelihood fit. To extract inclusive s and $t-$channel content a template fit is carried out using the H_T distribution, as this distribution is similar for both production channels. This is shown in the right plot of Fig. 19. The likelihood fit takes into account the systematic uncertainties from the jet energy scale, the top quark mass, b-tagging efficiencies and the luminosity. Smaller systematic uncertainties from initial state radiation, final state radiation, parton distribution functions, the choice of signal Monte Carlo generator, trigger, identification are also included. Some systematic effects can change the shape of the $Q \cdot \eta$ distribution, which is taken into consideration as well.
  The fit to the $Q \cdot \eta$ distributions using a Bayesian method, leads to a 95% C.L. upper limit on the production cross sections both in the s and $t-$channels independently. The fits using the H_T distribution result in the combined s and $t-$channel upper limits. These limits are listed in Table 6.
- **Neural Network Analysis:** The Neural Network (NN) "MLPFIT"[118] package is used by DØ to analyze (testing and training) the events. The "NeuroBayes" package[119] is used by CDF for their analysis. The networks were used with three layers of nodes: input, hidden, and output. Monte Carlo simulated events are used for the training and testing of the networks. Optimization studies based on the expected upper limits on the

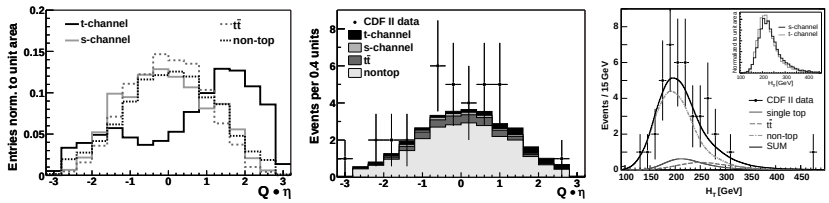

Fig. 19. Distributions of $Q \cdot \eta$ (two left plots) and H_T (right plot) for the CDF single top search [114].

single top quark production cross sections indicate that each of the channels require different networks for treatment of the dominant backgrounds. DØ separates backgrounds into two categories, $Wb\bar{b}$ and $t\bar{t}$ events. CDF has an additional category for $Wc\bar{c}$. This leads to multiple networks (between three to eight depending on the experiment) for the two s-channel or t-channel analyses. As an example, the set of input variables used for the DØ analysis are listed in Table 7 and denoted by a check mark. For each network, the set of input variables could be different (see Table 7) and the selected combination of variables is chosen to give the largest signal to background separation while keeping the testing error at its minimum.
The outputs of the NN for the DØ data and the expected signal and backgrounds are shown in Fig. 20. One notes that the NN output peaks near one for signal events and at low values (near zero) for background events. A good separation between the signal and $t\bar{t}$ backgrounds is seen for the $t\bar{t}$ networks. The $Wb\bar{b}$ networks are not as efficient in distinguishing between signal and backgrounds since the W+jets topology is closer to the signal events than the $t\bar{t}$ events. Similar behavior and separation is found in the CDF analysis as well.

- **<u>Likelihood Discriminant</u>** Another popular technique for extracting small signals from large datasets is by constructing a likelihood discriminant $\mathcal{L}(\vec{x})$ from a vector of measurements $\vec{x}$:

$$\mathcal{L}(\vec{x}) = \frac{P_{signal}(\vec{x})}{P_{signal}(\vec{x}) + P_{background}(\vec{x})} \tag{4}$$

where, $P_{signal}(\vec{x})$ and $P_{background}(\vec{x})$ are the probability density for the signal and background events respectively. The strength of this method relies on the use of the difference in the shapes of the distributions for the signal and background events for a given variable. Both CDF and DØ analyses separate the signal into s-and t-channels while constructing the likelihoods. Monte Carlo events are used to construct the one dimensional probability density functions $P_{signal}(\vec{x})$ and $P_{background}(\vec{x})$ for each of the input variables. The final probability density functions of the signal and backgrounds are the products of the functions constructed for the individual variables.

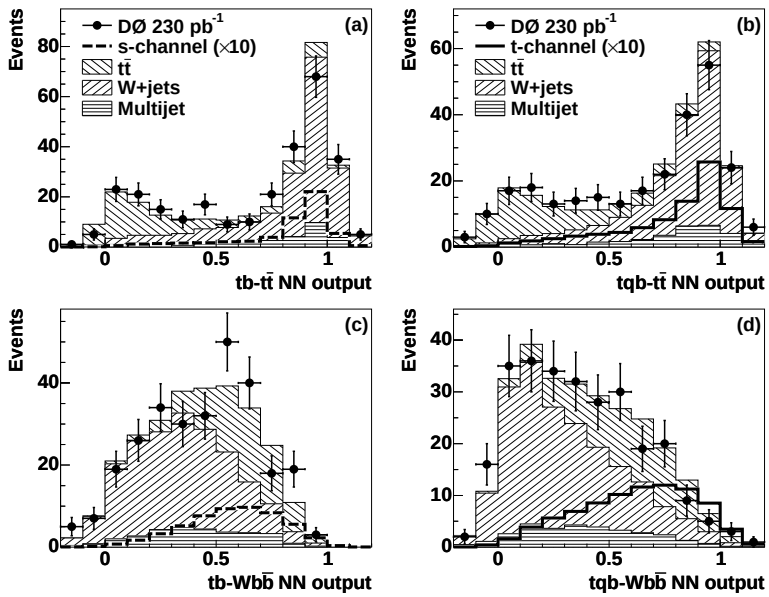

Fig. 20. Comparison of DØ background, signal, and data for the neural network outputs, for the electron and muon channels combined, requiring at least one tag, for the *tb-tt* filter (a), the *tqb-tt* filter (b), the *tb-Wbb* filter (c), and the *tqb-Wbb* filter (d). Signals are multiplied by 10 for readability [115].

No correlations between variables are used. One expects the value of the likelihood discriminant $\mathcal{L}(\vec{x})$ to be peaked near one for signal events and near zero for background events. Many different input variables and combinations were considered during the optimization process to obtain the best expected limit on the cross section measurement. The list of input variables used for the DØ and CDF analysis are similar to those used by NN. The Likelihood Discriminant for the observed single tagged data (electron and muon data combined) together with the expected signal and backgrounds are shown in Fig. 21.

5.1.3. *95% C.L. Upper Limit on production cross section*

The cross section for single top quark production is computed from the observed data using a Bayesian approach. The probability to observe the vector of event yields $\mathbf{d}$ assuming the single top quark production cross section σ is given by the single top quark acceptance α, integrated luminosity $\mathcal{L}$, and the number of events expected from background b, is given by

$$p(\mathbf{d}|\sigma, a, b) = P(\mathbf{d}|a\sigma + b)$$

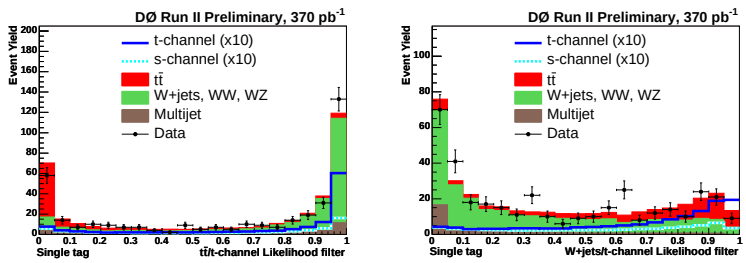

Fig. 21. Data to Monte-Carlo comparison for the $tqb/t\bar{t}$ (left) and $tqb/W+jets$ (right) Likelihood Discriminants for single b-tagged events from the DØ experiment[111].

where $a = \alpha\mathcal{L}$ and $P(x|y)$ is the Poisson probability to observe x event yield when y are expected. Using Bayes' theorem the probability for the single top quark production cross section to have the value σ is then

$$p(\sigma|\mathbf{d}) = \frac{1}{\mathcal{N}} \int\int p(\mathbf{d}|\sigma, a, b)\pi(a, b)\mathrm{d}a\mathrm{d}b,$$

where $\mathcal{N}$ is a normalization constant, a flat prior for σ was assumed and the prior for the other parameters $\pi(a, b)$ is a product of Gaussians with widths given by the experimental uncertainties in these parameters. The dependence on all parameters except σ was eliminated by integrating over these so-called nuisance parameters.

The measured cross section is then given by the value of σ for which $p(\sigma|\mathbf{d})$ is maximized. If this occurs for $\sigma = 0$ an upper limit σ_{max} can be set at confidence level β using the condition

$$\int_0^{\sigma_{max}} p(\sigma|\mathbf{d})\mathrm{d}\sigma = \beta.$$

For a finite cross section the errors δ_+ and δ_- are defined by

$$\int_{\sigma_{max}-\delta_-}^{\sigma_{max}+\delta_+} p(\sigma|\mathbf{d})\mathrm{d}\sigma = 0.6827$$

for which $\delta_- + \delta_+$ is minimized.

Since the observed data are consistent with the background predictions for all analysis techniques used by DØ and CDF, following the prescription for cross section computation described above, the 95% C.L. upper limits on the single top quark production cross sections are computed. These measurements are listed in Table 6. These upper limits represented significant improvements over previously published results[112], mainly due to the larger data sets analyzed, and the use of multivariate analysis techniques. It is interesting to note that they approach the region of sensitivity for models incorporating fourth quark generation scenario or flavor-changing neutral-currents.

5.2. *Evidence for single Top quark production*

The evidence for single top quark production was reported by the DØ Collaboration in December 2006[110]. This analysis is based on a large data sample corresponding to a luminosity of 0.9 fb^{-1} collected between 2002 and 2005. Event sample selection procedures are similar to the earlier searches as described in the previous section. Events are classified into twelve subsamples based on the lepton type (e or μ), the number of jets (two, three or four jets), and the number of tagged b-jets (one or two tags) in the event. The event yields are tabulated in Table 8.

Table 8. Numbers of expected and observed events in 0.9 fb^{-1} for e and μ, one b tag and two b tag channels combined from the DØ experiment. The total background uncertainties are smaller than the component uncertainties added in quadrature because of anticorrelation between the W+jets and multijet backgrounds resulting from the background normalization procedure [110].

Source	2 jets		3 jets		4 jets	
s-channel	16	3	8	2	2	1
t-channel	20	4	12	3	4	1
$t\bar{t}\to\ell\ell$	39	9	32	7	11	3
$t\bar{t}\to\ell$+jets	20	5	103	25	143	33
$Wb\bar{b}$	261	55	120	24	35	7
$Wc\bar{c}$	151	31	85	17	23	5
Wjj	119	25	43	9	12	2
Multijets	95	19	77	15	29	6
Total background	686	41	460	39	253	38
Data	697		455		246	

A multivariate technique known as "Decision Tree"[120] is used for discriminating between signal and background events in the sample. Decision Trees, DT, are a machine learning technique which are used to compute the probability of the event to be a signal event. Decision trees provide a way to represent rules underlying data with hierarchical, sequential structures that recursively partition the data. It is a binary tree with a selection cut implemented at each node such that each event eventually ends up into a well-separated class called "leaves". A purity value defined as the ratio of signal to background events and predetermined from the training samples is associated with each of the leaves. The output of the decision tree is the distribution of the final purity values for the sample and is discrete. A major improvement in this technique, comes from the implementation of the adaptive boosting algorithm AdaBoost[121]. This boosting algorithm modifies the weights of the misclassified events and rebuilds the tree iteratively. The final decision tree with improved performance is an average over many trees produced during the boosting process.

Forty nine variables (see reference [122] for details) are used as inputs to the Decision Tree. These variables based on individual object kinematics, global event kinematics, and angular correlations are constructed in order to discriminate between signal and background events. For each of the three searches $s-$channel, $t-$channel and $s+t$ channel, decision trees were trained on the twelve event subsamples, leading to a total of thirty six decision trees. Thus each one of the 36 decision trees is trained for a given signal signature against the sum of $W+$jets and $t\bar{t}$ backgrounds. The Monte Carlo samples used for training the trees and testing their performance are independent of each other.

Tests on the performance of the decision trees on the collider data are done by studying samples which are rich in background. Two such samples were created: a $W+$jets sample and a $t\bar{t}$ sample. The $W+$jets sample was selected by requiring $H_T < 175$ GeV for the events with two jets and one tagged b-jet. The $t\bar{t}$ sample comprises of events with four jets, one tagged b-jet and $H_T > 300$ GeV. In Fig. 22 (a) and (b), the decision tree discriminants, O_{DT}, are shown for both the background enriched data samples. The prediction of the background models are overlayed on these data distributions. Good agreement is visible between the prediction and the observed events in these background enriched samples.

Output of the decision tree analysis in the high end of the discriminant spectrum for combined e and μ data samples is displayed in Fig. 22 (c). The expected signal and backgrounds are overlaid and summed over the twelve decision trees for $s+t$ channels. A single top quark signal is well accommodated with the data sample. The characteristics of the events in the high decision tree discriminant region have been examined, by making a selection $O_{\mathrm{DT}} > 0.65$. For these selected events, in Fig. 22 (d) the distribution of invariant mass from the best $b-$jet and reconstructed W boson is displayed. Good agreement is observed between the data and a prediction including background and a single top quark signal.

Two other supporting analyses were carried out. One is based on using Bayesian Neural Networks and the other is known as the Matrix Element technique. The Bayesian Neural network[123] at the first stage is similar to a simple Neural Network as described in section 5.1. Instead of choosing one set of weights to characterize the network with Bayesian Neural Networks, a posterior probability density is computed using all possible weights. The final network is obtained by computing a weighted average of a large number of networks, obtained after many sets of training cycles, where the weights are the probability of each network given the training data. The BNN uses a subset of the input variables used in the DT analysis. The training samples are the combined s and t channel Monte Carlo signals and the combined background set. The performance of this technique is shown in Fig. 23 (left panel), for events with electron and two jets, with one of them tagged as a b-jet.

The Matrix Element method encodes all kinematic information of the event and contains all the properties of the interaction. Hence this technique uses maximal information and is firmly anchored with an understanding of the underlying physics

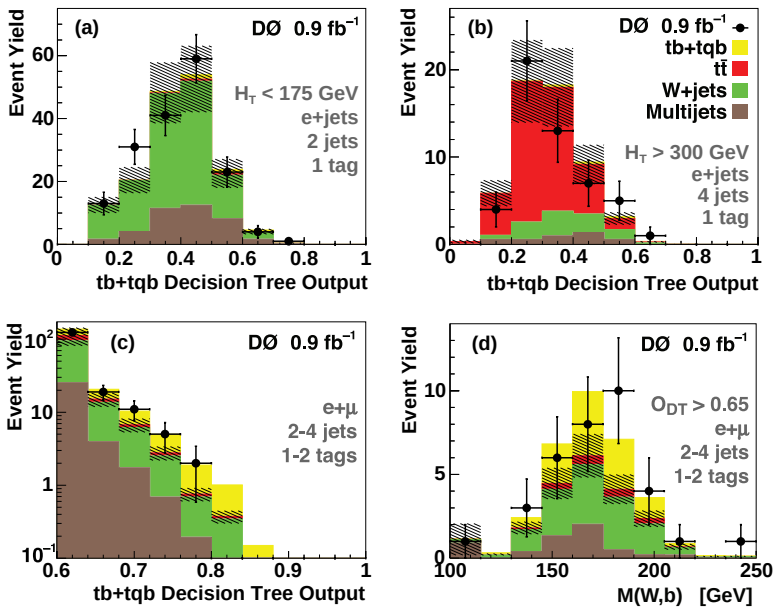

Fig. 22. Boosted decision tree output distributions for (a) a W+jets-dominated control sample, (b) a $t\bar{t}$-dominated control sample, and (c) the high-discriminant region of the sum of all 12 inclusive tb+tqb decision trees. For (a) and (b), $H_T = E_T^{\ell} + \not{E}_T + \sum E_T^{\text{alljets}}$. Plot (d) shows the invariant mass of the reconstructed W boson and highest-p_T b-tagged jet for events with $O_{\text{DT}} > 0.65$. The hashed bands show the ± 1 standard deviation uncertainty on the background. The expected signal is shown using the measured cross section (DØ experiment) [110].

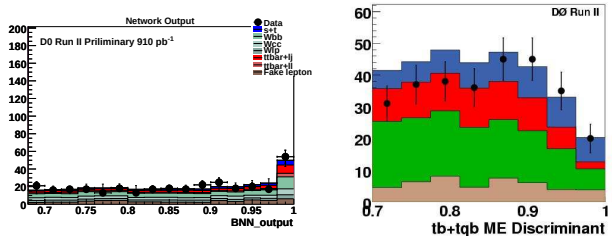

Fig. 23. Bayesian Neural Network discriminant(left) and the Matrix Element discriminant (right), in the high-discriminant region, for the combined event sample (DØ experiment) [122].

processes. Matrix elements of the main signal and background diagrams are used to compute an event probability density for signal and background hypotheses. The signal and background Feynman diagrams used for the subsamples with two jets and three jets are shown in Fig. 24. A discriminant O_{ME} is calculated from the probabilities for the event to be compatible with the signal hypothesis, P_{signal} and

background hypotheses P_{bkg}.

$$O_{\mathrm{ME}} = \frac{P_{signal}}{P_{signal+P_{bkg}}} \tag{5}$$

where P_{signal} is the properly normalized differential cross section ($\frac{\partial\sigma}{\partial\vec{x}}$) for an event which contains objects with reconstructed four-momenta $\vec{x}$:

$$P_{signal} = \frac{1}{\sigma} \times \frac{\partial\sigma}{\partial\vec{x}} \tag{6}$$

This technique is similar to those employed in the top quark mass measurement and shares some of the same tools. Figure 23 (right panel) shows the high end region for O_{ME} obtained from the combined event sample and it accommodates the single top quark signal reasonably well.

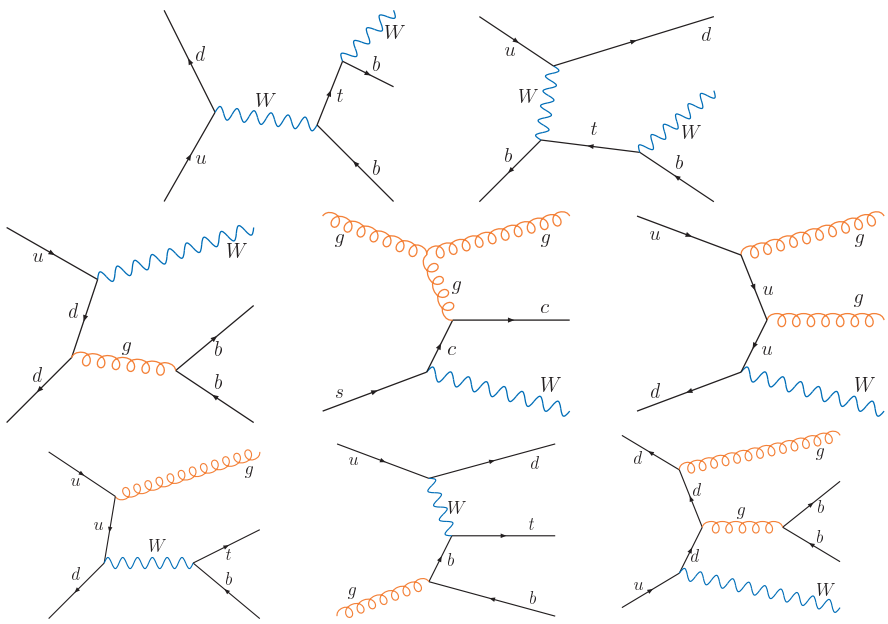

Fig. 24. Representative Feynman diagrams corresponding to the leading-order matrix elements used for event probability calculation. The upper and middle row are for events with exactly two jets. Upper row, signals: $ud \to tb$, $ub \to td$; middle row, backgrounds: $ud \to Wbb$, $sg \to Wcg$, $ud \to Wgg$. The bottom row shows diagrams for events with exactly three jets. Left two plots: signals, $ud \to tbg$, $ug \to tbd$; right plot: background,$ud \to Wbbg$ 122.

A detailed study of the systematic uncertainty was carried out. Dominant sources of systematic uncertainties which are accounted for in the analysis are: normalization of the three major sources of the backgrounds ($t\bar{t}$, $W + jets$ and multijet backgrounds) which includes a component arising from the heavy flavor fraction, the b-tagging rate functions for the signal and backgrounds, the jet energy scale

uncertainty, and the uncertainty on the integrated luminosity. Some of these uncertainties are dependent on the shape of the underlying spectrum. Uncertainties were assigned for each of the backgrounds, as a function of jet multiplicities, lepton type, and number of tags. To derive the affect of each of the uncertainties, the inputs were shifted by $\pm 1\sigma$, and the analysis was redone. Systematic uncertainties on the signal acceptance were also computed in a similar fashion.

Given that an excess of events compared to the background estimates is observed, the cross section is computed using the method described in Sec. 5.1. Before the final cross section results were computed, a verification of the cross section computation procedure was performed by generating many sets of pseudo-experiments or 'ensembles'. These ensembles were subjected to the full analysis chain, including systematic uncertainties.

Generated ensembles include:

(1) Ensembles at a few different values of total $s+t$ channel cross sections.
(2) SM ensemble with inclusive $\sigma(s+t$ channel$) = 2.9$ pb.
(3) Ensembles at the experimentally measured inclusive $s+t$ channel cross section.
(4) zero-signal ensemble

A pool of 1.7 M weighted signal + background events are used to generate the zero signal ensemble. In the ensemble generation process, the relative and total yields of each type of background is fluctuated in proportion to systematic errors. To generate one of the ensembles, a random sample is drawn from a Poisson distribution about the total yield.

All generated ensembles are used to evaluate the linearity of the cross section measurement by comparing the observed cross sections with the input cross sections. The three techniques were tested and display a good agreement with a linear response function.

The SM ensemble is used to estimate the compatibility of the measured value with the SM expectations. The ensemble generated at the measured cross sections were used to verify the estimates of the systematic and statistical uncertainties. The zero-signal ensemble is used to determine the sensitivity of each measurement. The expected $p-$value is defined as the fraction of zero-signal ensembles in which a SM cross section of at least 2.9 pb is measured. The observed $p-$value is computed as a fraction of zero-signal pseudo-datasets in which at least the observed cross section is measured.

Final results of the measured cross sections and the significance are given in Table 9 for the primary DT analysis, together with the two supporting analyses: BNN and ME.

Figure 25 shows the first measurements of the single top quark cross sections at the Tevatron. The plots are from the DT analyses.

The measured cross section for single top quark production $\sigma(p\overline{p}\rightarrow s + t -$ channel$) = 4.9 \pm 1.4$ pb, which is consistent with expectations from SM. The observed $p-$value, or the probability that the background fluctuates to give the

Table 9. Results from the different analysis techniques for measurement of the cross sections and significance of the analyses from the DØ experiment. SD below denotes the number of standard deviations. [110].

	DT	ME	BNN
$\sigma(p\overline{p}\rightarrow s+t-\text{channel})$	4.9 ± 1.4 pb	$4.6^{+1.8}_{-1.5}$ pb	5.0 ± 1.9 pb
expected p-value	1.9%	3.7%	9.7%
observed p-value	0.035%	0.21%	0.81%
observed significance	3.4 SD	2.9 SD	2.4 SD

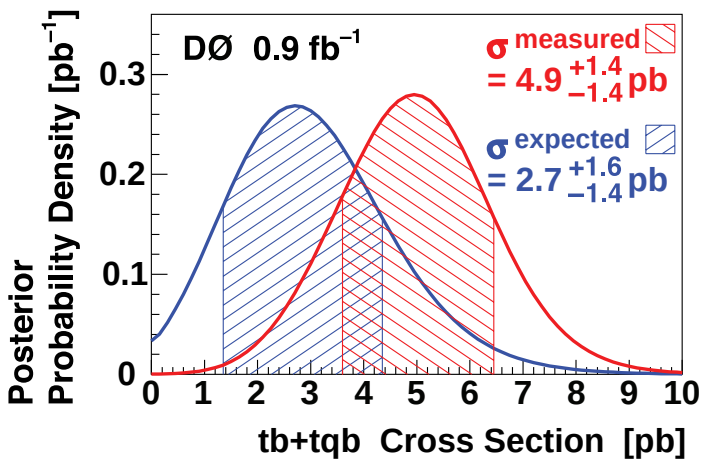

Fig. 25. Expected SM and measured Bayesian posterior probability densities for the *tb*+*tqb* cross section. The shaded regions indicate one standard deviation above and below the peak positions (reproduced from Ref. 110).

measured cross section value of 4.9 pb or greater is 0.035%, which corresponds to a 3.4σ evidence for the single top quark production at the Tevatron.

The CDF collaboration confirmed the DØ evidence for single top quark production in August 2007 by analyzing a data sample corresponding to an integrated luminosity of 1.5 fb^{-1}. CDF performed analyses using two different techniques: a multivariate likelihood technique and the matrix element discriminant technique[124]. These are extensions of the techniques already described earlier and applied to smaller datasets. The single top production cross section measured by the matrix element technique is $\sigma(p\overline{p}\rightarrow s+t-\text{channel}) = 3.0^{+1.2}_{-1.4}$ pb,which is consistent with expectations from SM and those measured by the DØ experiment. This result corresponds to a 3.1σ excess over SM background. The likelihood discriminant exhibits a 2.7σ excess over SM backgrounds and leads to a compatible single top quark production cross section measurement.

6. Measurements of the Top Quark Mass

6.1. *Role in electroweak model*

Mass of the fundamental particles is currently understood to be generated from the spontaneous breaking of electroweak symmetry via the Higgs mechanism. The high value of the top quark mass[125] provides a means to establish the Higgs mass scale because the two can be related via radiative corrections to the W mass, M_W. One loop corrections to M_W give $M_W^2 = \frac{\pi\alpha/\sqrt{2}G_F}{sin^2\theta_W(1-\Delta r)}$ where Δr includes a correction depending on m_t ($\frac{3G_F m_t^2}{8\sqrt{2}\pi^2 tan^2\theta_w}$) and on the Higgs mass ($\frac{11G_F M_Z^2 \cos^2\theta_W}{24\sqrt{2}\pi^2} \ln \frac{M_H^2}{M_Z^2}$).

The fact that m_t is 35 times higher than the next heaviest fundamental fermion gives it a place of importance for another reason. Given the Higgs vacuum expectation value, $v \sim 247$ GeV, the current world average m_t points to a top quark Yukawa coupling of $Y_t = \frac{m_t\sqrt{2}}{v} \sim 1$. Since the electroweak theory makes no prediction of these couplings and they range over many orders of magnitude, it seems surprising that one of them would be unity. This value raises interesting questions about the precise nature of the Higgs mechanism, and some believe that the measured value of m_t may indicate extra Higgs doublets, as in Minimal Supersymmetric Models (MSSM)[126]. For these reasons, the measurement of the top quark mass has rapidly become one of the most important efforts in the whole top quark sector. It is in fact one of the key parameters to come out of the current Tevatron program.

6.2. *General techniques for mass extraction*

The top quark mass can be extracted from each of the broad channels in the $t\bar{t}$ final state: dileptons, ℓ+jets and all-jets. Across these channels, there are three very general approaches to experimental measurement of m_t. In order of increasingly sophisticated usage of the information in each event, they are:

- **Fitting Kinematic and Decay Parameters:** The value of m_t is reflected in several individual observables of top quark events. For instance, the direct $t \to b$ decay means that in the top quark rest frame, the $b-$quark has momentum $\sim m_t/2$. In the lab frame, the motion of the top quark and jet specific effects reduce the strength of this correlation. However, the observed p_T spectrum of b-jets is still anticipated to strongly follow m_t. In addition, the decay length distribution associated with b-jets also correlates with m_t. By fitting one or more of these parameters one can discriminate between top quarks of different masses. Such a fit in a sample of data can be performed to pull out a measurement of m_t.
- **Kinematic Reconstruction:** $t\bar{t}$ final states leave as many as 18 kinematic observables (17 for ℓ+jets, 14 for dilepton). Because of the specific decay chain from $t\bar{t}$, there are correlations among the kinematics of these objects. For instance, two light-quark jets from a W boson should be consistent with a dijet mass $\sim M_W$. Constraint equations describe these relations and can be used to calculate solutions that provide a mass estimator for each candidate event. By

fitting these mass estimators for a set of events, the mass of the top quark is extracted.

- **Matrix Element Fitting:** A special case of kinematic recontruction involves the full use of the information about top quark production and decay. By using the leading-order matrix elements, in conjunction with a full knowledge of the experimental resolutions of the final state object momenta, a fit can be performed to the data. This is used to provide a probability that an observed event configuration is consistent with a top quark of a certain mass.

Almost all analyses are based on the latter two strategies. These approaches generally yield substantially better uncertainty than the first because they use many, if not all, of the measurements made for each event. The matrix element approach in particular tends to extract the maximum information and so has slightly better performance. Because each method relies on different information from the complex $t\bar{t}$ event, both CDF and DØ pursue multiple strategies for each class of final state. By ascertaining the correlations between these approaches, they provide the best overall estimate of the top quark mass.

All analyses that measure the top quark mass generate pseudo-experiments to test the performance and calibration of their methods and to determine the effects of systematic uncertainties. For these tests, simulated event samples (*ensembles*) are generated that correspond to the observed event sample in number of events and signal and background composition. These ensembles are then processed in the same way as the collider data. In this way the experiment at hand can be simulated many times. The mean $\langle m \rangle = \sum_{i=1}^{N} m_i/N$ of the measured top quark masses m_i from N ensembles, their rms $\sigma(m) = \sum_{i=1}^{N} \sqrt{(\langle m \rangle - m_i)^2/N}$, and the mean and rms of their pulls $d = (m_i - m_t)/\delta m_i$ can be determined. Here m_t is the top quark mass assumed in the simulation and δm_i is the statistical uncertainty in the measurement from the ith ensemble. A well calibrated analysis method gives $\langle m \rangle = m_t$, $\langle d \rangle = 0$, and $\sigma(d) = 1$. Ensemble tests can be used to calibrate the methods, i.e., determine corrections to be applied to the measurements so that these relations are satisfied. Various sources of systematic uncertainties on the mass measurement are considered. Some of the most prominent sources which are carefully evaluated are: 1) jet energy scale, 2) initial state gluon radiation, 3) final state gluon radiation, 4) parton distribution functions, 5) Monte Carlo generators, 6) background model, 7) b-tagging, 8) Monte Carlo statistics.

6.3. *The dilepton final state*

It is important to study m_t in all of the final states in which the top quark can be identified for two main reasons. Non-standard decays can impact specific final states differently. The kinematic analysis involved in a mass measurement therefore provides an additional test of the hypothesis that the signal events conform to the $t \to Wb$ decay chain. If this chain is other than expected, sufficient statistical precision would reveal discrepancies between the measured m_t as estimated in different

channels. Dilepton channels provide both an independent statistical sample with which to measure m_t. As the integrated luminosity at the Tevatron increases or the LHC turns on, the statistical limitations of this channel become less relevant. Systematic uncertainties are similar in magnitude to those for the single lepton channels, and so the dilepton-based measurement has an important role in improving the world-average top quark mass.

6.3.1. *Fitting with kinematic parameters*

The effort to extract a measure of m_t in dilepton events has involved each of the techniques mentioned in Section 6.2. The most basic of these involves fitting to kinematic distributions in candidate events. Because the top quark is so much more massive than any of the fundamental fermions in its decay chain, the magnitude of m_t is directly manifested in the momenta of these particles. For instance, the transverse momenta of the b-quarks are of order $m_t/2$.

This approach has been tried by CDF using eight events in their explicit dilepton sample. Two different approaches were combined. If one ignores b-quark and lepton masses, then the top quark mass can be expressed approximately as $m_t^2 = M_W^2 + \frac{2(M_{lb}^2)}{1-\cos\theta_{lb}}$. One can rewrite this expression in terms of well-measured quantities,

$$m_t^2 = \left\langle M_{lb}^2 \right\rangle + \sqrt{M_W^4 + 4M_W^2 \left\langle M_{lb}^2 \right\rangle + \left\langle M_{lb}^2 \right\rangle^2} \tag{7}$$

Here the b refers to the jets which are presumed to arise from the b-quarks. There is some confusion arising from the combinatorics of mapping the jets and leptons that should come from the same top quark. Considering the allowed jet-lepton configurations, each event produces two M_{lb} measurements. These values are used to provide a value for $\left\langle M_{lb}^2 \right\rangle$ for the sample using a prescription tuned with $t\bar{t}$ events generated with Herwig. A top mass measurement is extracted from this parameter in the data sample[127]. This is augmented with another approach which uses the average p_T of the two $b-$jets in the event. This average is very correlated with $m_t/2$. A maximum likelihood fit is applied to templates generated from this parameter for signal and background samples. A combined mass estimate of $161 \pm 17(stat) \pm 10(sys)$ GeV was obtained from these analyses[127].

6.3.2. *Fitting using kinematic reconstruction*

While the technique of fitting to kinematic parameters provides useful, general estimates of m_t, it does not use all of the information in an observed event that might maximize the measurement's precision. For instance, momentum correlations between final state particles which can be used to test whether the event is consistent with two top quarks of equal mass, or two W bosons with mass equal to M_W. These capabilities are gained with an explicit kinematic reconstruction of an event. Performing such a reconstruction with dilepton events has the challenge that there are

two neutrinos. There are 18 unknowns for the six initial fermion three-momenta, but only four full three-momenta measured plus two components for the $\not\!\!E_T$. Three additional constraints arise from requiring each $l\nu$ pair to give M_W, and both top quarks must have equal mass. As a result, a -1C underconstrained fit results and some information must generally be provided as input to solve these events. Generally, approaches assume an input value of m_t in steps over the allowed range (e.g. 150 GeV to 200 GeV).

The specifics of how the events are solved varies with method (see below). A two-fold ambiguity results for the solutions for the momentum of each neutrino. This ambiguity in kinematic reconstruction is compounded by the different assignments of lepton and jet to one of the $t \to Wb$ decay chains. A particular $configuration$ refers to a particular jet assignment in tandem with one of the neutrino solutions given that assignment. Generally, a $weight$ is calculated for each configuration which reflects the relative consistency of that configuration with some additional observed property in the event. This weight is summed for all configurations which are solved for a particular input m_t.

This integration is performed for a range of assumed top quark masses to provide a probability or 'weight' vs. m_t for each event. Several parameters of the weight distribution carry information about the actual m_t. These 'mass estimator' parameters are used to compare events in data with expectations from top quark signal events of different masses, and background. Often, analyses will choose just the mass for which the weight distribution is maximum ('peak') as the mass estimator. The peak does indeed carry most of the sensitivity to the actual m_t for the two kinematic reconstruction strategies described below. However, more information is available in the rest of the weight distribution. Other approaches extract this information by forming a coarsely binned template from the weight distribution, or taking instead the first couple moments of this distribution. In any of these cases, the distribution of mass estimators is generated for data, and this must be compared via maximum likelihood fit to templates of distributions for signal and background samples.

6.3.3. *Neutrino weighting*

One method for solving $t\bar{t}$ events utilizes the expected neutrino rapidity distributions. This method is termed 'neutrino weighting' (νWT) and was first developed by DØ in Run I[128]. A kinematic fit is performed by omitting two measured variables, $\not\!\!E_x$ and $\not\!\!E_y$. To compensate for this loss of information, one assumes rapidities for the two neutrinos. An integration over the neutrino rapidity distributions is performed such that for each choice of neutrino rapidity pair and jet combination, the neutrino momentum solutions are calculated. For each configuration, a weight is calculated by comparing the measured event $\not\!\!E_T$ with the kinematically reconstructed $\not\!\!E_T$

$$w = \sum \exp\left(\frac{-(E_x^{calc} - E_x^{obs})^2}{2\sigma_{E_x}^2}\right) \exp\left(\frac{-(E_y^{calc} - E_y^{obs})^2}{2\sigma_{E_y}^2}\right) \tag{8}$$

This weight is summed for all configurations for each value of m_t. Templates using the parameters from the full integrated weight vs. m_t distribution can be used to extract a top quark mass.

DØ has performed this analysis with Run I[128] and Run II[135] data by coarsely binning the weight distribution. The Run II analysis differs primarily in that the ℓ+track channels were included. A maximum likelihood fit of these templates is performed to analogous templates for simulated signal and background, and instrumental backgrounds from data. A probability density estimator approach is taken [139]. The signal probability for a given m_t, $f_s(\vec{W}|m_t)$, and background probability, $f_b(\vec{W})$ are established by comparison of data templates ($\vec{W}$) with those for signal and background. The value of m_t can be extracted by maximizing the likelihood

$$L(m_t, \bar{n}_b, n) = G(n_b - \bar{n}_b, \sigma)P(n_s + n_b, n) \times \Pi_{i=1}^{n}[(n_s f_s + n_b f_b)/(n_s + n_b)] \quad (9)$$

where a Gaussian and Poisson constraint are placed on the estimate of n_b and $n_s + n_b$ given the observed event yield, respectively. As is typically done with these analyses, the method is tested by performing the analysis on independent pseudo-experiments of simulated signal and background events. In common with most of the mass analyses, the relation of average fitted top quark mass vs. input m_t was verified in each channel to have slope near unity and with small offset. This helps to keep systematic uncertainties from the method to a minimum. Any residual difference of the slope and offset from unity and zero, respectively, is used to correct the fitted mass. The statistical uncertainty from a given ensemble is extracted from limits in m_t when $-ln(L)$ varies by 0.5 from its minimum value. It is cross-checked by verifying that pull widths are near 1.0. Statistical uncertainties for the Run II analysis were corrected for a small deviation of pull widths from unity. The plot of the $-ln(L)$ vs. m_t resulting from the maximum likelihood fit to the Run II data is given in Fig. 27. The top mass was measured to be $m_t = 179.5 \pm 7.4(stat)$ GeV. A 5.6 GeV systematic uncertainty is dominated by the jet energy scale. This measurement was combined with the matrix-weighting determination (see Section 6.3.4) to yield $m_t = 178.1 \pm 6.7(stat) \pm 4.8(sys)$ GeV[135]. The Run I measurement was $m_t = 170.0 \pm 14.8(stat)$ GeV [128].

The dilepton analysis with νWT has been pursued in preliminary analyses in the 1 fb^{-1} data sample [137,136]. One question for these analyses has been what is the most optimal way to use the output of the weight calculation (i.e. the weight distribution) to get the smallest expected uncertainty in the top mass. Ref. 137 presents an analysis in $e\mu$ events of three different approaches to extract the value of m_t from the weight distribution. These analyses attempted to determine an optimal use of the most important parts of a weight distribution. One of these three methods constituted an optimized version of the binned template approach described above. Another approach used just the value of the top mass for which the weight was maximized, and then performed a 2-dimensional fit to this peak value and the input m_t. A third approach considered various properties of the weight distribution (e.g. moments, integral weight in high and low mass bins, etc.) and settled on

the first two moments as the minimal number of parameters that provided the 20% improvement in sensitivity usually associated with the use of the full binned template. The 2-dimensional fit and moments approaches each were found to match the *apriori* expected sensitivity of the binned-template method, and were combined into a measurement using dilepton events $(ee, e\mu, \mu\mu)$ in 1 fb^{-1} [136]. A value of $m_t = 172.5 \pm 5.8(stat) \pm 3.5(sys)$ GeV was obtained.

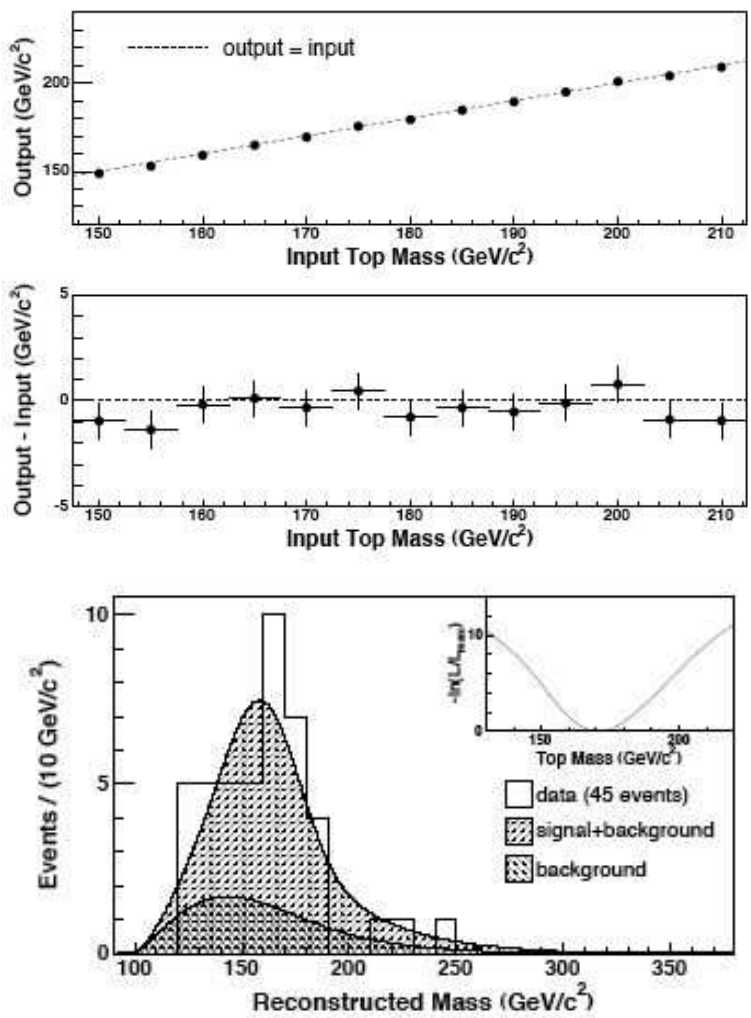

Fig. 26. νWT results from the 359 pb^{-1} CDF Run II ℓ+track sample. The linearity of the fit (left) and data overlaid with signal and background templates (right) are shown[130].

CDF has pursued the νWT approach in 359 pb^{-1} of data in Run II. The basic

kinematic reconstruction is performed similarly to that used by DØ . In Run II, they applied the technique to their ℓ+track sample of 46 events. CDF chose the mass estimator as the peak of the weight distribution. Thus the data m_{peak} distribution is compared to the expectation from signal and background (see Fig. 26). The maximum likelihood fit on data gives $m_t = 170.7^{+6.9}_{-6.5}(stat) \pm 4.6(sys)$ GeV[130]. Systematic uncertainties were estimated for jet energy scale, gluon radiation (ISR and FSR), background template shape, *pdf*s, and showering Monte Carlo generator. A further improvement for CDF is obtained by combining this analysis with two others of lesser statistical power. These use an assumption of the longitudinal momentum of the top quarks, or the azimuthal angle of the neutrinos, to solve each candidate event. The final result from this combination is $m_t = 170.1 \pm 6.0(stat) \pm 4.1(sys)$ GeV[140]. In Run I, which used an explicit dilepton selection, the mass estimator for each event was taken as the weighted mean in a window around the mass with highest weight. This approach generated a value of $m_t = 167.4 \pm 10.3(stat) \pm 4.8(sys)$ GeV[129]. CDF performed a consistency check with the fitting procedure garnered in single lepton double-tagged events by treating the two light-quark jets from the W has a lepton and a neutrino. By mimicing the dilepton signature in this way they obtain a mass estimate in these events which was within the expected resolution.

6.3.4. *Matrix weighting*

Another approach to kinematic reconstruction of top quark events has been proposed [131,132]. In this method, the measured $\not\!\!E_T$ is not omitted from the kinematic reconstruction, thereby permitting a $t\bar{t}$ event to be solved to an eightfold ambiguity if m_t is assumed. Unlike the νWT approach, both the t and $\bar{t}$ are solved simultaneously. A weight is calculated for each solved configuration with an assumed mass, m_t:

$$w = f(x)f(\overline{x})P(E_{l1}|m_t)P(E_{l2}|m_t) \tag{10}$$

where $f(x)$ is the *pdf* taken at the Feynman x obtained for the solution. The $P(E_l^*|m_t)$ are the probabilities for a lepton to have energy E_l in the solved top quark rest frame. This approach is termed 'matrix weighting' (MWT).

The DØ Collaboration has pursued this approach in both Run I and Run II. Using the 370 pb^{-1} data sample from Run II, they considered the explicit dilepton channel [135]. The candidate sample was broken down into the low background b-tagged subsample, and the higher background sample with strictly topological selection. This topological selection loosens kinematic and electron identification requirements on the $e\mu$ channel relative to what was done for the νWT analysis described above. This separation by $b-$tagging was done to enhance the sensitivity to the signal events in data. The maximum likelihood is performed by taking the peak of the weight distribution:

$$L(m_t) = \Pi_{i=1}^{n_{bin}}((n_s s_i(m_t) + n_b b_i)/(n_s + n_b))^{n_i} \tag{11}$$

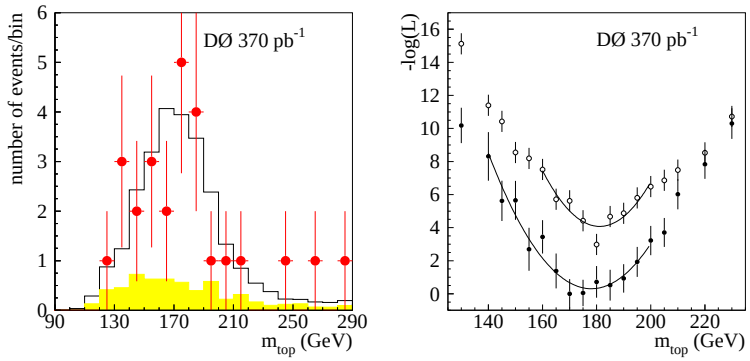

Fig. 27. The m_{peak} distribution from the MWT technique applied to 370 pb^{-1} of dilepton events from DØ (left). The νWT (open circles) and MWT (closed circles) fits are shown (right) for the data. The former also includes the ℓ+track channel[135].

where the product is taken over the i bins of the m_{peak} distribution from data (n_i) as compared to a signal template (s_i) and a background template (b_i). This constitutes a different approach than used for Run I since there are single templates from the m_{peak} distributions of the data, signal and background rather than templates from full weight distributions for each event in data, signal and background samples. From 26 dilepton events, a value of $m_t = 176.2 \pm 9.2(stat) \pm 3.9(sys)$ GeV was determined. The plot of the $-ln(L)$ vs. m_t is given in Fig. 27. For comparison, the Run I measurement was $m_t = 168.2 \pm 12.4(stat)$ GeV[128]. For the Run II measurement, the dominant systematic uncertainty was from the uncertainty in jet energy calibration. The matrix-weighting approach has been applied to the 1 fb^{-1} sample in dilepton events and yielded $m_t = 175.2 \pm 6.1(stat) \pm 3.4(sys)$ GeV [138].

6.3.5. *Matrix element fit*

Use of the full matrix-element to encompass the expected correlations of particle kinematics in a mass analysis was first applied by DØ in complete form with single lepton events[134]. The CDF collaboration has performed such an analysis with dilepton events[133]. The analysis uses the explicit dilepton event selection from the cross section measurement described above. This gives 33 events in 340 pb^{-1}.

This analysis differs from those described above which integrate over just one class of parameters to perform the fit, such as neutrino rapidity or Feynman x. Instead the leading order matrix element for $q\bar{q} \to t\bar{t}$ production is used. Some initial assumptions are implemented which permit a more tractable calculation. Lepton momenta are assumed to be perfectly measured. Quark directions are assumed to be perfectly indicated by observed jet angles. An integration is then performed over the neutrino and quark energies as calculated from the LO matrix element. This integration is constrained by a *transfer function* which expresses the mapping of quark energies to observed jet energies obtained from a sample created with HERWIG

fed into GEANT. The probability density can then be expressed as

$$P_s(x|m_t) = \frac{1}{\sigma(m_t)} \int d\Phi \, |\mathcal{M}_{tt}(q_i, p_i; m_t)|^2 \times \prod_{jets} W(p_i, j_i) f_{PDF}(q_1) f_{PDF}(q_2) \quad (12)$$

where the matrix element is performed as in Ref. [142]. When performing this integration, the contribution from the leading order gluon-gluon production is omitted. A similar probability density calculation is performed for those background processes arising from Z and WW production, as well as W + jets in which one jet fakes a lepton. One can then obtain a joint likelihood for an event sample by multiplying the likelihoods for each event from the background and signal probability densities.

In order to test the validity of the result, ensembles are constructed from simulated signal and background samples which were allowed to fluctuate with Poisson fluctuations. The instrumental background was obtained from data. The resulting slope vs. input (pole) m_t, shown in Fig. 28, is not unity primarily because of the simplification of the background components in the probability density calculation. The measured top quark mass and estimated statistical uncertainty are corrected for this slope. Additionally, the resulting pulls are 1.51, so the statistical uncertainty is corrected for this. The resulting top mass measurement in data is $m_t = 165.2 \pm 6.1(stat)$ GeV[133]. Figure. 28 shows the probability density vs. m_t, as well as the $-ln(L)$ vs. m_t (inset). Systematic uncertainties are estimated for several sources. The chief one is the jet energy scale (2.6 GeV) which is obtained by varying this calibration within its allowed range. The effect of uncertainties in *pdf*s is quantified in several ways, for instance comparing CTEQ5L and MRST72, and by exploring the range given in the CTEQ6M set of functions. Combining all sources gives a 1.0 GeV *pdf* uncertainty. Initial and final state radiation are varied giving a 0.5 GeV and 0.7 GeV uncertainty, respectively. Pythia and Herwig generated events are used to provide a Monte Carlo generator uncertainty (0.8 GeV). Other uncertainties are calculated for background modeling and the fitted mass slope correction. The total uncertainty tallies to 3.4 GeV. When combined with the template-based methods, the value of m_t was determined to be $167.9 \pm 5.2(stat) \pm 3.7(sys)$ GeV. The matrix element method was also applied in 1.03 fb^{-1} of data and yielded $164.5 \pm 3.9(stat) \pm 3.9(sys)$ GeV [141].

6.4. *Single lepton channels*

ℓ+jets events the top quark mass is reconstructed from the momenta of the charged lepton (e or μ), the transverse momentum of the neutrino which is inferred from the $\not{E}_T$ in the event and the momenta of the four jets in the detector, two from the fragmentation of the b quarks and two from the hadronic W decay. There are two unknown parameters in the kinematic description of lepton+jets events: $\not{p}_z$ and m_t. On the other hand the event kinematics have to satisfy four constraints. The charged lepton and neutrino momenta must add up to a system whose mass equals the mass of the W boson. Adding the momentum of the b-jet from the semi-leptonic

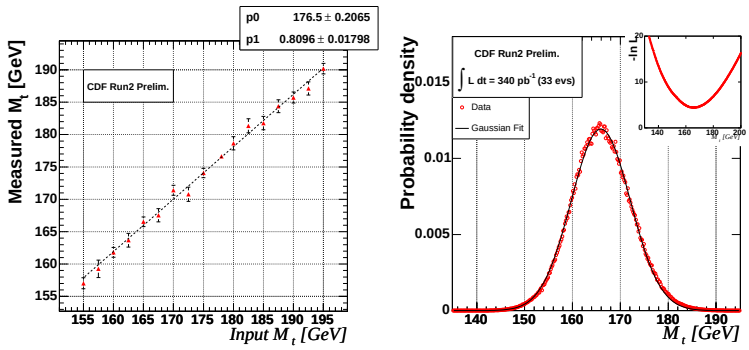

Fig. 28. CDF matrix element results in 340 pb^{-1} dilepton events. The scale between fitted and input top mass is shown (left) and the probability density as a function of m_t is shown at right[133].

top quark decay must give a system with the mass of the top quark. The invariant mass of the di-jet system from the hadronic W decay must equal the W boson mass and the three-jet system from the hadronic top quark decay must have the mass of the top quark. We can thus perform a 2-C kinematic fit of the ℓ+jets decay hypothesis to these events to determine the most likely value of the top quark mass. This simple picture is complicated by the presence of jets from gluons radiated from the initial state and by the splitting of jets from the top quark decay. Moreover it is not possible to uniquely assign the jets in the event to the partons from $t\bar{t}$ decay. If only the four jets with the largest transverse momentum values are considered, there are 12 different ways to assign jets to partons. If one jet is identified as originating from the fragmentation of a b-quark and is only assigned one of the b-quarks this reduces to eight permutations. If two jets are identified as b-jets, this further reduces to two permutations.

The experiments have applied several techniques to extract the top quark mass from ℓ+jets events. Almost all are based on the kinematic reconstruction of the top quark mass. An exception is a measurement by the CDF collaboration that used the decay length distribution of $b-$jets to determine the top quark mass. The simplest kinematic reconstruction technique is the template method which has been used by CDF and DØ. The matrix element method and the ideogram method were both developed at DØ and are now used by both experiments. We will describe these methods in the following sections.

The kinematic reconstruction of the top quark mass requires that all energy and momentum measurements are well calibrated. The electron energy scale and the muon momentum scale can be calibrated precisely enough with $Z \to \ell^+\ell^-$ decays that the residual uncertainty is negligible. The calibration of the jet energy scale, however, is more difficult and gives rise to the dominant systematic uncertainty in the top quark mass measurement. In addition to the *apriori* calibration of the jet

energy scale, most recent measurements of the top quark mass in the ℓ+jets channel also make use of the hadronic W boson decays in these events to gain an additional constraint on the jet energy scale. These analyses use the known W mass as an input parameter and then determine simultaneously the top quark mass m_t and an overall jet energy scale parameter α_{jes} that multiplies all jet energies.

6.4.1. *Template method*

For the template method one chooses an estimator for the top quark mass, typically the best fit mass m_{fit} from a kinematic fit of the event. A simulation is used to compute the expected distribution of this estimator based on the expected number of signal and background events as a function of the top quark mass. These distributions are referred to as templates. One then performs a fit of the templates to the distribution of the estimator observed in the data to determine the value of the top quark mass that best predicts the data distribution.

The early measurements of the top quark mass by CDF and DØ in 1995[1,2] used this method. DØ has used this method for its first top quark mass measurement from Run II using of approximately 230 pb^{-1} of data[143]. CDF also performed a measurement of the top quark mass using this method on 318 pb^{-1} of data from Run II[144].

The CDF analysis divides the sample of events with a high-p_T electron or muon, $\not\!\!E_T$ and at least four high-p_T jets into four subsamples of different combinatorics and background contamination levels defined by the number of b-tagged jets: at least two b-tagged jets, at least one 'tight' b-tagged jet, at least one 'loose' b-tagged jet, and no b-tagged jets. For every event with $\chi^2 < 9$ for the kinematic fit the hypothesized top quark mass m_{fit} that minimizes χ^2 is entered into a histogram. The masses of all pairs of jets that are not tagged as b-jets are entered in another histogram. Both quantities are histogrammed separately for the four subsamples.

The templates are histograms of m_{fit} and m_{jj} from Monte Carlo simulations, parameterized in terms of the hypothesized top quark mass m_t and the jet energy scale parameters α_{jes} and separately for each of the subsamples. Sample templates are shown in Fig. 29.

A simultaneous fit of the data to the parameterized templates gives best agreement for $m_t = 173.5^{+3.7}_{-3.6}(\text{stat} \oplus \text{jes}) \pm 1.3(\text{sys})$ GeV. The *apriori* calibration of the jet energy scale $\alpha_0 \pm \delta\alpha$ enters into this fit as a Gaussian constraint on $\Delta\alpha = 0 \pm 1$, where $\Delta\alpha = (\alpha_0 - \alpha_{jes})/\delta\alpha$. Best agreement is achieved for $\Delta\alpha = -0.10^{+0.78}_{-0.8}$. Figure 30 shows a contour plot of the likelihood in the $m_t - \Delta\alpha$ plane.

An identical analysis is carried out on a factor of two larger data sample corresponding to a luminosity of 680 pb^{-1} [145], leading to a measurement of $m_t = 173.4 \pm 2.5(\text{stat} \oplus \text{jes}) \pm 1.3(\text{sys})$ GeV.

A variation of this analysis which uses a 2-dimensional templates of top quark mass and hadronic W boson mass constructed using a Kernel Density Estimate (KDE) has been carried out by the CDF collaboration. With this technique and a

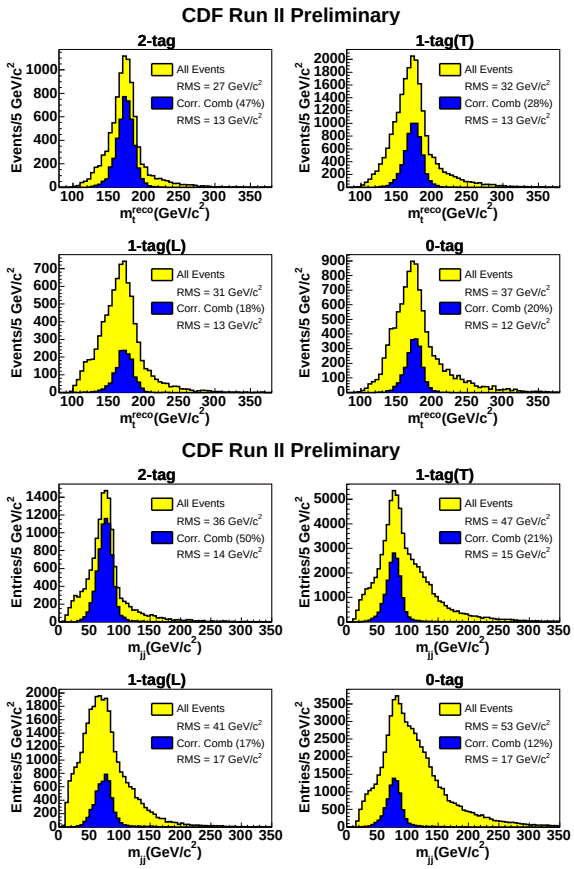

Fig. 29. Sample templates for m_{fit} and m_{jj} for the CDF ℓ+jets data[144].

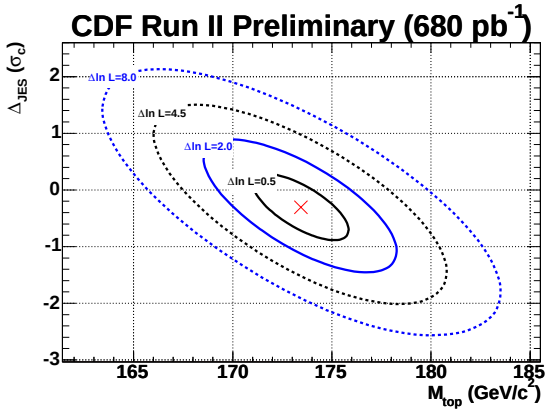

Fig. 30. Contour plot of the likelihood for the template fit to the CDF ℓ+jets data[144]. This shows the measured shift in jet energy calibration as it is correlated with the measured m_t.

data sample with integrated luminosity of 1.7 fb^{-1} the top quark mass is measured to be $m_t = 171.6 \pm 2.1(\text{stat} \oplus \text{jes}) \pm 1.1(\text{sys})$ GeV [124].

6.4.2. *Matrix element method*

The matrix element method was developed by DØ between Run I and Run II. It was used first on the Run I data set to obtain a top quark mass measurement of $m_t = 180.1 \pm 3.6(\text{stat}) \pm 3.9(\text{sys})$ GeV[134]. A significantly improved statistical precision was achieved compared to the previous measurement $m_t = 173.3 \pm 5.6(\text{stat}) \pm 5.5(\text{sys})$ GeV[146] on the same data set which used the template technique.

The idea is to compute for each event the probability density to observe the event as a function of the top quark mass, based on the full kinematic information from the event. This probability density is given by

$$p_{evt}(x|m_t, \alpha, f) = f p_{top}(x|m_t, \alpha) + (1 - f) p_{bkg}(x|\alpha). \tag{13}$$

Here x stands for all measured quantities in the event, i.e. the momenta of the charged lepton, the jets and the $\not\!\!E_T$. α is a scale parameter for the jet energies, and f represents the fraction of top quark decay events in the data sample. The event-by-event probability densities are combined into a joint likelihood for all events in the sample,

$$-\ln L(x_1 ... x_n|m_t, \alpha, f) = -\sum_{i=1}^{n} \ln p_{evt}(x|m_t, \alpha, f). \tag{14}$$

The measurement of the top quark mass is then the value of m_t that maximizes L for any value of the parameters α and f.

The signal probability density is given by the differential cross section normalized to the total cross section $\sigma_{t\bar{t}}(m_t)$ for all events accepted by the analysis cuts. It is given by

$$p_{sig}(x|m_t, \alpha) = \frac{1}{\sigma_{t\bar{t}}(m_t)} \int dz d\overline{z} f(z) f(\overline{z}) d\sigma_{t\bar{t}}(y, m_t) W(x|y, \alpha), \tag{15}$$

where z and $\overline{z}$ are the fractions of the proton and antiproton momenta carried by the initial partons, $f(z)$ is the parton distribution function for the proton, y represents the momenta of all partons taking part in the hard scatter event. The transfer function $W(x|y, \alpha)$ gives the probability to measure the observables x for the parton momenta y and the jet scale parameter α. The parton cross section $d\sigma_{t\bar{t}}$ is calculated based on the leading-order matrix element $\mathcal{M}$ for the process $q\overline{q} \to t\bar{t} \to \ell\nu b q\overline{q}'\overline{b}$:

$$d\sigma_{t\bar{t}}(y, m_t) = \frac{|\mathcal{M}|^2}{x\overline{x}s} d\Phi_6, \tag{16}$$

where $d\Phi_6$ is the Lorentz-invariant six-particle phase space element and s is the parton center of mass energy. In order to make p_{sig} calculable with reasonable computing power, a number of simplifying assumptions must be made. Typically

these are assuming that $p_T(t\bar{t}) = 0$, that all angles are well measured and that the transfer function factorizes into contributions from each final state object. After these assumptions the remaining six integrations can be carried out using Monte Carlo integration techniques. The calculation is carried out for all possible jet-parton assignments and for both solutions of p_z of the neutrino. These contributions are then added together for the final value of p_{sig}. A similar calculation is carried out for p_{bkg} except that this quantity does not depend on the top quark mass.

The power of this method originates from the use of all kinematic information from the events and the use of signal and background probabilities for each event. This effectively weights events in the event likelihood L that are more likely to be from top quark decay stronger than events that are more likely to be background. The downside is that the phase space integration is very computationally intensive.

The DØ Collaboration published a measurement of the top quark mass using the matrix element method based on 370 pb^{-1} of data from Run II[147]. In this measurement DØ makes use of b-tagging to give higher weight to jet permutations that assign b-tagged jets to b-quarks. This leads to a reduction in the combinatoric background and improves the statistical precision of the measurement. The result of this measurement is $m_t = 170.3^{+4.1}_{-4.5}(\text{stat}\oplus\text{jes})^{+1.2}_{-1.8}(\text{sys})$ GeV. The measurement was updated using a data sample corresponding to an integrated luminosity of 1 fb^{-1}[148]. Figure 31 shows a contour plot of the event likelihood L defined in equation 14 as a function of the assumed top quark mass m_t and the jet energy scale factor α. Plots in Fig. 32 show the projections onto the two axes. The updated measurement applied to b-tagged events yield a top quark mass of $m_t = 170.5 \pm 2.4(\text{stat} \oplus \text{jes}) \pm 1.2(\text{sys})$ GeV. The first uncertainty is derived from the width of the likelihood and accounts for both the statistical uncertainty and the uncertainty from the jet energy scale calibration. Ensemble tests show that the matrix element algorithm results in a measured value of the top quark mass that tracks the input top quark mass with a small offset. Figure 33 shows a plot of measured top quark mass versus input top quark mass for this analysis. The result is corrected for the observed offset.

An analysis using the same technique is carried out by CDF using a sample of 940 pb^{-1} of data [149]. The events are required to have a lepton, $\not\!\!E_T$ and only four jets, out of which one is expected to be tagged as a b-jet. This sample yields a measurement of $m_t = 170.9 \pm 2.2(\text{stat} \oplus \text{jes}) \pm 1.3(\text{sys})$ GeV.

By combining the signal probability computed using the matrix element technique with a Neural network discriminant to reject backgrounds, CDF experiment has measured $m_t = 170.9 \pm 1.3(\text{stat}) \pm 1.2(\text{jes}) \pm 1.2(\text{sys})$ GeV This measurement is based on a data sample with integrated luminosity of 1.7 fb^{-1} [124].

6.4.3. *Quantized dynamical likelihood method*

CDF has developed another method, based on Ref. [150], called the quantized dynamical likelihood method. In this analysis only events with exactly four jets are used. The four jets are assigned to partons in every possible way with the restriction

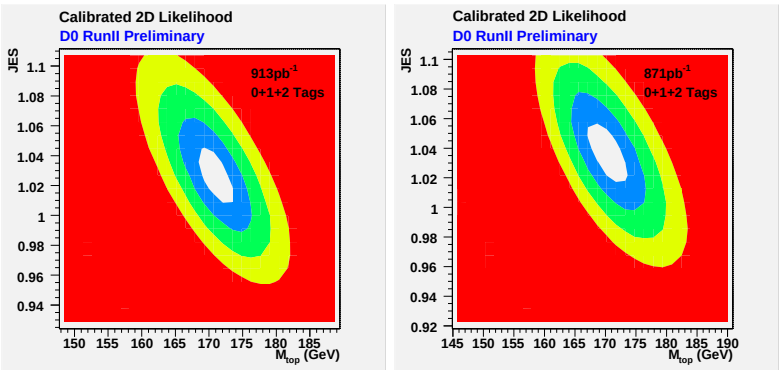

Fig. 31. Contour plot of the likelihood for the matrix element analysis of the D0 e+jets data (left panel) and μ+jets data (right panel) [148].

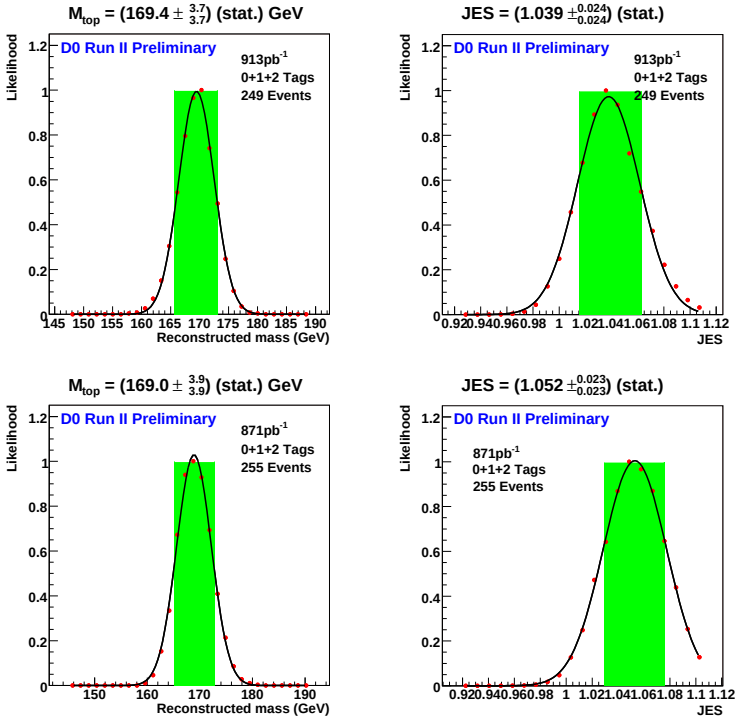

Fig. 32. Likelihood versus top quark mass (left), and jet energy scale (right) for the matrix element analysis of the DØ e+jets data (top plots) and μ+jets data (bottom plots) [148].

that b-tagged jets are only assigned to one of the b quarks.

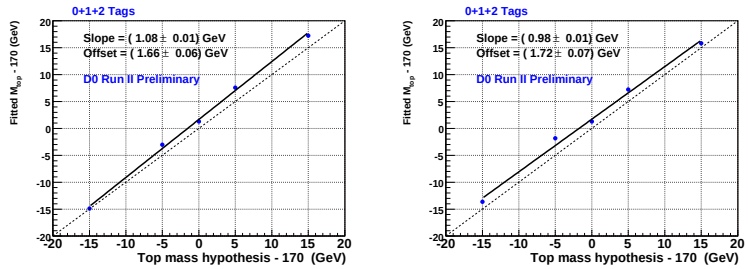

Fig. 33. Measured top quark mass from ensemble tests versus input top quark mass for matrix element analysis of the DØ e+jets data (left) and μ+jets data (right)[148].

For each permutation a likelihood is computed as

$$L_1(m_t) = \frac{d\sigma}{d\Phi_6}, \tag{17}$$

where $d\Phi_6$ is the Lorentz-invariant six particle phase space element and $d\sigma$ is the differential $t\bar{t}$ production cross section integrated over the momentum fractions z and $\bar{z}$ of the initial state partons and the transverse momentum $p_T(t\bar{t})$ of the $t\bar{t}$ system:

$$d\sigma = \int\int\int dz d\overline{z} f(z) f(\overline{z}) d^2 p_T(t\bar{t}) f(p_T(t\bar{t})) d\sigma_{t\bar{t}}(x, m_t), \tag{18}$$

where $f(p_T(t\bar{t}))$ is the expected p_T distribution of the $t\bar{t}$ system, $d\sigma_{t\bar{t}}(x, m_t)$ is the parton cross section defined in section 6.4.2 and all other parameters are also as defined in the same section.

The likelihood L_1 is typically averaged over 50,000 random generations of the parton momenta x from the observed jet momenta using Monte Carlo derived transfer functions. These functions are taken over all possible jet-parton assignment and over the two possible values of the z-component of the neutrino momentum to obtain the event likelihood $L(m_t)$. This joint likelihood for all events is computed by multiplying together all the event likelihoods. The top quark mass is measured as the hypothesized top quark mass for which the joint likelihood is maximized. Finally, this result is corrected for the effects of backgrounds in the sample. This correction is determined from ensemble tests using Monte Carlo data.

Using a data sample of 63 $t\bar{t}$ candidates in the lepton+jets channel with at least one b-tagged jet from 318 pb^{-1} of data, CDF measures $m_t = 173.2^{+2.6}_{-2.4}(\text{stat}) \pm 3.2(\text{sys})$ GeV.

6.4.4. *Ideogram method*

The ideogram method[152] is based on ideas that were used by the Delphi Collaboration to measure the W boson mass[153]. It was first adapted for the measurement

of the top quark mass by the DØ Collaboration. It is based on the same general idea that was developed for the matrix element method in equations 13 and 14. The difference lies in the definitions of p_{sig} and p_{bkg}. In order to reduce computing requirements, this analysis method makes use of the same kinematic fit as the template method.
The signal probability is defined as

$$p_{sig}(o|m_t,\alpha) = \tilde{p}_{sig}(D)\sum_{i=1}^{24}\exp\left(-\frac{\overline{\chi}_i}{2}\right)\left[f\int G(m_i,m',\sigma_i)B(m',m_t)dm' + (1-f)S(m_i,m_t)\right]. \tag{19}$$

Here D is a discriminant based on the kinematic observables in the event that is constructed such that most top quark like events have $D \approx 1$ and most background like events have $D \approx 0$ and $\tilde{p}_{sig}(D)$ is the probability density for signal events with discriminant value D. The sum over i runs over all 12 jet permutations and the two solutions for p_z of the neutrino. $\overline{\chi}_i^2$ is the minimum value of the χ^2 goodness of fit variable for the kinematic fit described in section 6.4.1 and m_i is the corresponding value of the hypothesized top quark mass. $G(x, x_0, \sigma)$ is a Gaussian bell curve with mean x_0 and width σ and $B(x, x_0)$ is a Breit-Wigner function of mean x_0. The integral is a convolution of the Breit-Wigner line shape of the top quark with a Gaussian resolution function and represents the contribution from jet permutations with the correct jet-parton assignments and f indicates the probability that a jet permutation corresponds to the correct jet-parton assignments. $S(m_i, m_t)$ represents the contribution of jet permutations with the wrong jet-parton assignments. Figure 34 shows the event likelihood curves for simulated events with zero, one, or two tags. The background probability density p_{bkg} is determined using a Monte Carlo simulation.

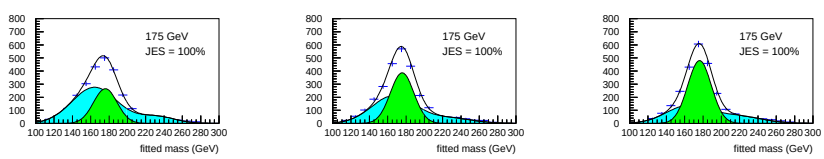

Fig. 34. Event likelihoods for simulated DØ ℓ+jets events with 0, 1, or 2 tags[152].

The DØ collaboration has applied this technique to the same data set as was used by the matrix element analysis described in section 6.4.2 except that the ideogram analysis uses events with four or more jets. Figure 35 (left plot) shows a contour plot of the event likelihood L defined in equation 14 as a function of the assumed top quark mass m_t and the jet energy scale factor α. Figure 35 (right plot) shows the likelihood versus top quark mass. The result of this measurement is $m_t = 173.7 \pm$

$4.4(\text{stat} \oplus \text{jes})^{+2.1}_{-2.0}(\text{sys})$ GeV. The first uncertainty is derived from the width of the likelihood and accounts for both the statistical uncertainty and the uncertainty from the jet energy scale calibration. Ensemble tests show that the ideogram algorithm results in a measured value of the top quark mass that tracks the input top quark mass with a small offset. The final quoted result includes this calibration.

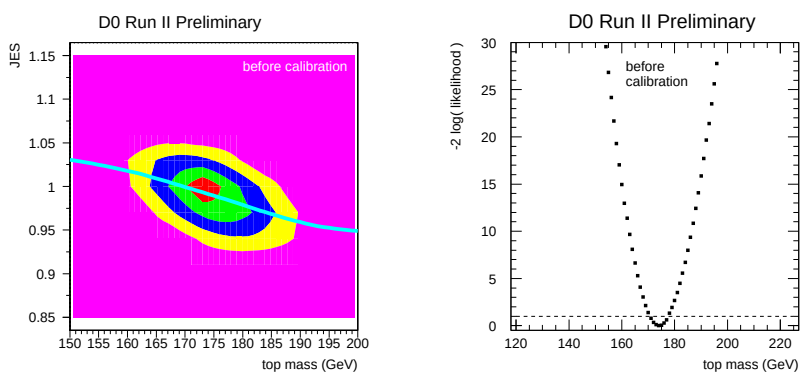

Fig. 35. Contour plot of the likelihood (left) and Likelihood versus top quark mass for the ideogram analysis of the DØ ℓ+jets data[152].

6.4.5. *Decay length distribution*

In addition to the measurement techniques described in the past few sections, the CDF collaboration has measured the top quark mass from the decay length distributions of b-hadrons from top quarks decays. The mean momentum of the b-quarks from the decays of top quarks increases with the top quark mass. A harder momentum spectrum leads to a higher Lorentz-factor and a longer decay length in the lab frame. Thus the decay length spectrum of b-hadrons from top quark decays can yield a measurement of the top quark mass, albeit with significantly poorer statistical sensitivity than the methods that are based on the kinematic reconstruction of the top quark decay. The advantage is that this method has different systematic uncertainties. Most importantly, it does not depend strongly on the jet energy scale calibration. The result of this measurement is $m_t = 180.7^{+15.5}_{-13.4}(\text{stat}) \pm 8.6(\text{sys})$ GeV [154].

6.5. *All-jets channels*

Events in which both W bosons decay to quark pairs provide another avenue with which to measure the top quark mass. The lack of a neutrino simplifies the kine-

matic reconstruction by removing quadratic ambiguities and providing for an over-constrained fit from the momenta of six jets. The large all-jets branching fraction provides a potentially substantial source of data that is essentially uncorrelated with the leptonic modes. On the other hand, a very high background persists even though $b-$tagging is used. This substantially impacts the statistical power of this channel. The Tevatron experiments have pursued several analyses to measure m_t in the all-jets channel: three template-based measurements, an ideogram analysis and a matrix element analysis.

6.5.1. *Template methods*

Templated approaches for the all-jets mass extraction have been tried by CDF in Run II[155] and I[106], and by DØ using Run I data published in 2005[156]. The most sensitive of these is the Run II CDF analysis which is a preliminary result that used 1.02 fb^{-1}. All three use event kinematic selections very similar to those described in Section 4.5. At least six jets are required in all cases, and CDF relaxed its initial ΣE_T cut to minimize the bias to the mass measurement. The DØ analysis used soft μ-tagged all-jets events, while CDF used secondary vertex b-tagged events.

To model signal, top quark events were modeled by both experiments using Herwig. CDF considered masses from 150 GeV to 200 GeV in their Run II analysis. Backgrounds were estimated similarly by both experiments. An untagged multijet sample was selected just as the signal sample. Known mistag rates were then applied to properly weight events when constructing templates. Estimatation of signal and background levels gave 334 events and 573 events, respectively, for CDF's Run II sample. The Run I analyses had 65 and 136 events total for DØ and CDF, with 48 and 108 expected background events, respectively.

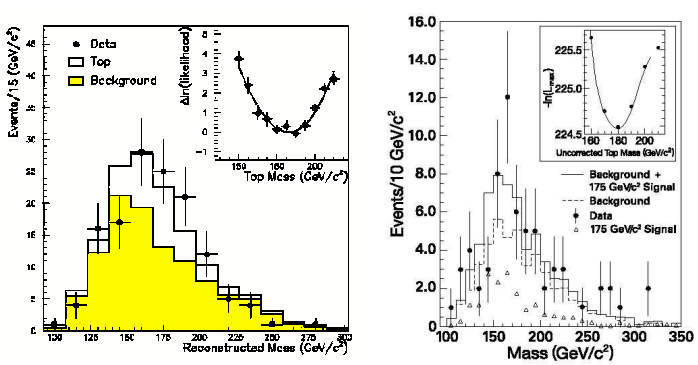

Fig. 36. The CDF measurement of the top mass in the all-jets final state using Run I data (left)[106]. Expected background and top quark signal are shown in solid, and data points provide data. At right is the DØ distribution [156]. Insets at upper right of both plots provide the fit used to determine the mass.

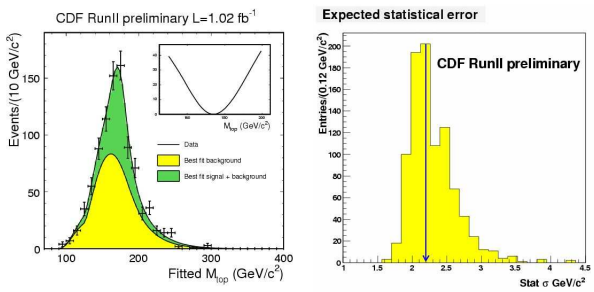

Fig. 37. The result of the template analysis of 1 fb^{-1} of CDF Run II data is shown with signal and expected background components (left). The inset at upper right provides the resulting $-ln(L)$ vs. m_t. The distribution of expected statistical uncertainties (right) [155] is also provided showing the result from data (see arrow).

Kinematic reconstruction of the candidate events was performed. For this reconstruction, each of the six highest E_T jets was associated with one of the quarks from a top quark or W boson decay. Tagged jets were specifically associated with $b-$quarks. There is an ambiguity in how the jets are assigned in pairs to W bosons and how these are associated with $b-$jets to form each top quark. Resolving this situation involved considering all possible configurations and calculating a χ^2 with respect to a correct $t\bar{t}$ configuration. Each configuration presents two jet triplets purported to originate from each top quark. For example, DØ defined a χ^2 for each configuration,

$$\chi^2 = \left(\frac{m_{t_1} - m_{t_2}}{2 \times \sigma_{m_t}}\right)^2 + \left(\frac{M_{W_1} - M_{W_0}}{\sigma_{M_W}}\right)^2 + \left(\frac{M_{W_2} - M_{W_0}}{\sigma_{M_W}}\right)^2 \tag{20}$$

where $M_{W_0}(= 77.5)$ GeV is the mass reconstructed in $t\bar{t}$ simulation for the two jets from a W boson. The values of M_{W_i} and m_{t_i} correspond to the masses calculated from the jet pair or triplet for the ith W boson or top quark, respectively, given the configuration being considered. All analyses resolved the combinatoric ambiguity by selecting the one with the lowest value of the χ^2. Using this combination, the invariant masses of three jet groupings were calculated. They are shown in Fig. 36 for the Run I measurements, and Fig. 37 for the analysis in 1 fb^{-1}.

This distribution is fit using expectations for backgrounds and for a top quark of varying mass and background. CDF in Run II has used a convolution of one gaussian and two gamma functions to represent the signal shape, and two gaussians plus a gamma function for background. The background shape was adjusted for a small estimated top quark contamination. CDF obtained measurements of $m_t = 174.0 \pm 2.2(\text{stat}) \pm 4.8(\text{sys})$ GeV and 186 ± 10 GeV in Run II and Run I, respectively. The primary systematic uncertainties in the former arose from the jet energy scalibration and the Monte Carlo modeling of the top quark signal. When applying the maximum likelihood fit, DØ allowed both signal and background levels to float. The fitted mass

is 178.5 ± 13.7 (stat) GeV. The systematic uncertainties for jet energy calibration, b-tag rate, and background statistics totalled 7.7 GeV.

6.5.2. *Matrix element analyses*

As with other channels, matrix element techniques have now been exploited in the all-jets channel, to date by CDF [157,158]. The former is actually a variant of the ideogram method used in ℓ+jets samples but also incorporating the matrix element approach to perform the m_t determination. This preliminary result was obtained from 310 pb^{-1} of b-tagged all-jets data. Each event presents 90 potential configurations of grouping jets to form W's and top quarks. All combinations are considered when performing a kinematic fit. Goodness of fit and the probability that two jets are b-jets were used to pick the right configuration. A two dimensional likelihood was performed in terms of the masses of the two top quarks, m_{t1} and m_{t2}. The shape of the signal was obtained from Pythia and Herwig using Gaussian resolution functions for jets obtained from data. The QCD background was modeled with Alpgen. The likelihood yielded a measurement of $m_t = 177.1 \pm 4.9(\text{stat}) \pm 4.7(\text{sys})$ GeV. The leading systematic uncertainties were the jet energy calibration and the background shape.

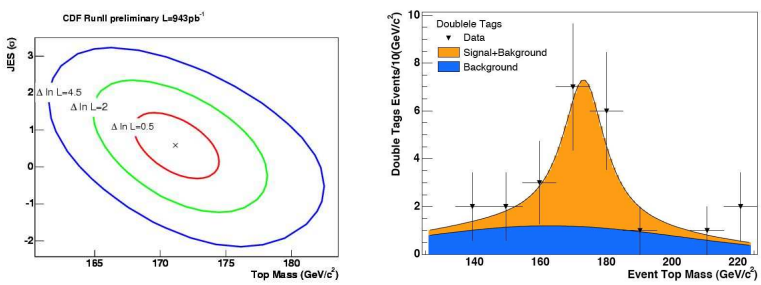

Fig. 38. Contour plot of the favored region in the jet energy scale vs. m_t for the CDF matrix-element analysis of 943 pb^{-1} of data [158](left). The distribution of fitted top mass for the double tagged sample is shown at right. Expected signal and background are shown.

Using a pure matrix-element approach, CDF has also generated a preliminary result[158] in 943 pb^{-1} which is an indicator of things to come. The event selection requires six jets with a scalar sum of their E_T of more than 280 GeV. Spherically distributed events which tend to have central jets are kept if they have at least one b-tagged jet. Extraction of the top quark mass proceeds by first estimating a probability vs. top quark mass using a matrix-element calculation. Transfer functions were used to relate reconstructed jet spectra to parton level momenta. This weight distribution is then used as a template and the data is compared to templates generated from signal and background Monte Carlo. By relating the fitted dijet masses from W bosons according to each jet-quark combination chosen to the expectation

from $W \to jj$, an estimate can be made of the residual jet energy scale as well as the measured correction to the top quark mass. This relation is shown in Fig. 38. This serves to validate the method and provide a systematic uncertainty for the residual jet energy scale. The fitted mass distribution for double-tagged candidate events is also shown in Fig. 38. The CDF analysis yielded a result of $m_t = 171.1 \pm 4.3$ GeV where 2.1 GeV of the uncertainty is due to systematic effects.

6.6. *Combined fits and electroweak constraints*

The Tevatron Electroweak Working Group[125] has performed combinations of the top quark mass measurements by DØ and CDF, properly taking into account correlations between the measurements in different channels and from both experiments. As of March 2007, the most precise value for the top quark mass is 170.9 ± 1.8 GeV [125]. More details on the combined results are given in Table 10. Their implications are discussed in Section 9.2.

The measured value of the top quark mass can be compared to the value of the top quark mass from the global electroweak fit performed by the LEP Electroweak Working Group[159]. Based on the Z lineshape measurements a value of $172.6^{+13.2}_{-10.2}$ GeV is most consistent with the standard model. If one includes in addition the measured W boson mass and width into the fit, the best top quark mass goes up to $178.9^{+11.7}_{-8.6}$ GeV. Either value is completely consistent with the value from the direct measurement.

Table 10. Summary of Top Quark Mass Measurements.

Channel	Experiment	Measured Mass (GeV/c^2)
$\ell\ell$	CDF	164.5± 5.6
$\ell\ell$	DØ	172.5± 8.0
ℓ+jets	CDF	170.9± 2.5
ℓ+jets	DØ	170.5± 2.7
All-jets	CDF	171.1±4.3
Lepton+jets (L_{xy})	CDF	183.9± 15.8

7. Properties of the Top Quark

As with the other fundamental fermions, the ability to study the top quark presents new opportunities to test our current understanding. Measuring the charge of the top quark helps to confirm if the particle discovered in 1995 is in fact the weak isospin partner to the b-quark. Determining V_{tb} will either confirm or refute whether we live in a world confined to three quark doublets. Several properties of the top quark have been measured so far and the increasing sizes of data samples

are placing real constraints on fundamental physics.

7.1. *W boson helicity measurements*

The high mass of the top quark raises the question whether there are new interactions near the electroweak symmetry breaking energy scale. Measuring the helicity of the W boson from top quark decay probes the tWb vertex and provides a stringent test of the standard model. A general form of the Lagrangian for the tWb interaction is given in Ref.[161]. It contains four form factors: f_1^L, f_1^R that parameterize the $V-A$ and $V+A$ interactions, and f_2^L, f_2^R which reflect the strength of an anomalous weak magnetic moment. In the SM, the coupling of W bosons to fermions is purely $V-A$, and therefore the only non zero form factor is f_1^L. If the tWb couplings are standard, then top quarks decay to left-handed W bosons (W_-) or to longitudinal W bosons (W_0). In the presence of non-standard couplings such as $V+A$, some admixture of right-handed W bosons (W_+) is expected.

7.1.1. *Sensitive Variables*

Measurement of the W boson helicity can be performed using any leptonic top quark decay. CDF and DØ have analyzed both their dilepton and ℓ+jets samples to extract limits on the W boson helicity using three sensitive variables.

- the helicity angle θ^*, defined as the angle between the charged lepton and the top quark directions in the W boson rest frame,
- the transverse momentum of the lepton in the laboratory frame,
- the invariant mass, $M_{\ell b}$, of the charged lepton and $b-$jet thought to come from the same top quark.

If we define θ^* as the angle of the decay positron in the W boson rest frame, with the polarization axis defined by the direction of the W boson in the top rest frame, then the angular distribution of the lepton with respect to the polarization of the W boson is given by

$$w(cos(\theta^*)) = f_-\frac{3}{8}(1-cos(\theta^*))^2 + f_0\frac{3}{8}(1-cos^2(\theta^*)) + f_+\frac{3}{8}(1+cos(\theta^*))^2$$

where f_-, f_0 and f_+ are the fractions of left-handed, longitudinal, and right-handed W bosons, respectively. In the SM f_-, f_0 and f_+ are expected to be 0.7, 0.3 and 0, respectively.

Computation of the helicity angle requires the reconstruction of the top quark and the pairing of the lepton with a jet in the event. Reconstruction of the top quark using semileptonic decays is performed using a constraint kinematic fit to the $t\bar{t}$ hypothesis (see Section 6.4). In the fit, M_W and m_t are fixed to their respective measured values. The fit is performed using all possible jet assignments, 12 in general, six if there is a single b-tagged jet, or two if there are two $b-$tagged jets. The permutation which gives the lowest χ^2 is chosen. Once the event is reconstructed, the helicity angle is computed after a boost to the rest frame of the reconstructed W boson.

When dilepton events are used, each event has two leptons and hence contributes twice to the measurement. Kinematic reconstruction of dilepton events is described in Section 6.3. Here, the presence of the two neutrinos kinematically underconstrains the system. For an assumed top quark mass, the kinematics are solved algebraically with a four-fold ambiguity in addition to the two-fold ambiguity which arises from the pairing of the lepton with the jet. Once the detector resolution effects are folded into the measurement, an average value of the helicity angle for each lepton is available.

Because the $M_{\ell b}$ and lepton p_T are directly determinable from the lab frame, using them greatly simplifies the analysis. They can also be readily applied in dilepton events as well as ℓ+jets events where one of the four final state jets might not have been reconstructed. The $M_{\ell b}$ approach relies on the fact that the helicity angle cosine, $cos(\theta^*)$, can be approximated by the expression[161]

$$cos(\theta^*) \simeq \frac{M_{\ell b}^2}{m_t^2 - M_W^2} - 1. \tag{21}$$

Each lepton-jet pairing proves a measurement of the angle. The lepton p_T method relies on the correlations in W boson momentum and that of its decay lepton. Left-handed W bosons tend to emit the charged lepton in the direction opposite to their direction of flight, longitudinal W bosons perpendicularly to their direction of flight, and right-handed W bosons emit the leptons preferentially along their direction of flight, leading to increasingly harder lepton p_T spectra. However, this method is less powerful than measuring the helicity angle.

7.1.2. *CDF Results*

The CDF experiment has pursued measurements of the polarization fractions of the W boson via both the $M_{\ell b}$ and lepton p_T measurements. These measurements have used three channels: dilepton, ℓ+ jets with one $b-$tagged jet, and ℓ+jets with two tagged jets. In each case, templates are generated for $t\bar{t}$ decays with $V + A$ and $V - A$ couplings as well as background events. A likelihood calculation is used to extract constraints on the non-standard couplings.

In an analysis published in 2005, the ℓ+jets sample was used in $\sqrt{s} = 1.8$ TeV collisions to provide a measurement of the $V + A$ decay rate at the tWb vertex [162]. They utilized the $M_{\ell b}$ method to place a limit on f_+. To strengthen the limits, they combined these results with earlier measurements of the W boson polarization using the lepton p_T, $f_0 = 0.91 \pm 0.37(\text{stat}) \pm 0.13(\text{syst})$[163]. A limit of $f_+ < 0.18$ was obtained at 95% C.L.

This was followed with a measurement in $\sqrt{s} = 1.96$ TeV collisions [164]. A 162 pb^{-1} sample of ℓ+jets events was used in both single and double tagged channels. Both the M_{lb} and lepton p_T measurements were employed for these channels. Dilepton events from 193 pb^{-1} were also used to obtain f_0 and f_+ via the lepton p_T technique. Each dilepton event provides two measurements for each event. These

samples are described in Section 4.3 and 4.4. The primary difference in $\ell+$ jets event selection involved an additional requirement of a fourth jet with $p_T > 8$ GeV and $|\eta| < 2$. This allowed the events to be kinematically reconstructed with the $t\bar{t}$ hypothesis. m_t taken to be 175 GeV and the lepton-jet matching was performed based on the result of this fit.

In order to extract a measurement, templates were generated for the different samples. In all cases, one W boson was simulated with SM expectations and the other was forced to a chosen helicity. Leptons from the decay of this second W boson were used to generate $M_{\ell b}$ and p_T^{ℓ} templates for $t\bar{t}$ decays with $V - A$ and $V + A$ couplings and for background events.

These templates were used in a fit to data. To extract f_0, f_+ was fixed to zero, and to extract f_+, f_0 was fixed to the standard model expectation of 0.7. Interestingly, the value obtained in the dilepton sample ($f_0 = -0.54^{+0.35}_{-0.25} \pm 0.16$) was unphysical because of the soft p_T spectrum of the observed events. This result is consistent with $f_0 = 0.7$ only at the 0.5% level. It differs by 2 σ from the $\ell+$ jets measurement of $f_0 = 0.95^{+0.35}_{-0.42} \pm 0.17$. As indicated in section 6, the dilepton sample was analyzed and determined to be marginally consistent with the standard model. All results were combined to obtain $f_0 = 0.74^{+0.22}_{-0.34}(\text{stat} + \text{sys})$ and $f_+ = 0.00^{+0.20}_{-0.19}(\text{stat} + \text{sys})$.

This gives a limit of $f_+ < 0.27$ at 95% c.l. To account for correlations among uncertainties, Monte Carlo experiments were conducted to obtain the necessary correlation coefficient. Significant sources of systematic uncertainty came from background modeling, the uncertainty in the value of m_t, and the calibration of jet energies.

In 700 pb^{-1} of Run II data, CDF has used the $M_{\ell b}$ technique in dilepton, $\ell+$ jets with one $b-$tag and $\ell+$ jets with two tags [165]. The event selection follows Section 4.3 and 4.4. A fourth jet was not explicitly required in the $\ell+$jets sample. In constructing templates for the $\ell+$jets samples, the following observations can be made. In the single tag case, the tagged jet comes from the same top quark as the identified lepton in about 50% of the cases. For the double tag sample, there are two possible combinations of $b-$tagged jet with charged lepton. This led to the use of a one-dimensional $M_{\ell b}$ template for the former, and a two-dimensional template for the latter. Templates for background were obtained from Alpgen $Wb\bar{b}$ events and, for the single tag case, a 15% admixture of multijet instrumental background from data. The dilepton analysis considers each charged lepton as an independent measurement. In each case, there are two possible matches to the leading two jets in an event, which are assumed to be the $b-$jets. Like the double-tagged $\ell+$jets analysis, a two-dimensional template of $M_{\ell b}$ is generated for signal. The background was modeled by a 50%:30%:20% mix of $Z \to \ell\ell$, $W+$jets, and diboson processes. The $W+$jets instrumental background was obtained from data according to the prescriptions described in Section 4.3. The expectations from backgrounds for $\ell+$jets (dilepton) channels were validated in background-dominated one and two (one) jet samples in data. Figure 39 indicates the distribution of $M_{\ell b}$ for the $\ell+$jets data

sample. Both $V + A$ and $V - A$ expectations are shown for comparison.

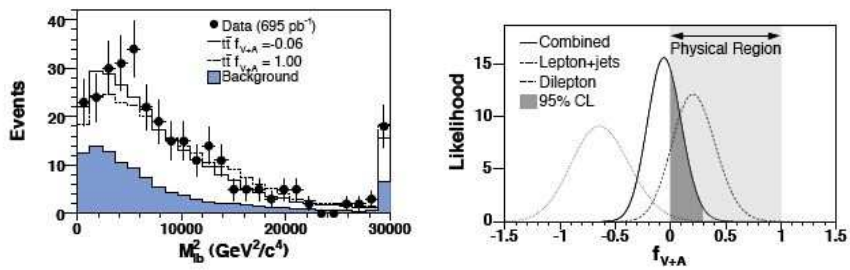

Fig. 39. Distribution of $M_{\ell b}$ in 700 pb^{-1} of CDF $\ell+$ jets events, with expected $t\bar{t}$ and background overlaid (left). Likelihood for dilepton, ℓ+jets and combined analyses indicating estimated f_{V+A} (right) [165].

To obtain an estimate of f_{V+A}, a binned log likelihood fit was employed to the data using templates from $t\bar{t}$ decays with $V + A$ and $V - A$ couplings and from background events. The $t\bar{t}$ and background cross sections were treated as nuisance parameters in the fit. The fitted values of these parameters were near the input values (e.g. $\sigma_{t\bar{t}} = 7.3 \pm 0.9$ pb). The validity of the fit method was explored by using ensemble testing where the $t\bar{t}$ and background composition was allowed to vary by the estimated uncertainty in these estimates. Ensembles were also constructed with a varying $V + A$ component. The measurement from the ℓ+jets analysis yields the fraction of $V + A$ current $f_{V+A} = 0.21 \pm 0.28$. Dilepton events yield $f_{V+A} = -0.64 \pm 0.37$. These results are approximately 1.8σ apart. The combined result gives $f_{V+A} = -0.06 \pm 0.25(\text{stat} + \text{sys})$. The likelihood vs. f_{V+A} for each channel, and the combined result, are shown in Figure 39. The primary systematic uncertainty came from the uncertainty in the jet energy scale. By using a Bayesian approach, an upper limit of $f_{V+A} < 0.29$ was obtained at 95% c.l. These results translate into a value for the fraction of right-handed W bosons of $f_+ = -0.02 \pm 0.07(\text{stat}) \pm 0.04(\text{sys})$ and a limit of $f_+ < 0.09$ at 95% C.L.

The most recent analysis of the W-boson helicity fractions from CDF[124] was performed using a dataset corresponding to an integrated luminosity of 1.7fb^{-1}, The distribution of the helicity angle cosine, $cos(\theta^*)$, was used to obtain the fractions of longitudinal f_0 or right-handed f_+ W-bosons. Fully reconstructed ℓ+jets $t\bar{t}$ events were used for this analysis. While all combinations of jet-parton assignments were processed via the kinematic fitter, the one with the smallest fit χ^2 was chosen as the final event configuration and was used for reconstructing the variable $cos(\theta^*)$. An unbinned likelihood fit to the observed $cos(\theta^*)$ distribution for the data was performed using templates for the longitudinal, right- and left-handed signal events and the background events. From this fit a measurement of the uncorrected longitudinal and right-handed fractions of W-boson events in the data was obtained. To convert

this measurement to the true longitudinal and right-handed fractions of events, a correction for the selection and reconstruction efficiencies was applied. Three different types of fits were employed. In all three fits the constraint $f_- + f_0 + f_+ = 1$ was imposed. Two 1-D fits correspond to the measurements of the fraction f_+ (f_0) with f_0 (f_+) fixed to the value expected from SM. If one constrains the right-handed fraction $f_+ = 0$, then the measurement of $f_0 = 0.57 \pm 0.11(\text{stat}) \pm 0.04(\text{syst})$. Constraining $f_0 = 0.7$ lead to a measurement $f_+ = -0.04 \pm 0.04(\text{stat}) \pm 0.03(\text{syst})$ or $f_+ < 0.07$ at 95% C.L.. The third fit was a simultaneous $2D$ fit for both parameters f_+ and f_0 and lead to a measurement of $f_0 = 0.61 \pm 0.20(\text{stat}) \pm 0.03(\text{syst})$ and $f_+ = -0.02 \pm 0.08(\text{stat}) \pm 0.03(\text{syst})$.

7.1.3. *DØ Results*

During Run II, DØ has performed measurements of the W boson helicity using the $cos(\theta^*)$ distribution. In the most recent publication[166], both dilepton and $\ell+$ jets events are used for the measurement. The event selection in both channels is similar to that used for the m_t measurements. The backgrounds for the $\ell+$jets events are mainly $W+$jets production and the instrumental background from misidentified multijet events. Discrimination between $t\bar{t}$ events and background events is obtained by constructing a discriminant which is close to one for signal $t\bar{t}$ events and near zero for background events. This discriminant is computed from variables that exploit the differences in the event kinematics and jet flavor of the signal and background events.

The kinematic variables used for building the discriminant include H_T, $\Delta\phi(\ell, \not{E}_T)$, aplanarity ($A$), sphericity ($S$) and the minimum dijet mass m_{jjmin}. These are described in Section 4.1. The χ^2 from the kinematic fit was also used.In addition a variable which distinguishes the flavors of the jets is obtained by using the impact parameters of the tracks in the jet with respect to the primary vertex. The impact parameters of tracks are used to form a probability for the jet to originate from the primary vertex. The average of the two smallest probabilities are used to characterize the event. This variable has smaller values for top quark events than for background events. For the dilepton channel, backgrounds arise mainly from $WW+$jets or $Z+$jets processes. After the selection of the events using kinematic quantities, a fairly good signal to background ratio is obtained and no further cut on an event discriminant is required.

Measurement of the W boson helicity is performed by fitting the $cos(\theta^*)$ distributions observed in both the dilepton and $\ell+$ jets data samples. The observed distribution is fit to two components: the expected backgrounds and a $t\bar{t}$ signal sample which is generated at specific values of f_+. During the fit, f_0 is fixed at 0.70 and f_+ is varied. The $cos(\theta^*)$ templates for signal samples are constructed by generating $t\bar{t}$ events with two different values of f_+=0 and f_+=0.30 and using a linear interpolation to generate a value of f_+. The backgrounds with real leptons are generated using ALPGEN and PYTHIA, and the multijet background templates are extracted

from the background control samples (see Section 6.4 for details). Figure 40 shows the $cos(\theta^*)$ distribution observed in $\ell+$ jets and dilepton events for a luminosity corresponding to 370 pb^{-1}. Overlaid on the figure are the expected distributions from the standard model prediction and a model with a pure $V + A$ interaction. A binned Poisson likelihood $L(f_+)$ is computed for the data to be consistent with the sum of signal and background templates at each of the chosen f_+ values in the range $0 < f_+ < 0.3$.

A parabola is fit to the $-ln[L(f_+)]$ points to extract the likelihood as a function of f_+. Systematic uncertainties are folded in prior to the determination of the final result. The dominant contributions to the systematic uncertainties arise from jet energy scale measurements and the input top quark mass. They are assumed to be fully correlated between the dilepton and $\ell+$ jets events. With the assumption that f_0 is fixed at 0.7, DØ measures $f_+ = 0.109 \pm 0.094(\text{stat}) \pm 0.063(\text{syst})$ using $\ell+$ jets events, and $f_+ = 0.089 \pm 0.154(\text{stat}) \pm 0.059(\text{syst})$using dilepton events. Combining the two yields $f_+ = 0.056 \pm 0.080(\text{stat}) \pm 0.057(\text{syst})$. A Bayesian confidence interval is computed using a flat prior distribution which is non-zero only in the physically allowed region of $0 < f_+ < 0.3$ leading to $f_+ < 0.23$ at 95% C.L.

An earlier analysis with 230 pb^{-1} data was also carried out by DØ [167]. The analysis strategies and techniques were similar to the ones described above. The main difference involved the further subdivision of the $\ell+$ sample into two categories depending on whether a tagged $b-$jet was found in the event. A likelihood analysis of the angular distribution of the leptons, leads to the result $f_+ = 0.0 \pm 0.13(stat) \pm 0.017(syst)$ and $f_+ < 0.25$ at 95% C.L. All measurements are consistent with the SM prediction f_0=0.7, f_+=0.

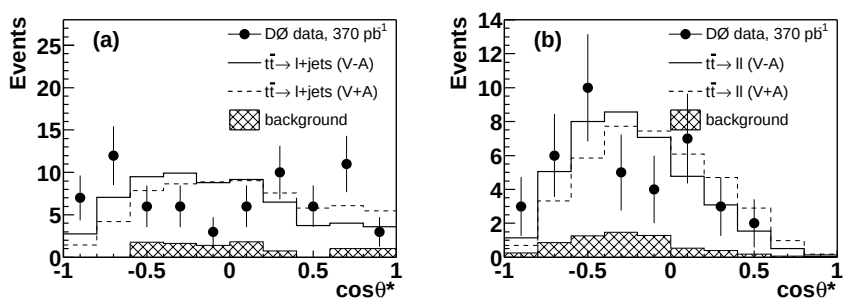

Fig. 40. Distribution observed in DØ ℓ+jets events (left) and dilepton events (right)[166]. The standard model predictions are shown as the solid lines. A model with a pure $V + A$ interaction would result in the distribution given by the dashed lines.

DØ also has carried out a first model independent measurement of the W boson helicity fractions on a larger dataset corresponding to an integrated luminosity of 1 fb^{-1}[168]. As described above, all earlier measurements of helicity fractions f_+, f_0 have been performed by keeping one of them fixed to the value predicted by the

SM and measuring the other by a fit to one of the kinematic variables sensitive to the W-boson helicity. The model independent study is based on a simultaneous measurement of f_+, f_0, with the condition that $f_+ + f_0 + f_- = 1$. This analysis also benefits from better event selection efficiency. The event selection efficiency and the background rejections compared to analyses on the smaller datasets are improved by using a likelihood based event discriminant. The likelihood discriminant is based on the following variables: H_T, centrality C, $k_T(min)$, the sum of all jet and charged lepton energies h, the minimum dijet mass of the jet pairs $m(jj)_{min}$, aplanarity A, sphericity S, $\not{E}_T$ and the dilepton invariant mass (for definitions of these variables see Section4). The likelihood discriminants $\mathcal{D}$, are computed independently for each of the different channels considered in the analysis (ee, $e\mu$, ee, e+jet, and μ+jet) and an appropriate selection on $\mathcal{D}$ is applied to maximize the signal to background for each channel. In addition, the neural network b-tagging algorithm was used to identify the b-jets.

The simultaneous measurement of f_0 and f_+ is performed using the distribution of $cos(\theta^*)$. A further enhancement in this analysis compared to previous ones is the use of the hadronicaly decaying W boson in the $cos(\theta^*)$ distribution in the $\ell + jets$ events. The distributions of $cos(\theta^*)$ for the leptonic and hadronic W bosons obtained in the $\ell + jets$ events is shown in Fig.41.

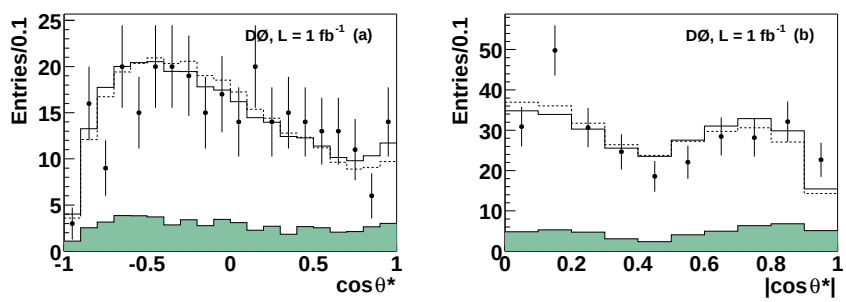

Fig. 41. Distribution of $cos(\theta^*)$ for the leptonic W bosons (left) and hadronic W bosons (right) obtained in the $\ell + jets$ sample.[168]. The data are represented by dots, the expected signal is shown as the dashed histogram and the shaded histogram corresponds to the expected background.

The simultaneous fit for f_0 and f_+ is performed using a binned Poisson likelihood $\mathcal{L}(f_0; f_+)$. The consistency of the data with the sum of signal and background templates as a function of the helicity fractions is computed, keeping the background normalization constrained to the expected value within uncertainties. With this procedure DØ obtains

$$f_0 = 0.425 \pm 0.166(\text{stat.}) \pm 0.102(\text{syst.})\text{and} f_+ = 0.119 \pm 0.090(\text{stat.}) \pm 0.053(\text{syst.}).$$

In Fig.42, the 68%, and 95% C.L. contours from the fit are shown compared to the prediction from SM. While the measurement may suggest a smaller fraction

of longitudinal W bosons and a larger fraction of right-handed W-bosons as compared to SM predictions, they are statistically consistent with the SM. Given the uncertainties in the measurement, DØ computes a 27% chance for observing the discrepancy.

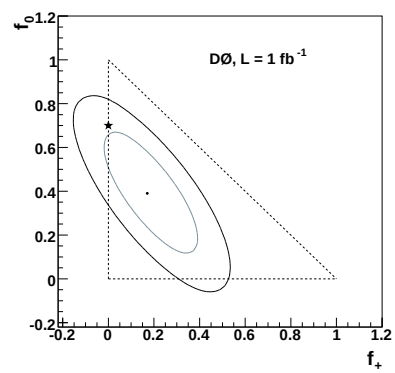

Fig. 42. Result of the model-independent simultaneous fit to the W boson helicity fractions f_0 and f_+. The star denotes the SM prediction, the ellipses represent the measured 68% and 95% C.L. contours. The triangle indicates the physically allowed region.[168].

Measurements of f_0 and f_- can also be performed using the earlier prescription of fixing one of the them to the SM value. Fixing f_+ to the SM value gives $f_0 = 0.619 \pm 0.090(\text{stat.}) \pm 0.052(\text{syst.})$ and fixing f_0 to the SM value leads to a value of $f_+ = -0.002 \pm 0.047(\text{stat.}) \pm 0.047(\text{syst.})$.

7.2. *Measurement of $B(t \to Wb)/B(t \to Wq)$ and $|V_{tb}|$*

The top quark decays predominantly via $t \to Wq$, where q can be a d, s, or a b-quark. Flavor changing neutral current (FCNC) decays of the type $t \to Vq$, where $V = g, Z, \gamma$ and $q = u, c$ are of the order of 10^{-10} or smaller within the SM[169]. In the SM, the ratio of top quark branching fractions, $R = BR(t \to Wb)/BR(t \to Wq)$, can be expressed in terms of the CKM matrix elements, $R = \frac{|V_{tb}|^2}{|V_{tb}|^2+|V_{ts}|^2+|V_{td}|^2}$. Based on the assumption of three quark generations and unitarity of the CKM matrix, and using the very small experimentally measured values of $|V_{ub}|$ and $|V_{cb}|$, one obtains $0.9990 < |V_{tb}| < 0.9992$ at 90% C.L.[48]. This also constrains R to be in the interval 0.9980–0.9984 at the 90% C.L.[48]. Thus, in the SM, the top quark is expected to decay nearly 100% of the time into a W boson and a b-quark. A significant deviation from the SM prediction of $BR(t \to Wb) \simeq$ unity could arise in the presence of additional quark generations or non-SM processes in the production or decay of the top quark. The identification of $t\bar{t}$ events at the Tevatron allows us

to check for such a possible deviation which would imply the appearance of new physics. In Run I, CDF measured $R = 0.94^{+0.31}_{-0.24}$(stat+sys) [170] and set a lower limit of R >0.61 (0.56) at 90% (95%) C.L., in agreement with SM predictions. In Run II, both CDF[171] and DØ [172] have reported direct measurements of R by examining the candidate $t\bar{t}$ events in data samples of ∼160 pb^{-1} and ∼230 pb^{-1}, respectively. These analyses assume that $t \to Xq$, where $X \neq W$ is negligible.

Analysis strategy: In the SM case with $R \approx 1$, the $t\bar{t}$ event signature contains two $b-$jets from the two top quark decays. However, with R of an unknown value, a $t\bar{t}$ event might have zero, one or two $b-$jets since the top quark can also decay into a light quark (d or s) and a W boson. The ratio $R = BR(t \to Wb)/BR(t \to Wq)$ determines the fraction of $t\bar{t}$ events with zero, one and two $b-$jets and therefore how $t\bar{t}$ events are distributed among samples with zero, one or two-tags. Thus R can be extracted from the relative rates of identified $b-$jets in $t\bar{t}$ events. If each of the two top quarks in the event has a probability R to decay to a b-quark, and there is an efficiency ϵ_b to tag the $b-$jet, the efficiencies to detect zero, one or two $b-$jets in the event are

$$\epsilon_0 = (1 - R\epsilon_b)^2, \epsilon_1 = 2R\epsilon_B R(1 - R\epsilon_b), \epsilon_2 = (R\epsilon_b)^2 \tag{22}$$

$$\Longrightarrow R\epsilon_b = \frac{2}{\epsilon_1/\epsilon_2 + 2} = \frac{1}{2\epsilon_0/\epsilon_1 + 1} = \frac{1}{\sqrt{\epsilon_0/\epsilon_2} + 1} \tag{23}$$

$$R\epsilon_b = \frac{2}{N_1/N_2 + 2} = \frac{1}{2N_0/N_1 + 1} = \frac{1}{\sqrt{N_0/N_2} + 1} \tag{24}$$

where N_i are the number of $t\bar{t}$ events observed with i tags, where i can be zero, one or two. Any two tagging rates determine $R\epsilon_b$ uniquely, while all three tagging rates jointly overdetermine $R\epsilon_b$. The ratios of tag rates can only determine the product $R\epsilon_b$, as it is not possible to distinguish missing tagged jets due to tagging inefficiency (ϵ_b less than unity) from missing tagged jets due to the absence of b-quarks (R less than unity). R can be extracted by measuring ϵ_b independently, from $t\bar{t}$ simulation calibrated with complimentary data samples. As R depends only on relative tag rates, this measurement is independent of any assumptions of the overall $t\bar{t}$ cross section ($\sigma_{t\bar{t}}$).

The measurement thus follows three basic steps. After identifying samples enriched in $t\bar{t}$ events, the background level in those events is estimated for different $b-$jet multiplicity. Then the expected tag rates (and, implicitly, their ratios) in $t\bar{t}$ events are predicted as a function of $R\epsilon_b$. Finally, the observed tag rates are compared to the expectations, yielding the most likely value of $R\epsilon_b$, and allowing to set a lower limit on R. This strategy was pioneered by CDF's Run I analysis[170].

Measurement by CDF: Based on ∼160 pb^{-1} of Run II data, CDF followed the same technique and determined R from the relative numbers of $t\bar{t}$ events with different multiplicity of $b-$tagged jets in the ℓ+jets and dilepton channels[171]. The

event selection, $b-$jet identification and the associated background estimation are essentially equivalent to the ones in the cross section analyses discussed in earlier sections. In particular, in the one-tag and two-tag subsamples of the ℓ+jets sample, *apriori* estimates of the background are made with a collection of data-driven and simulation techniques. In the zero-tag ℓ+jets sample, where the W+jets production rate dominates over the $t\bar{t}$ pairs, the event rate is determined by exploiting the unique kinematics of $t\bar{t}$ events with an artificial neural network (ANN). A binned maximum likelihood fit of the ANN output distribution is performed for the $t\bar{t}$ fraction in the subsample. In the dilepton channel, most of the jets in the background events arise from generic QCD radiation. To determine the background distribution across the subsamples with zero, one and two b-tags, a parameterization of the probability to tag a generic QCD jet, derived from jet-triggered data samples, is applied to the jets in the dilepton sample, correcting for the enriched $t\bar{t}$ content of the sample. Table 11 shows the observed number of events (N^{obs}) in the ℓ+jets and dilepton samples, and the corresponding estimates of background levels (N^{bkg}) and expected event yields (N^{exp}). The $t\bar{t}$ event tagging efficiency ϵ_i depends on the fiducial acceptances for jets that can potentially be $b-$tagged, and the efficiency to tag those jets. These efficiencies in turn depend on the species of the jet's progenitor quark. The efficiency ϵ_i thus depends strongly on R, as R not equal to unity implies fewer $b-$jets available for $b-$tagging, and more light-quark jets instead. The jet acceptances and tagging efficiencies are used to parameterize $\epsilon_i(R)$ using $t\bar{t}$ simulated events. The nominal values of ϵ_i for R equal to unity are also given in Table 11.

Table 11. Summary of observed and expected event yields as a function of $b-$jet multiplicity in the l+jets and dilepton samples in the CDF[171] and DØ [172] analyses.

	0-tag	1-tag	2-tag	0-tag	1-tag	2-tag
CDF (l+jets)				CDF (dilepton)		
ϵ_i(R=1)	0.45±0.03	0.43±0.02	0.12±0.02	0.47±0.03	0.43±0.02	0.10±0.02
N_i^{bkg}	62.4±9.0	4.2±0.7	0.2±0.1	2.0±0.6	0.2±0.1	<0.01
N_i^{exp}	80.4±5.2	21.5±4.1	5.0±1.4	6.1±0.4	4.0±0.2	0.9±0.2
N_i^{obs}	79	23	5	5	4	2
DØ (l+3 jets)				DØ (l+≥4 Jets)		
N_i^{tt}	32.4±1.6	32.3±1.6	8.2±0.5	35.6±2.8	41.5±3.3	13.5±1.4
N_i^{exp}	1275±44	79±5	11.4±0.8	297±19	56±4	14.4±1.4
N_i^{obs}	1277	79	9	291	62	14

The expected event yield in each of the three tagged subsets of ℓ+jets and dilepton samples is

$$N_i^{exp} = N_{inc}^{t\bar{t}}\epsilon_i(R) + N_i^{bkg} \tag{25}$$

where $N_{inc}^{t\bar{t}} = \sum_i (N_i^{obs} - N_i^{bkg})$ is an estimate of the inclusive number of $t\bar{t}$ events

in the sample. The analysis constructs a likelihood function using this information to get the best estimate of $R\epsilon_b$. The full likelihood is a product of independent likelihoods for the ℓ+jets and dilepton samples. Each likelihood function is built as the product of the Poisson functions comparing N_i^{obs} to N_i^{exp} for each value of i, multiplied by Gaussian functions which incorporate systematic uncertainties in the event-tagging efficiencies and backgrounds, taking into account the correlations across different subsamples. The resulting likelihood as a function of R is shown in Fig. 43, along with the negative logarithm of the likelihood, which gives a central value of $R = 1.12^{+0.21}_{-0.19}(stat)^{+0.17}_{-0.13}(sys)$ most consistent with the observation.

Measurement by DØ : The DØ experiment measures simultaneously the ratio of branching fractions R together with the $t\bar{t}$ production cross section, using 230 pb^{-1} of data and selecting a sample enriched in $t\bar{t}$ events which are consistent with ℓ+jets final states[172]. The $t\bar{t}$ enriched sample is divided into $\ell + 3$jets and $\ell + \geq 4$jets, which are further categorized on the basis of zero, one and two or more $b-$jets. The analysis fits simultaneously R and the total number of $t\bar{t}$ events ($N_{t\bar{t}}$) in the zero, one and two-tag samples to the number of observed one-tag and two-tag samples, and, in the zero-tag events, to the shape of a discriminant variable (D) that exploits kinematic differences between the background and the $t\bar{t}$ signal. The event selection, background determination and secondary vertex $b-$tagging algorithm are essentially equivalent to that of the corresponding cross section analyses described in the section 4.4.

In an analysis based on the SM, with $R \approx$ unity, the $t\bar{t}$ event tagging probabilities are computed assuming that each of the signal events contain two $b-$jets. In the present analysis with R not equal to unity, the $t\bar{t}$ event tagging probability becomes a function of R since a $t\bar{t}$ event might have zero, one or two $b-$jets. To derive the event tagging probability as a function of R, the event tagging probability is determined for the three following scenarios (i) $t\bar{t} \to W^+bW^-\bar{b}$, (ii) $t\bar{t} \to W^+bW^-\bar{q}_l$, and (iii) $t\bar{t} \to W^+q_lW^-\bar{q}_l$, where q_l denotes either a $d-$ or $s-$ quark. The probabilities P_{i-tag} to observe $i - tag =$ zero, one or $\geq$ two $b-$jets are computed separately for the three types of $t\bar{t}$ events, using the probabilities for each type of jet (b, c or light flavor jet) to be $b-$tagged. The probabilities P_{i-tags} in the three scenarios are then combined in the following way to obtain the $t\bar{t}$ tagging probability as a function of R:

$$P_{i-tag}(t\bar{t}\ ) = R^2P_{i-tag}(i) + 2R(1-R)P_{i-tag}(ii) + (1-R)^2P_{i-tag}(iii) \quad (26)$$

where the subscript $i - tag$ runs over zero, one and at least two tags. Table 11 compares the observed number of events with the sum of the predicted backgrounds and the fitted number of $t\bar{t}$ events as a function of the number of $b-$tags. To measure R and $\sigma_{t\bar{t}}$, a binned maximum likelihood fit is performed to the data. The values of R and $\sigma_{t\bar{t}}$ that maximize the total likelihood function are $R = 1.03^{+0.19}_{-0.17}$(stat+sys) and $\sigma_{t\bar{t}} = 7.9^{+1.7}_{-1.5}$(stat+sys)$\pm$0.5 (lum) pb, respectively, and in good agreement

with the SM expectation. The result of the 2-dimensional fit is shown in Fig. 43 in the plane (R, $\sigma_{t\bar{t}}$), along with the 68% and 95% confidence level contours. A preliminary simultaneous measurement of $\sigma_{t\bar{t}}$ and R was performed in 900 pb^{-1} of data [173]. This gives a measured value of $R = 0.97^{+0.09}_{-0.08}(\text{stat} + \text{sys})$.

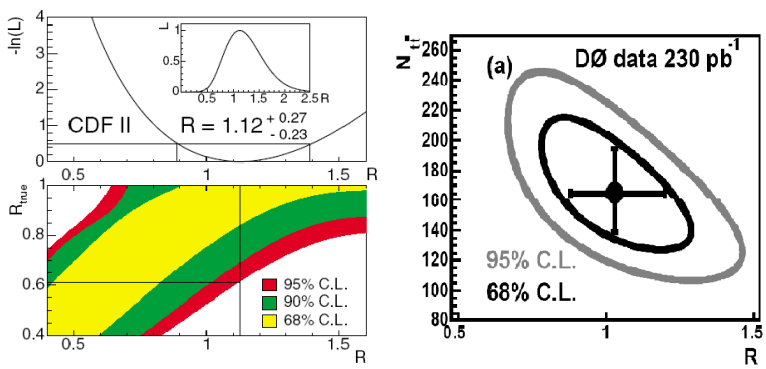

Fig. 43. Left: The upper plot shows the likelihood as a function of R (inset) and its negative logarithm. The intersections of the horizontal line ln(L)=-0.5 with the likelihood define the statistical 1σ errors on R. The lower plot shows 95% (outer), 90% (central), and 68% (inner) C.L. bands for R_{true} as a function of R by CDF[171]. Right: The 68% and 95% statistical confidence contours in the (R,$N_{t\bar{t}}$) plane by DØ [172]. The point indicates the best fit to the data.

With their measured values of R, CDF and DØ have set a lower limit on R. Assuming that non-W decays of the top quark can be neglected, that only three-generations of fermions exist, and that the CKM matrix is unitary, implying $R = |V_{tb}|^2$, they have extracted the CKM matrix element $|V_{tb}|$. The results of this measurement are summarized in the Table 12. All the measurements of R and $|V_{tb}|$ are consistent with SM expectations. These results are presently limited by statistics and will profit from the upcoming larger data sets.

Table 12. Published measurements and lower limits of $R = BR(t \to Wb)/BR(t \to Wq)$ and $|V_{tb}|$ from CDF[171] and DØ [172] in Run II.

	CDF ($\int \mathcal{L}$dt=160 pb^{-1})	DØ ($\int \mathcal{L}$dt=230 pb^{-1})
R	$1.12^{+0.27}_{-0.23}$	$1.03^{+0.19}_{-0.17}$
R (95% C.L.)	>0.61	>0.61
R (68% C.L.)	–	>0.78
$\|V_{tb}\|$ (95% C.L.)	>0.78	>0.78
$\|V_{tb}\|$ (68% C.L.)	–	>0.88

First direct determination of $|V_{tb}|$ by DØ : Single top quark cross section measurement provides a direct determination of the CKM matrix element $|V_{tb}|$ since the cross section is proportional to the square of this quantity ($\sigma \propto |V_{tb}|^2$). A value inconsistent with the SM expectation $|V_{tb}| \simeq 1$ would be a signature for new physics such as a fourth quark family. The DØ experiment has performed the first direct measurement of $|V_{tb}|$ based on the single top quark cross section measurement derived from decision trees analysis (discussed in section 5.2) using about 0.9 fb^{-1} of data[110]. This result makes no assumptions on the unitarity of CKM matrix or the number of families, but it does require a few assumptions. First, it is assumed that the single top quark production meachanism only involves interaction with a W boson, and not from one of the various beyond SM scenarios that include extra scalar and vector bosons or FCNC interactions. The second assumption made is that $|V_{td}|^2 + |V_{ts}|^2 \ll |V_{tb}|^2$, which is experimentally supported by the $BR(t \to Wb)/BR(t \to Wq)$ measurements done on $t\bar{t}$ events. This requirement implies that $BR(t \to Wb) \simeq 100\%$ and that single top quark production is completely dominated by the tbW production. Finally, it is assumed that the tbW interaction is CP-conserving and of the $V-A$ type, but it is allowed to have an anomalous strength. Two measurements have been performed, one for the strength of the $V-A$ coupling $|V_{tb} f_1^L|$ in the Wtb vertex, where f_1^L is an arbitrary left-handed form factor, with no requirement that it be less than one; and one assuming $f_1^L = 1$ resulting in $|V_{tb}|$ being restricted to between 0 and 1. The limits calcualted using Baysian approach are: $|V_{tb} f_1^L| = 1.3 \pm 0.2$ and $0.68 < |V_{tb}| < 1$ at the 95% C.L.[110].

7.3. *Top Quark Charge*

Many of the currently measured properties of the top quark are still only poorly known, and the indirect constraints set by precision electroweak data leave plenty of room for new physics. In particular, its electric charge (q_t), one of the most fundamental quantities characterizing a particle, has not been directly measured so far. It still remains not only to confirm that the discovered quark has a charge $+\frac{2}{3}$ as assigned by the SM, but also to measure the strength of its electromagnetic (EM) coupling to rule out anomalous contributions to its EM interactions. In the top quark analyses of the CDF and DØ experiments, the correlations of the b-quarks and the W bosons in $p\bar{p} \to t\bar{t} \to W^+W^-b\bar{b}$ are not uniquely determined which results in a two-fold ambiguity in the pairing of W bosons and b-quarks, and, hence, in the electric charge assignment of the top quark. In addition to the SM assignment $t \to W^+b$, it is conceivable that the 't-quark' is an exotic quark Q with charge q= $-\frac{4}{3}$ which decays via $Q \to W^-b$. This alternative interpretation is consistent with current precision electroweak data. It is possible to fit $Z \to \ell^+\ell^-$ and $Z \to b\bar{b}$ data assuming a top quark mass of $m_t = 270$ GeV, provided that the right-handed b-quark mixes with the isospin $+\frac{1}{2}$ component of an exotic doublet of charge $-\frac{1}{3}$ and $-\frac{4}{3}$ quarks, $(Q_1\ , Q_4)_R$[174]. In such a scenario, the particle we have been exploring may in fact be the $-\frac{4}{3}$ charge quark and the top quark, with m_t=270 GeV, would

have so far escaped detection at the Tevatron.

Specific q_t measurements are therefore required to rule out or confirm one of the hypotheses. In order to determine q_t, one can study the charge of its decay products or investigate photon radiation in $t\bar{t}$ events. The latter method[175] consists in cross-section measurements of $t\bar{t}$ pairs where a photon is radiated, either at the production ($p\bar{p} \to t\bar{t}\gamma$) or the decay ($p\bar{p} \to t\bar{t}$, $t \to Wb\gamma$); the radiation being dependent on the value of q_t. Measurement of q_t using radiative $t\bar{t}$ processes is hopeless at the Tevatron[175] - even with 20 fb^{-1} of data, a charge $-\frac{4}{3}$ top quark can be excluded at ≈95% confidence level. However, at the LHC, with 10 fb^{-1}, one can hope to determine q_t with a precision of ≈10%. The first method - measuring q_t by reconstructing the charges of its decay products (the final-state $b-$jets and the W bosons) for semi-leptonic decays - seems feasible at the Tevatron. The W boson charge in leptonic decays is accurately given by the lepton coming from it and the b-jet charge can be determined from a measurement of charges associated with the tracks in the jet. It should be noted that since both t and $\bar{t}$ quarks are present in every event, the analysis is only sensitive to the absolute value of q_t.

The DØ experiment has performed the first determination[176] of q_t with ∼370 pb^{-1} of Run II data on a double-tagged semi-leptonic ($p\bar{p} \to t\bar{t} \to l^{\pm}\nu jj'b\bar{b}$) sample of $t\bar{t}$ candidate events. The first step in the measurement involves selecting a pure sample of $t\bar{t}$ events in data in the ℓ+jets channel. Events with an isolated high p_T ($> 20\ GeV$) e or μ accompanied by four or more high p_T ($> 15\ GeV$) jets are considered for the analysis. Events with W bosons are selected by requiring $\not{E}_T$ > 20 GeV. To remove the multijet background, $\not{E}_T$ is required to be acollinear with the lepton direction in the transverse plane. The purity of the sample is significantly enhanced by requiring at least two jets in the event to have a secondary vertex b-tag. In the resulting sample of 21 candidate events, $Wb\bar{b}$ production is the largest background and represents ≈5% of the sample.

Each selected $t\bar{t}$ event has two "legs", one with a leptonically decaying W_l ($t \to Wb \to l\nu b_l$) and one with a hadronically decaying W_h ($t \to Wb \to q\bar{q}'b_h$). The second step in the analysis consists in assigning the correct jets and leptons to the correct "leg" of the event, uniquely specifying which b-jet comes from the same top (or anti-top) quark as the lepton. A constrained kinematic fit is performed for this purpose. The four highest p_T jets can be assigned to the set of final state quarks according to many permutations and there are at least two ways to assign the $b-$jets to b_l and b_h. For each permutation, the measured four vectors of the jets and leptons are fitted to the $t\bar{t}$ event hypothesis and the b_l and b_h jets are identified by selecting the permutation with the highest probability of arising from a $t\bar{t}$ event. For 16 of the 21 selected events, the kinematic fit converges leading to correct assignment, thus providing 32 measurements of q_t since top quark charge is measured twice in each event. In each $t\bar{t}$ event, the observable $|q_t|$ is computed, which is the

sum of the lepton charge from the W-boson decay and the charge of b_l. The $b-$jet charge is determined by taking a p_T-weighted sum of the charges of the tracks with $p_T > 0.5\ GeV$ contained within a cone of ΔR =0.5 around the $b-$jet's axis and thus one can distinguish between the b and $\bar{b}$ on a statistical basis. The performance of this jet charge algorithm is calibrated using an independent dijet data sample enriched with semileptonic b quark decays. In the calibration sample, the charge of the $b-$jets is derived from the lepton charge, accounting for $c-$jet contamination and B oscillation corrections. The performance of the algorithm is also calculated as a function of the p_T and η of the jet, so that kinematic differences between the control sample and the $t\bar{t}$ are accounted for.

The subsequent step is to use the expected shapes of jet charge for b-jet and $\bar{b}$-jet in data to derive the expected shape of $|q|$ for the SM ($q_t = +2/3$) and the exotic ($q_t = -4/3$) scenario. The resulting SM and exotic templates, normalized to unity, are used as probability density functions, $p^{\rm sm}$ and $p^{\rm ex}$, respectively, in the C.L. calculation. Figure. 44 compares the charge distribution of the top quark candidates reconstructed in data with +2/3 and -4/3 charge hypotheses.

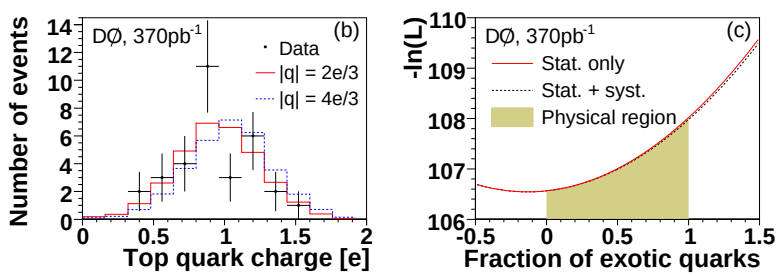

Fig. 44. The 32 measured values of the top quark charge (binned) compared to the Standard Model and exotic scenario templates (left)[176]. Likelihood fit of the fraction of exotic quark pairs in the selected data sample (right)[176].

A likelihood ratio defined as

$$\Lambda = \frac{\prod_i p^{\rm sm}(q_i)}{\prod_i p^{\rm ex}(q_i)} \tag{27}$$

is then computed to determine the most probable model where the numerator (denominator) measures the likelihood of the observed set of charges q_i arising from a SM top quark (exotic quark). The subscript i runs over all 32 available measurements. The value of the $\Lambda^{\rm data}$ measured in data is compared with the expected $\Lambda^{\rm sm}$ and $\Lambda^{\rm ex}$ distributions derived by performing ensemble tests using the SM and exotic scenarios respectively. The observed set of charges is found to agree well with those of a SM top quark. For the exotic heavy quark hypothesis, only 7.8% of the pseudo-experiments give a higher Λ ratio than the one measured in data. Therefore, DØ

yields a $p-$value, corresponding to the probability of consistency with the exotic model, of 7.8%. The top quark is indeed consistent with being the SM $|q_t|$ =2/3 quark. Figure 44 shows the fraction of exotic quark pairs (ρ) in the data obtained by performing an unbinned maximum likelihood fit to the observed set of q_i which yields $0 \leq \rho <0.52$ at the 68% $C.L$ and $0 \leq \rho <0.80$ at the 90% $C.L$.

8. Searches for Non-Standard Top Quark Production and Decay

Several alternative models predict substantially different production and decay mechanisms for the top quark than were described in Section 2. For instance, the possibility to detect a heavy resonance which decays to $t\bar{t}$ is testable using elements of the techniques for kinematic reconstruction. The final states are sensitive to alternative decay chains from the top quark, such as thru a charged Higgs or W' boson. This section will review the experimental efforts in these directions.

8.1. $t\bar{t}$ *resonance search*

It may be that the top quark is a special member of the fermion family. Its large mass has provoked suspicion that it may have a unique and significant role to play in electroweak symmetry breaking. Topcolor models[177,44] suggest that there are new strong interactions which can generate the large top quark mass while leaving other quarks light. This interaction results in a massive $t\bar{t}$ condensate, sometimes termed Z'. Technicolor[178], on the other hand, posits interactions at the electroweak scale which provide electroweak symmetry breaking without the need for a scalar Higgs field. In the extended models, this gives masses to all fermions. However, the generated value of m_t is too small. The top-color assisted technicolor[177,44] model combines these approaches to predict the correct m_t. Variants of this approach predict a Z' which couples preferentially to third generation fermions and has no couplings to leptons.

8.1.1. *General Methods*

Efforts to look for a $t\bar{t}$ resonance have employed the ℓ+jets final state. In such events, a full kinematic reconstruction is performed as in the mass analyses described in Section 6.4, with the exception that m_t is either held fixed or within a window determined by uncertainty on the mass. All jet combinations and neutrino solutions are tried. The chosen combination is one that minimizes the χ^2, given the known errors and measured parameters of the event. The combinatorics of jet assignment mean that this choice is not always the correct one, although $b-$tagging can enhance the probability. Generally, a cut on the χ^2 is applied to further reduce backgrounds. The solution for each event permits the calculation of the apparent $t\bar{t}$ invariant mass, $M_{t\bar{t}}$, from that event.

A narrow resonance with $\Gamma_{Z'} = 0.012 M_{Z'}$ is the standard assumption for the signal. Generally, this width is substantially less than the resolution inherent in the experimental measurements, so natural widths up to a few percent may still be accomodated. However, this assumption does mean that any results are not

strictly applicable to some models, such as Kaluza-Klein scenarios. The primary backgrounds to the search are standard $t\bar{t}$ production, W+jets and QCD multijet production. Single top quark and diboson events give small but non-negligible contributions. Evidence of resonant production is sought by fitting the expected $M_{t\bar{t}}$ resonance plus the expected $t\bar{t}$ and backgrounds to the observed spectrum in data. A limit on any anomalous production cross section results on a limit on the mass of the resonant state.

8.1.2. *DØ Searches*

In 2004, DØ published a search for $t\bar{t}$ resonance in Run I data[180]. A sample of 41 ℓ+jets events, 4 with soft $\mu-$tag selection. were used for the analysis. The resonance signal was modeled with PYTHIA in a mass range of 400 GeV $< M_{Z'} <$ 850 GeV. The CTEQ3M *pdf* was used. The $t\bar{t}$ background was simulated using HERWIG. The W+jets background was modeled with VECBOS, and HERWIG was used for the parton shower simulation. The instrumental background from multijet production was derived from a data sample in which actual leptons have been rejected. No evidence for resonant production was observed. A Bayesian fit [181] was performed which considered three components separately: signal ($Z' \to t\bar{t}$), standard $t\bar{t}$ production, and $W + jets$ and multijet events. The latter element had W and QCD fractions set from the template mass analysis. The resulting limit is $M_{Z'} > 560$ GeV/c^2 at 95% C.L..

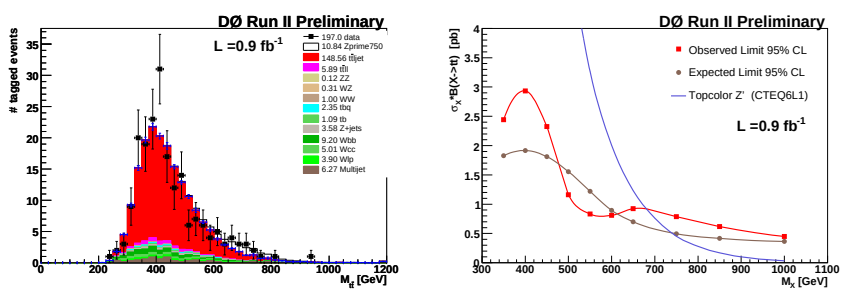

Fig. 45. Distribution of $t\bar{t}$ invariant mass, $M_{t\bar{t}}$, from DØ Run II data (left) [183]. Expected and observed limits, with comparison to the Z' estimation is also shown (right).

Two preliminary studies have been executed in Run II using template methods for kinematic reconstruction. A mass range 350 GeV/c^2 $< M_{Z'} <$900 GeV/c^2 was considered in both analyses. The first search used 370 pb^{-1} of ℓ+jets events tagged with a secondary vertex tagger. Signal Monte Carlo samples were generated using PYTHIA. Studies indicated that the choice of jet-to-parton configuration was correct about 65% of the time after the χ^2 cut. The $t\bar{t}$ and W+jets backgrounds were generated using ALPGEN plus PYTHIA. The QCD background was estimated

via matrix method in the data. The data yielded 108 events which showed no evidence of a resonance. A Bayesian approach was used to extract a limit. Kinematic shape uncertainties arose from jet energy calibration and efficiency and the knowledge of the kinematic dependence of the $b-$tag and mis-tag rates. Normalization uncertainties came from theoretical uncertainty in the $t\bar{t}$ cross section as well as the integrated luminosity. Correlations among uncertainties were included in the fit. A limit of $M_{Z'} < 680$ GeV/c^2 was obtained at 95% C.L. [182]. A further study has been performed with 197 ℓ+jets events obtained from 900 pb^{-1} of data. These events were tagged with a neural network tagger. In this sample, 154 events were expected from standard $t\bar{t}$ process. Much of this analysis is similar to the 370 pb^{-1} analysis. A limit of $M_{Z'} > 680$ GeV/c^2 was obtained [183]. Results are shown in Fig. 45.

8.1.3. *CDF Searches*

An initial search for the $t\bar{t}$ resonance was conducted by the CDF collaboration using Run I data [179]. One of the leading three jets in each event were required to be $b-$tagged with a secondary vertex. VECBOS was used to model W+jets events. PYTHIA was used to model the signal as $Z' \to t\bar{t}$. In order to improve the reconstructed mass resolution of the $t\bar{t}$ system, the requirement on the computed top quark masses was relaxed to fall in the range 150 GeV to 200 GeV. This allowed a more efficient acceptance of combinations with correct jet-parton assignments. Twenty events were removed out of the initial sample of 83 because they yielded a poor minimum χ^2. No evidence of a resonance was observed in the data. A binned likelihood fit of the data to signal and background was performed to extract a limit on the resonance production rate. Masses from 400 GeV to one TeV were scanned. The primary sources of systematic uncertainty were from signal and background shapes, and jet-related systematics such as energy scale and gluon radiation. Uncertainties were incorporated into the limit calculation as Gaussian uncertainties. The 95% C.L. upper limit for $\Gamma_{Z'} = 0.012 M_{Z'}$ is $M_{Z'} > 480$ GeV.

CDF has improved upon this result by looking at 680 pb^{-1} of Run II data [184]. The signal and standard $t\bar{t}$ production were modeled with PYTHIA. Multijet background came from data and W+jets events were modeled with ALPGEN plus HERWIG. The top quark and boson pair processes were normalized based on the theoretical cross sections and the estimated luminosity to be 199 and 14 events, respectively. The QCD and W+jets backgrounds were then taken as the remaining contribution to the event yield observed in data: 450 events. The QCD/W ratio was fixed at 10% as taken from the cross section measurement [86]. Event reconstruction was done via matrix element fit using resolution functions for the jets. All possible jet configurations were summed over in this approach, and a probability distribution vs. $m_{t\bar{t}}$ was obtained. Simulations showed that the mean of this distribution was best correlated with the actual resonance mass. The mass resolution was set by the jet energy calibration and the unknown p_z of the neutrino. Incorrect jet assignments

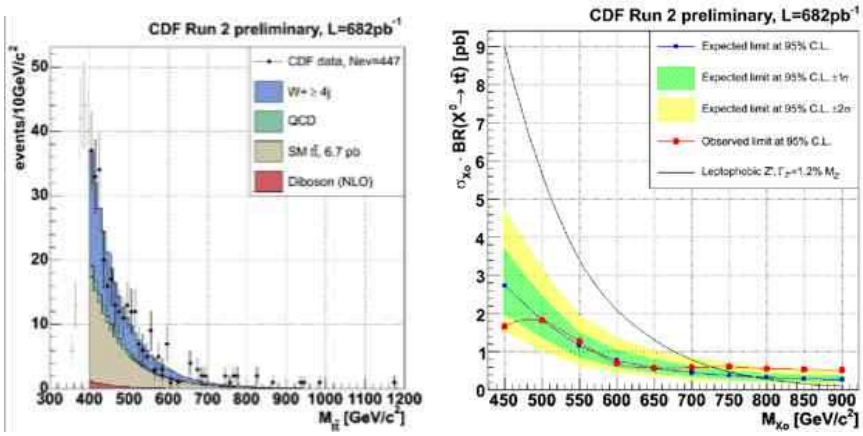

Fig. 46. Distribution of $t\bar{t}$ invariant mass, $M_{t\bar{t}}$, from CDF Run II data (left) [184]. Expected and observed limits, with comparison to the Z' estimation is also shown (right).

also produced a significant low mass tail. No evidence for an excess over standard expectations was observed. The presence of a resonance would be detected by a likelihood calculation based on the distributions $< m_{t\bar{t}} >$ for signal of varying masses and the backgrounds. Systematic uncertainties were extracted by varying the jet energy scale, initial and final state radiation, and the Q^2 for W+jets production by $\pm 1\sigma$ and generating these mass distributions for use in the likelihood fit. A limit of $M_{Z'} < 725$ GeV/c^2 at 95% C.L. was extracted from the data (see Fig. 46). More recently, CDF has analyzed 955 pb^{-1} of data using a template fitting method. A limit of $M_{Z'} < 720$ GeV/c^2 was obtained [185].

8.2. *Charged Higgs decays*

8.2.1. *Two Higgs Doublet Models*

In the electroweak model, the generation of mass is governed by one scalar Higgs doublet manifesting in one observable particle, the Higgs boson. The peculiar problems associated with the Higgs mechanism have led to several efforts to produce models with extended Higgs sectors. The simplest configuration has two Higgs doublets and this is included in several scenarios, including supersymmetry (SUSY). Two types of model exist. Type I models have only one doublet coupling to fermions. Type II models, however, posit one doublet which couples to up-type fermions including charged leptons, and another doublet that couples only to down-type fermions. In the MSSM [126], the Type II case holds. Five physical particles are predicted: two neutral scalars (h^0, H^0), a neutral pseudoscalar (A^0), and two charged scalars ($H^{\pm}$).

Evidence of the existence of the charged Higgs has been sought in e^+e^- collisions[160]. Indirect searches from CLEO provide the constraint $m_H > [244 +$

$63/(\tan\beta)^{1/3}]$ GeV at the 95% C.L.[186], where $\tan\beta$ is the ratio of vacuum expectation values of the two Higgs doublets. Observed $\tau \to \nu_\tau K$ and $K \to \nu_l(\gamma)$ branching ratios provide a limit of 0.21 GeV^{-1} $> \tan\beta/m_H$ at 90 % C.L.[187]. These limits are stricter than those quoted for the Tevatron searches below, but are more theory dependent. The direct search for $H^\pm$ at LEP, however, provides a hard limit of $m_H > 78.6$ GeV[188]. The Tevatron searches consider potential physics beyond this limit.

8.2.2. *Production and Decay*

Single charged Higgs production would have negligible cross section at the Tevatron. Weak pair production of charged Higgses is calculated to have a cross section of 0.1 pb. However, a large enhancement occurs when they are generated through the production and decay of top quark pairs. Then the Higgs pair production rate is potentially as high as the 6.7 pb $t\bar{t}$ cross section. Additionally, the top quark decay produces associated $b-$jets which allows a further background reduction relative to direct diboson production.

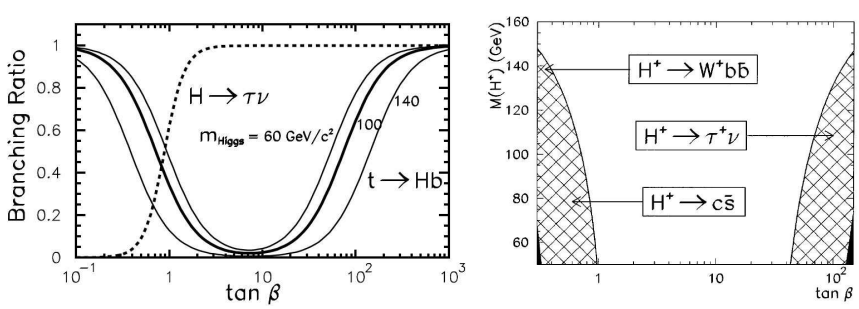

Fig. 47. At left is shown the dependence of $BR(H \to \tau\nu)$ and $BR(t \to Hb)$ on $\tan\beta$. Coverage in the m_H vs $\tan\beta$ plane is shown at right when $BR(t \to Hb) > 0.5$ (cross-hatched) and 0.9 (solid). Regions where specific final states dominate are indicated.

If the $H^\pm$ are lighter than the top quark, then the decay $t \to Hb$ can compete with the standard $t \to Wb$ decay. In particular, $BR(t \to Hb) = m_t^2 \cot^2\beta + m_b^2 \tan^2\beta + 4m_t^2 m_b^2$ is significant when $\tan\beta$ is either very large or very small (see Fig. 47). Figure 47 also indicates that this branching ratio declines as m_H increases. There are then three top quark decay modes to consider: $t\bar{t} \to HHb\bar{b}$, $HWb\bar{b}$, and $WWb\bar{b}$. The final states are dictated by the H and W decays, and the analyses all assume fermionic decays for the charged Higgs.

In the Type II models, $H^\pm$ decays are expected to be quite different than the normal W boson decays. Its decay branching ratios are dependent on m_t, M_H and $\tan\beta$. For values of $\tan\beta > 2$, the $H \to \tau\bar{\nu}$ decay dominates and grows to 100% when $\tan\beta > 5$, as shown in Fig. 47. The τ is identified explicitly only through

its hadronic decays to a narrow jet, as described in Section 3.2. For smaller $\tan\beta$ values, the $H \to c\bar{s}$ decay is primary and leads to two quark jets in the final state. However, when $M_H > 130$ GeV the decay chain $H \to tb \to Wb\bar{b}$ exceeds this mode. The dominance of the $H \to \tau\bar{\nu}$ or $c\bar{s}$ modes have led to two different search strategies for low and high $\tan\beta$ regions.

8.2.3. *High* $\tan\beta$ *Searches*

The more direct searches attempt to identify the presence of the $H^{\pm}$ explicitly from the presence of the τ in a selected top quark event sample. These searches have the benefit that they can avoid some dependencies on theoretical calculations, since they measure the actual rate of τ production. In general, an assumption is made that $BR(H \to \tau\nu) \sim 100\%$. CDF conducted such a search in Run I data [189] using $\not{E}_T$ triggers. Two event topologies were explored for this analysis. One searched for events possessing a $\tau + l(= e, \mu, \tau) + \not{E}_T +$ two jets where one of the jets had to be tagged as coming from a $b-$quark. The other topology exhibited two τ jets that were not azimuthally back-to-back. It was employed to account for the case where M_H approached m_t and the $b-$jets were too soft to be reconstructed. Instrumental backgrounds from fake τ jets are dominant. They are modeled from the data by folding a $jet \to \tau$ fake rate into the multijet $+\not{E}_T$ sample. W and Z boson production was modeled using VECBOS and normalized to the measured cross sections in data. Standard $t\bar{t}$ backgrounds were also determined to be significant. The total background estimation was 7.4 ± 2.0 events and seven events were observed. To extract a limit on $H^{\pm}$ production, the polarization of the τ's should be considered because it affects the ν angles and produces larger $\not{E}_T$. ISAJET was modified to account for this and expected signal efficiencies were extracted. For high $\tan\beta$ (i.e. > 100), the region $M_H < 147$ GeV was excluded at 95% C.L..

Theoretical progress led to the realization that higher order radiative corrections impact branching ratio calculations in the high $\tan\beta$ region[190,191]. This means that limits in the $\tan\beta$ vs. M_H plane depend on model parameters. CDF incorporated this into their analysis of $\ell + \tau$ events in Run I[192]. Both tracking-centric and calorimeter-centric τ identification schemes were used. The explicit identification of jets by $b-$tagging was not implemented in this analysis. The primary backgrounds were Z and W boson production in association with jets. $t\bar{t}$ also provided a significant contribution. This was estimated by anchoring the expected event yield to CDF's measurement of $\sigma_{t\bar{t}} = 5.1$ pb in the ℓ+jets channel. The total background was estimated to be 3.1 ± 0.5 events, and four events were observed. By considering the observed data and the estimated backgrounds and their uncertainties, a limit was determined for $BR(t \to Hb)$. Acceptance for WW, WH and HH modes was calculated using PYTHIA with $m_t = 175$ GeV. TAUOLA was used to provide the correct polarization of the τ. Higgs masses from $60/c^2$ to 160 GeV$/c^2$ were scanned, and a limit of $BR(t \to Hb) < 0.5$ or 0.6 in the range 60 GeV $< M_H < 160$ GeV was obtained. In the MSSM at very high $\tan\beta$, this limit is not valid because the

relevant Yukawa coupling is non-perturbative.

A direct search was also pursued in 2002 using 62.2 ± 3.1 pb^{-1} by DØ[193]. Events comprised of $\tau + \not\!\!E_T + jets$ and possessing a spherical distribution to the object E_T's were selected. A neural network (NN) based on JETNET[194] incorporated the $\not\!\!E_T$ and two eigenvalues of the normalized momentum tensor to discriminate signal and background. The NN was trained on signal generated with ISAJET with forced decays of $H \to \tau\nu$ and $\tau \to hadrons$. The Higgs mass was taken as 95 GeV since it only weakly affected the NN performance. The top quark production cross section was taken as 5.5 pb. The instrumental background was modeled using multijet events from data. W+jets events were modeled using VECBOS plus ISAJET for soft QCD evolution. A total of 5.2 ± 1.6 events were expected from background and standard top quark processes, while three events were observed in data. The probability for the number of expected events to fluctuate to the number observed was calculated for individual choices of $\tan\beta$ and m_H. Systematic uncertainties for jet energy scale uncertainty, signal modeling and τ identification were the main sources considered. Values of $\tan\beta > 32.0$ were excluded at 95% C.L. for $m_H = 75$ GeV. The result is shown in Fig. 48.

8.2.4. *Low* $\tan\beta$ *Region and General Searches*

As already noted, the unique signature from Higgs $\to \tau$ jets is confined to the high $\tan\beta$ region. However, at low $\tan\beta$, it is also possible for substantial numbers of top quarks to decay to charged Higgses. The Higgs decays to $c\bar{s}$ in this region are less distinctive than in the previous cases. A search incorporating the low $\tan\beta$ region was first performed on 109.2 pb^{-1} by DØ in Run I. They employed a technique to look for the disappearance of SM top quarks[195] and used the selections for the standard ℓ+jets channels, both topological and soft μ tagged, in the $t\bar{t}$ production analysis[74]. This strategy has the advantage of incorporating the $c\bar{s}$ decays into the search. However, at high $M_H > 130$ and $\tan\beta < 2$, the Higgs boson will preferentially decay via a virtual top quark to $Wb\bar{b}$. This gives a final state that is not different enough from standard top quarks, so the search is insensitive in this region. Since the presence of non-standard top quark decays would affect the measurement of the top quark production cross section, the theoretical value of 5.5 pb at 1.8 TeV was used and assumed to be unaffected by the presence of the new Higgs sector. Also, studies indicated that the non-standard decays would not affect the existing measured top quark mass by more than five percent, so $m_t = 175$ GeV was used for the analysis. ISAJET was used to calculate signal efficiencies and was modified to properly account for $Wb\bar{b}$ final states. PYTHIA was also modified to provide a cross-check. Because the selection was the same as used for the cross section measurements, those existing background estimates were valid. The estimated background plus $t \to Wb$ signatures provide 30.9 ± 4.0 events compared to 30 events observed in data. Efficiencies were calculated for different m_H's from the Monte Carlo to extract the sensitivity at different points in the $(m_H, \tan\beta)$ plane.

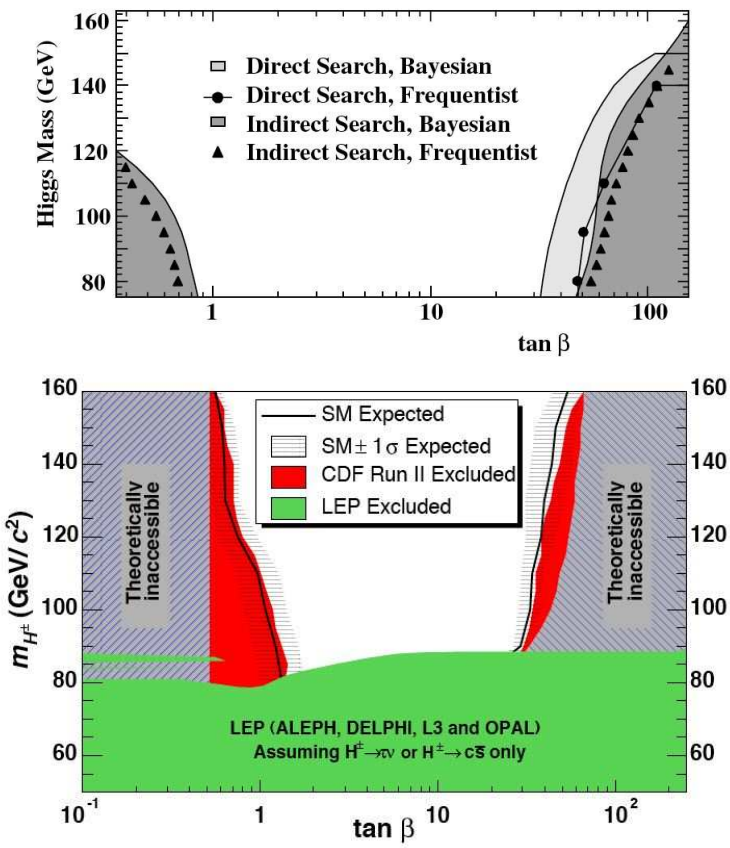

Fig. 48. DØ Run I limits [195] in the M_H vs. $\tan\beta$ plane incorporating direct and indirect searches (top). CDF Run II limits [196] using radiative corrections are shown at bottom. In the absence of these corrections, the CDF results would be the most stringent experimental limits.

Leading order theoretical calculations of branching ratios were used to calculate the probability to observe the charged Higgs decays. Primary systematic uncertainties were jet energy scale, signal model and particle identification. At 95% C.L., most of the points giving a $BR(t \to Hb) > 0.45$ were excluded. Combining this analysis with the direct limit from DØ gives a branching ratio limit of $BR(t \to Hb) < 0.36$ at 95% C.L. for $0.3 < \tan\beta < 150$ and $m_H < 160$ GeV (see Fig. 48).

Since this analysis, it was realized that $H^\pm \to Wh^0$ can be significant. CDF has incorporated this element, along with the developments described for their earlier analyses, into the first search for charged Higgs bosons in Run II[196]. Using 193 pb^{-1}, the yield of events in four categories of final state were compared: dilepton, ℓ+jets with $b-$tag, ℓ+jets with at least two $b-$tags, and $\ell+\tau$ events. The latter was compared to the other channels to produce direct limits on the presence of charged Higgs bosons in top quark decay. This analysis was the first to use the newer Yukawa

Table 13. Limits by DØ [195] and CDF[196] in high $\tan\beta$ region for charged Higgs branching fraction.

Experiment	Lumi. (pb^{-1})	$BR(t \to Hb) <$ @ 95%$C.L.$
DØ	66.2 and 109.2	0.36
CDF	193	0.4

coupling and radiative corrections[190,191] in the determination of acceptances for the sensitivity calculation. The analysis considered decays of the Higgs to $\tau\nu, c\bar{s}, t^*\bar{b}$, and $Wh^0 \to Wb\bar{b}$. PYTHIA was modified to include the $t^*\bar{b}$ decay mode and used to estimate the efficiencies for various top quark widths, the charged Higgs mass and width, and m_{h^0}. In order to properly calculate the overall acceptance for various parameter choices in MSSM, the CPSuperH[197] generator was used. Much of the low $\tan\beta$ region was excluded, including some of the high m_H region. In the high $\tan\beta$ region, a limit of $BR(t \to Hb) < 0.4$ at 95% was obtained, as shown in Fig. 48. If no assumptions are made for charged Higgs decay (i.e. $H \to \tau\nu$), the limit is relaxed to < 0.91. For comparison (see Table 13), these limits would be stricter than the previous DØ limits if the radiative corrections were ignored.

8.3. *W′ in Top quark decays*

The existence of new forces in nature can be revealed through the observation of additional gauge bosons beyond those of the standard model. Various extensions of the SM postulate larger gauge groups[32,198] and therefore new forces associated with additional charged gauge bosons, which are generically called W'. For instance, the left-right symmetric model[85] expands the $SU(2)_L \times U(1)$ electroweak group to $SU(2)_L \times SU(2)_R \times U(1)$, predicting the existence of three new gauge bosons: two charged $W'^{\pm}$ bosons and one neutral Z' boson. In this model, the W' boson appears as a heavier counterpart of the left-handed W and is responsible for right-handed interactions, in the same way as the SM W boson mediates only left-handed interactions.

Previous indirect searches based on low energy phenomena such as μ decay, the $K_L - K_S$ mass difference, neutrinoless atomic double beta decay, and semileptonic branching ratio $b \to Xl\nu$ have resulted in stringent model-dependent limits[199]. Direct searches for the production of W' bosons have focused on its leptonic decays, $W' \to l\nu_l$, by looking for anomalous production of high transverse mass $l\nu_l$ pairs. Searches using the decay mode $W' \to e\nu_e$[200,201] ($W' \to \mu\nu_\mu$[202]) from Tevatron Run I exclude a W' boson with mass $m_{W'} < 754$ GeV (660 GeV) at 95% C.L.. The combination of these leptonic channels yields the lower limit on $m_{W'}$ of 786 GeV at 95% C.L.[200]. These mass limits all assume that the new vector boson's couplings to leptons are those given by the SM, with the additional assumption that the neutrino produced is much lighter than the W' boson. Searches for the

W' boson in the quark decay channel $W' \to q\bar{q}'$ based on resonant structure in the dijet mass spectrum have also placed strong constraints on its mass. Searching in the hadronic final state avoids assumptions regarding the neutrino mass m_ν, but is background limited. Previous direct searches in this channel have ruled out W' bosons in the mass range 1< $m_{W'}$ <261 GeV by UA2[203], 300< $m_{W'}$ <420 GeV by CDF[204] and 300< $m_{W'}$ <800 GeV by DØ [205] at 95% C.L..

8.3.1. *W' in Top quark sector*

The top quark sector offers great potential for the search of new gauge bosons. The single top quark final state is especially sensitive to the presence of an additional heavy boson, owing to the decay chain $W' \to t\bar{b}$, where the top quark decays to a b-quark and a W boson which subsequently decays leptonically or hadronically. The leading order Feynman diagram for W' boson production resulting in single top quark events is shown in Fig. 49.

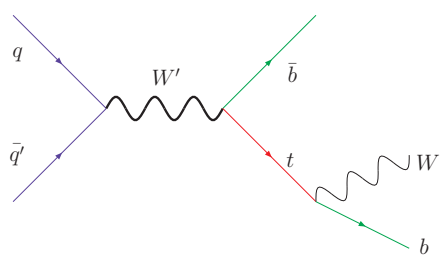

Fig. 49. Leading order Feynman diagram for single top quark production via a heavy W' boson. The top quark decays to a standard model W boson and a b-quark.

This diagram is identical to that of the SM s-channel single top quark production where the SM W boson appears as a virtual particle. The W' boson also has a $t-$channel exchange that leads to the single top quark final state. However, the cross section for a $t-$channel W' process is much smaller than the SM $t-$channel single top quark production due to the high mass of the W' boson. A heavy W' boson signal would appear as a peak in the $t\bar{b}$ invariant mass distribution in these processes. Although this search is only sensitive to W' bosons with mass above the $t\bar{b}$ kinematic threshold of approximately 180 GeV, it is relatively free of background compared to the $W' \to q\bar{q}'$ decay mode because of the distinct signature from the top quark decay $t \to Wb$. Furthermore, the interpretation of the data is less sensitive to assumptions regarding the right-handed neutrino (ν_R) sector or the lepton couplings of the W' boson.

8.3.2. *Run I search for $W' \to t\bar{b}$*

CDF attempted the first search for a W' boson decaying to a $t\bar{b}$ final state using a 106 pb^{-1} of Run I data sample[206]. The analysis considers the ℓ+jets final state topology of single top quark production arising from leptonic decays of W boson, $W \to e\nu, \mu\nu$. The event signature consists of a high-p_T lepton, significant $\not\!\!E_T$ from the neutrino, and two b-quark jets. The candidate events are selected by requiring a high-p_T electron or muon with large $\not\!\!E_T$ and accompanied by two or three jets, at least one of them being b-tagged. The fully simulated PYTHIA Monte Carlo was used to determine the expected contribution from signal events in the data sample as a function of W' mass. The W' boson is required to have a right-handed coupling to the $t\bar{b}$ final state since negligible signal yield differences between right-handed and left-handed couplings are expected. The analysis considered both the cases when $m_{W'} < m_{\nu_R}$ and $m_{W'} \gg m_{\nu_R}$, where m_{ν_R} is the mass of ν_R that couples to the W'. The analysis attempted to interpret the data for $m_{W'}$ >225 GeV since the acceptance calculation becomes increasingly uncertain as one nears the $t\bar{b}$ kinematic threshold. The dominant background contributions to this search arises from the pair production of top quarks, single top quark production, and the associated production of W bosons with one or more heavy quarks ($Wb\bar{b}$, $Wc\bar{c}$) which provides the largest single background contribution. A candidate sample of 57 events agreed reasonably with the 48±6 expected from background. Therefore, no significant evidence for W' boson production is seen.

In such a scenario, the analysis sets a limit on the W' production cross section times branching ratio, $\sigma \times BR(p\bar{p} \to W' \to t\bar{b})$, employing the invariant mass distribution of the $Wb\bar{b}$ final state. The $Wb\bar{b}$ mass distribution for the 57 candidate event sample is shown in Fig. 50 and is compared with the expected mass distribution for a W' boson with $m_{W'}$=500 GeV and the sum of the background processes. To estimate the size of a potential signal contribution, an unbinned maximum likelihood fit is performed to the observed mass distribution, allowing for both a signal and background contribution for different values of $m_{W'}$ ranging from 225 to 600 GeV. Based on the fit results for the fraction of events arising from W' production, the analysis sets 95 % C.L. upper limits using a Bayesian technique on the relative contribution of a W' boson for each value of $m_{W'}$, $\sigma \times BR(W' \to t\bar{b})/\sigma \times BR(W' \to t\bar{b})_{SM}$, where the denominator is the expected $\sigma \times B$ for a given W' boson mass assuming SM couplings. Figure 50 shows the upper limits on the W' boson production cross section as a function of the $m_{W'}$ for the two different assumptions on m_{ν_R}. This analysis excludes a W' boson at 95 % C.L. with masses $225 < m_{W'} <$536 GeV for $m_{W'} \gg m_{\nu_R}$ and $225 < m_{W'} <$566 GeV assuming $m_{W'} < m_{\nu_R}$.

8.3.3. *Run II search for $W' \to t\bar{b}$*

In Run II, DØ has conducted a comprehensive search for the W' boson in the top quark decay channel by analyzing 230 pb^{-1} of data[207]. The search considers three

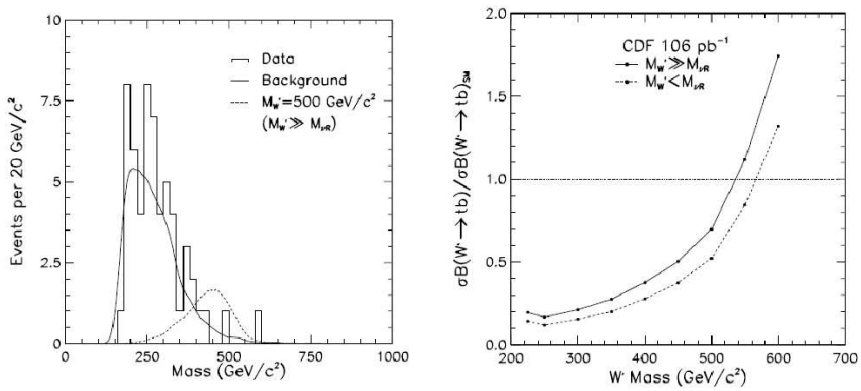

Fig. 50. CDF's Run I serach for W' boson in top quark decays[206]. **Left**: The $Wb\bar{b}$ mass spectrum of the candidate events after constraining the lepton-neutrino invariant mass to the W boson mass. The distribution expected from the production of a W' boson with a mass of 500 GeV is illustrated by the dashed curve. The distribution expected from the background processes is shown by the solid curve. **Right**: The upper limits on the W' boson production cross section as a function of the W' boson mass. Limits are shown for the case $m_{W'} \gg M_{\nu_R}$ (solid) and $m_{W'} < M_{\nu_R}$ (dashed). The intercepts at $[\sigma.BR(W' \to t\bar{b})/\sigma.BR(W' \to t\bar{b})_{SM}]$=1 correspond to the 95% C.L. limits on the W' boson mass with SM strength couplings.

models of W' boson production. In each case, the CKM mixing matrix elements for the W' boson is set to the SM values. The first model (W'_L) assumes the coupling of the W' boson to SM fermions to be identical to that of the SM W boson. Under these assumptions, there is interference between the SM s-channel single top quark process and the W' boson production process, although this interference term is small for large W' boson masses. In the second and third model (W'_R), the W' boson has only right-handed interactions. In the second model, the W'_R boson is allowed to decay both to leptons and quarks, whereas in the third model it is only allowed to decay to quarks. The branching fraction for the decay $W' \to t\bar{b}$ is about 3/12 when the decays to quarks or leptons are both included and is about 3/9 when the decay to leptons is not allowed[198]. COMPHEP 4.4.3 matrix element event generator[69] is used for the modeling of the W' boson production process. Fig. 51 compares the invariant mass distribution for the W' models with left-handed coupling (including interference) and right-handed coupling (no interference) with the SM s-channel single top quark production, for a W' boson mass of 600 GeV.

Table 14 shows the NLO cross sections[198] for a W' boson $\times$ branching fraction to $t\bar{b}$ for three different W' boson models. The systematic uncertainty on the cross section varies between about 12% at a mass of 600 GeV and 18% at a mass of 800 GeV. The theoretical W' boson production cross section is more than 15 pb for masses between 200 and 400 GeV for all three models[198]. The upper limits on the single top quark production cross section in the s-channel were 6.4 pb by DØ based on the analysis of same dataset[115] and 13.6 pb by CDF[114], which do not depend

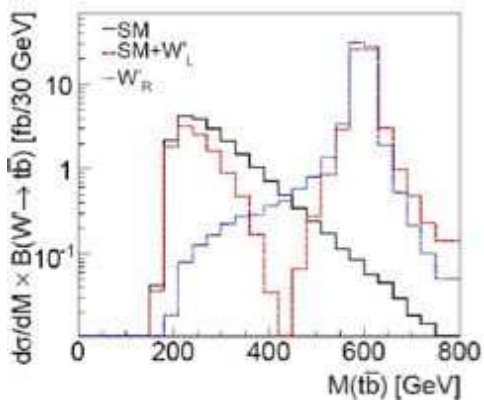

Fig. 51. The invariant mass of the top-bottom quark system at the parton level for different models of W' boson production[207]. Shown are the SM s-channel distribution, the $W'_L \to t\bar{b}$ boson distribution, including the interference with the SM contribution, and the $W'_R \to t\bar{b}$ boson contribution, for a W' boson mass of 600 GeV.

much on whether the W' boson coupling is left-handed or right-handed. Thus, the W' boson production decaying to $t\bar{b}$ is excluded in this mass region and the analysis explores the region of even higher masses for W' searches.

Table 14. NLO production cross section for a W' boson $\times$ branching fraction to $t\bar{b}$ for three different W' boson models[198]. The production cross section for W'_L interactions also include the SM s-channel contribution as well as the interference term between the two.

	Cross section $\times$ $BR(W' \to t\bar{b}$ [pb]		
W' mass [GeV]	SM+W'_L	$W'_R(\to l \; or \; q)$	$W'_R(\to q)$ only
600	2.17	2.10	2.79
650	1.43	1.25	1.65
700	1.03	0.74	0.97
750	0.76	0.44	0.57
800	0.65	0.26	0.34

This search adopts a strategy similar to that used in CDF's Run I analysis, i.e. looks for events that are consistent with $W' \to t\bar{b}$ production and the W boson from the top quark decaying leptonically ($W \to e\nu, \mu\nu$; including $W \to \tau\nu$ with $\tau \to e\nu$). It utilizes the same dataset, basic event selection, and background modeling as the DØ single top quark search described in Section 5.1, and Ref. 115. It selects signal-like events and separates the data into independent analysis sets based on final-state lepton flavor (electron or muon) with two or three jets and b-tag multiplicity, single tagged or double tagged. The independent datasets are later combined in the final statistical analysis.

The large mass of the W' boson is expected to set it apart from all background processes, hence a complete kinematic reconstruction of the invariant mass of the W' boson is performed by adding the four-vectors of all reconstructed final state objects: the jets, the lepton, and the neutrino. Figure 52 shows the distribution of effective mass of $\ell + \not{E}_T$ + jets when the $\ell\nu$ invariant mass is constrained to the W boson mass. The data, sum of background, and expected W' boson contributions are shown for different couplings and masses. The observed event yield is consistent with the background predictions within uncertainties. The dominant sources of systematic uncertainty on the signal and background acceptances arises from the modeling of b hadrons in the simulation, the jet energy scale, object identification and trigger efficiencies, and modeling of jet fragmentation.

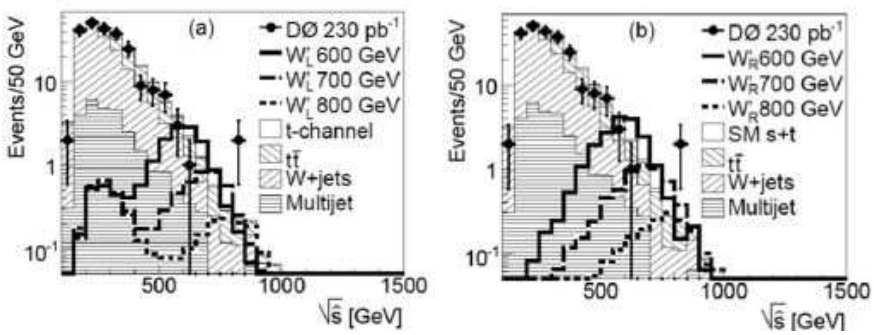

Fig. 52. DØ 's Run II search for W' boson in top quark decays[207]. The distribution of W' boson invariant mass for several values of W' boson mass and background processes for (a) left-handed W' boson couplings, and (b) right-handed couplings when only the decay to quarks is allowed. Electron, muon, single-tagged and double-tagged events are combined.

In the absence of a significant excess over the background predictions, a binned likelihood analysis is performed on the observed invariant mass distribution to obtain upper limits on the $\sigma \times BR(p\bar{p} \to W' \to t\bar{b})$ for discrete W' mass points in each model. Figure 53 shows the $\sigma \times BR(p\bar{p} \to W' \to t\bar{b})$ limits together with the NLO cross sections and the expected limits, along with their uncertainties. At the 95% C.L., the shaded areas above the solid lines are excluded in this analysis. The intersection of the solid line with the lower edge of the uncertainty band on the predicted cross section defines the 95% C.L. lower mass limit for each model. Together with the limit from the SM s-channel single top quark search, the presence of a W' boson with SM-like left-handed coupling is excluded if it has a mass between 200 and 610 GeV. In addition, the presence of a W' boson with right-handed couplings that is allowed to decay to leptons and quarks (only quarks) is excluded if it has mass between 200 and 630 GeV (670 GeV). This is the first direct search limit for the W' boson which takes into account interference with the SM properly. It is also the most stringent limit on the presence of a W' boson in top quark decays.

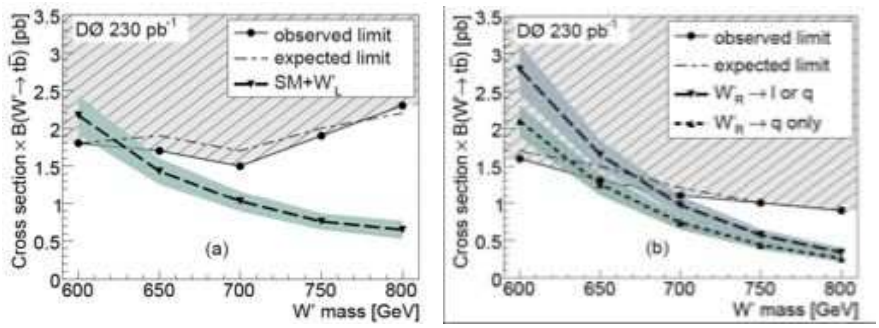

Fig. 53. DØ 's Run II search for W' boson in top quark decays[207]. Cross section times branching fraction limits at the 95% C.L. versus the mass of the W' boson with (a) left-handed couplings and (b) right-handed couplings. Also shown are the NLO cross sections and the expected limits. The shaded regions above the circles are excluded by the measurement.

More recently, CDF has also produced a preliminary result[208] on the search for resonant W' boson which decays via $W' \to t\bar{b}$ using a sample of approximately 1 fb^{-1}. As in the previous analyses, the search looks for unexpected structure in the spectrum of the invariant mass distribution of the reconstructed W boson and two leading jets (M_{Wjj}). Expected contributions from SM processes are derived from selections and background studies of the single top quark analysis. Resonant $t\bar{b}$ production is modeled as simple W' with SM-like couplings to fermions. The analysis finds no evidence for resonant W' production and excludes a W' boson for $m_{W'}$ <760 GeV in the case of $m_{W'} \gg m_{\nu_R}$ and $m_{W'}$ <790 GeV in the case of $m_{W'} < m_{\nu_R}$ at 95% C.L..

9. Prospects for Future Measurements

9.1. *Tevatron synopsis*

The Tevatron program in Run II is currently undergoing rapid progress and measurements of the top quark are greatly improving. We have seen a flowering of techniques for the isolation and study of the top quark. Some approaches pursued in Run I, such as the topological selection of $\ell+$ jets events or the secondary vertex tagging have been adopted by both experiments as useful strategies. New selection mechanisms such as $\ell+$ track in the dilepton case, and b-jet tagging tagging based on neural network discriminant in general have produced competitive results and significantly expand the fraction of top quark events that are analyzable. Attempts to maximize sensitivity for various measurements have generally meant that selections permit significant background yield. This necessitated improvements to background modeling that included increased ability to determine important properties of background in data. An example involves the study of the flavor content of the $b-$tagged backgrounds. Usage of Monte Carlos has been improved by efforts

to more correctly describe jet production.

Substantial increases in integrated luminosity have so far brought the measurement of the $t\bar{t}$ cross section from 30% to $< 15\%$ uncertainties. These measurements are in general agreement with the theoretically predicted value. Many different channel definitions have been tried within the dilepton, $\ell+$ jets and all-jets categories. So far, no serious discrepancies have been observed in the relative rates of these channels. Extensive kinematic tests of the various channels also reveal no clear difference from standard model expectations: production and decay seem well-modeled. The Run II measurements will surpass the 10% level of precision. They are currently systematically dominated and of comparable precision as the theoretical uncertainties. This will hopefully motivate further theoretical work. It will also provide an interesting test when it comes to comparing LHC and Tevatron production.

The major physical significance of m_t has motivated both Tevatron experiments to devote considerable effort to its measurement. Already, Run II has surpassed initial expectations. Improved techniques have been a significant part of this effort. Both experiments have attempted a variety of fitting techniques to exploit the data to the fullest extent. A critical contribution in this regard has been the matrix element approach, which is now being used on all channels. Soon measurements in all channels will be dominated by systematic uncertainties. In Run I, it was clear from the outset that the calibration of jet energies would be a major concern. This still remains the case, and the measurement of top quark properties, particularly the mass, has driven major progress in this area. One of the results of this effort is that we now see the use of the top quark sample as a means to anchor this calibration via the use of jets from $W \to jj$ decays *in situ*. This is a critical transition that will have significant impact on future Tevatron and LHC physics. Currently, the cumulative uncertainty in m_t is 1%, with each experiment achieving 1.5% in their best measurements. This result has been achieved with only a fraction of the expected total Run II luminosity. As energy scale and other uncertainties are further reduced, the measurement will likely become even more precise. Such a measurement will remain competitive with the LHC for some time to come.

An exciting aspect of the field is the rising experimental capability to test electroweak physics through the properties of this particle. With the advent of a signal for single top quark production, a new direct probe of electroweak interactions is available. The measurement of $|V_{tb}|$ is an important element of this effort. Run II should yield a 10% measurement of this quantity. Strong constraints have been laid on potential $V + A$ couplings at the Wtb vertex. The top quark charge is already determined to be like its c and u brethren.

Direct searches of new physics in the production and decay of the top quark have yielded significant constraints. Techniques to look for charged Higgs Bosons in top quark decay have been refined as the calculational picture has improved. Limits are occupying an increasing fraction of the experimentally available parameter space. With the increased statistics, better limits of $t\bar{t}$ resonance production are being set, as well as on the presence of potential extra W' bosons in single top quark

production.

9.2. *Looking to the Future*

Many of the basic techniques described in this review can be used at the LHC, and there will be many new challenges. Instantaneous luminosities of 10× relative to the Tevatron, and $t\bar{t}$ cross sections 100× larger will provide a thousand-fold increase in statistical samples. This will allow, for instance, very large event samples with both $b-$jets identified. Early studies indicate that 1% precision in m_t measurement is accessible (e.g. Ref. 209). To achieve or surpass this level will require large, well-constrained samples. The top quark pair production and decay will be measurable across a wide array of channels. The measurements that will improve most dramatically are the other top quark properties, such as V_{tb} or W boson helicity. The searches for new physics will also gain considerable sensitivity from the ability to make precise analysis of the rates and kinematics of final state particles in top quark events.

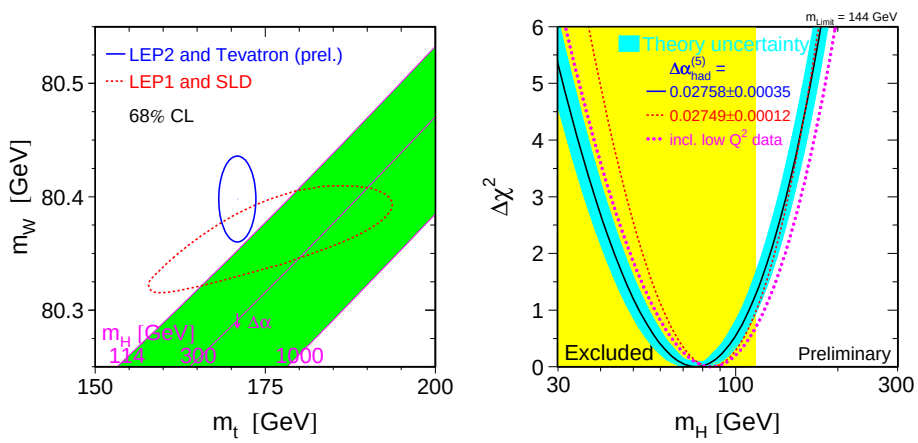

Fig. 54. The expected region of Higgs mass in the m_W vs. m_t plane (left). The combined Tevatron measurement of m_t (and m_W) are shown. Also shown is the fit to all electroweak data (right), in which the value of m_t provides substantial weight [125].

Finally, the study of the top quark is inextricably linked with the question of electroweak symmetry breaking and the Higgs mechanism. By including the measured value of m_t in the global electroweak fit one obtains the most stringent constraint on the mass of the Higgs boson. The preferred value for m_H is 76^{+33}_{-24} GeV[125], which is not favored by the $m_H > 114.7$ GeV limit from direct searches at LEP-II[160]. This result is shown in Fig. 54. The 95% confidence level upper limit on the Higgs boson mass set by this analysis is $m_H < 144$ GeV. It is interesting to consider the

measurements in relation to potential new physics. For example, Figure 55 indicates the regions in the m_W vs. m_t plane favored by MSSMs [210,211] and by the standard model. If current central values of m_W and m_t remain the same as more precise measurements are made, a signature of new physics may arise. In the standard model, improving the precision with which the top quark mass is measured will be a crucial ingredient in further tightening the constraints on the Higgs boson mass.

The most favored region provides for a complex set of Higgs boson production and decay processes. In this sense, the study of the Higgs boson has much in common with what confronted experimentalists for the top quark discovery. Final state channels including most of the objects identifiable at a hadron collider detector: $e, \gamma, \mu, \nu, jets, \tau$, and $b-$jets. This implies that the full range of experimental capabilities at the experiments will need to be mastered to maximize sensitivity. Multiple channels will be used to gain significance before any one channel sees a pristine signal. Decay chains include gauge bosons, and there are concurrent $W/Z + X$ backgrounds that go with this. Some of the modeling questions and background estimation approaches that have been important in study of the top quark will also be important for the Higgs boson search.

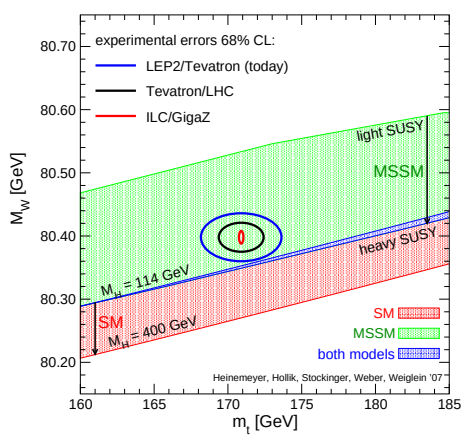

Fig. 55. Regions in m_W vs. m_t plane favored by MSSMs and by the standard model [210]. Anticipated sensitivities from future measurements are also shown.

One thing is clear, the race is on in earnest for the Higgs boson. Will the Tevatron have a shot at a signal? Will the LHC effort turn on rapidly and overwhelm the search quickly? Is there a Higgs mechanism at all, or are there new strong dynamics in its place which elevate the top quark to a more fundamental status. The study of the top quark lies at an important cross-roads in the pursuit of answers to these questions. We look forward with fascination to the chance to work with our colleagues in the coming years' study.

10. Acknowledgments

We sincerely thank the staff of Fermilab for providing a wonderful vehicle with which to study this new and fascinating particle. With gratitude, we thank our colleagues on CDF and DØ for the effort and experience they have shared in making the measurements described in this paper. We have benefited from the input of several colleagues in the drafting of this review. Special thanks go to Ulrich Heintz, Boaz Klima, Avto Kharchilava, Matteo Cacciari, Nikolaos Kidonakis, Lisa Shabalina, Florencia Canelli and Kirsten Tollefson for their thoughtful feedback on various aspects of this paper. Compilation of this review was funded in part by DE-FG02-O4ER41299 with Southern Methodist University, by DE-FG02-91ER40688 with Brown University and by NSF-0555632 with SUNY Buffalo.

References

1. DØ Collab. (S. Abachi et al.), *Phys. Rev. Lett.* **74**, 2632 (1995).
2. CDF Collab. (F. Abe et al.), *Phys. Rev. Lett.* **74**, 2626 (1995).
3. P. Bhat, H. Prosper and S. Snyder, "Top Quark Physics at the Tevatron", *Int. J. Mod. Phys.* A **13**, 5113 (1998).
4. D. Chakraborty, J. Konigsberg and D. Rainwater, "Top Quark Physics", *Ann. Rev. Nucl. Part. Sci.* **53**, 301 (2003).
5. S. Dawson, "The Top Quark, QCD and New Physics", Lect. given at TASI 2002 Summer School, U. of Colorado, Boulder, CO, June 2-28 (2002); **hep-ph/0303191**; **BNL-71205-2003-CP**.
6. W. Wagner, "Top Quark Physics in Hadron Collisions", *Rep. Prog. Phys.* **68**, 2409 (2005).
7. A. Salam, *Elementary Particle Physics* (Almqvist and Wiksells, Stockholm, 1968); S. Weinberg, *Phys. Rev. Lett.* **19**, 1264 (1967).
8. P. W. Higgs, *Phys. Lett.* **12**, 132 (1964); *Phy. Rev.* **145**, 1156 (1966). F. Englert and R. Brout, *Phys. Rev. Lett.* **13**, 321 (1964).
9. C. Quigg, *Gauge Theories of the Strong, Weak, and Electromagnetic Interactions* (Addison-Wesley, 1983).
10. M. Gell-Mann, *Phys. Lett.* **8**, 214 (1964); G. Zweig, *CERN Report*, 8182/Th.401, (1964).
11. R. D. Field and R. P. Feynman, *Nucl. Phys.* B **136**, 1 (1978); B. Andersson et al., *Phys. Rep.* **97**, 31 (1983).
12. M. Kobayashi and T. Maskawa, *Prog. Theor. Phys.* **49**, 652 (1973).
13. S. Glashow, J. Iliopolous and L. Maiani, *Phys. Rev.* D **2**, 1285 (1970).
14. M. L. Perl et al., *Phys. Rev. Lett.* **35**, 1489 (1975).
15. S. W. Herb et al., *Phys. Rev. Lett.* **39**, 252 (1977).
16. H. Geori and S. Glashow, *Nucl. Phys.* B **167**, 173 (1980)
17. G. Kane and M. Peskin, *Nucl. Phys.* B **195**, 29 (1982)
18. H. Georgi and A. Pais, *Phys. Rev.* D **19**, 2746 (1979)
19. J. Bjorken and K. Lane, in *Proc. of Int. Neutrino Conf.*, Baksan, 1977, ed. by M. Markov et al., (Nauka, Moscow, 1978).
20. F. Gursey, P. Raymond and P. Sikivie, *Phys. Lett.* B **60**, 177 (1976).
21. UA1 Collab. (A. Bean et al.), *Phys. Rev.* D **35**, 3533 (1987).
22. ARGUS Collab. (H. Albrecht et al.), *Phys. Lett.* B **192**, 245 (1987); CLEO Collab.(J. Bartelt et al.), *Phys. Rev. Lett.* B **71**, 1680 (1993).

23. E. Ma, *Phys. Rev. Lett.* **57**, 535 (1986).
24. Particle Data Group (K. Hagiwara et al.), *Phys. Rev.* D **66**, 010001 (2002).
25. JADE Collab. (E. Elsen et al.), *Z. Phys.* C **46**, 349 (1990); CELLO Collab. (H. Behrend et al.), *Z. Phys.* C **47**, 333 (1990); TOPAZ Collab. (A. Shimonaka et al.), *Phys. Lett.* B **268**, 457 (1991).
26. The LEP Electroweak Working Group, the SLD Electroweak and Heavy Flavor Groups, *Phys. Rep.* **427**, 257 (2006).
27. Review of Particle Properties, Particle Data Group,*Phys. Lett.* B **239**, VII 167 (1990).
28. UA1 Collab. (C. Albajar et al.), *Z. Phys.* C **37**, 505 (1988); *Z. Phys.* C **48**, 1 (1990).
29. UA2 Collab. (T. Akessan et al.), *Z. Phys.* C **46**, 179 (1990).
30. CDF Collab. (F. Abe et al.), *Phys. Rev. Lett.* **68**, 447 (1992); *Phys. Rev.* D **45**, 3921 (1992).
31. DØ Collab. (S. Abachi et al.), *Phys. Rev. Lett.* **724**, 2138 (1994).
32. T. M. P. Tait and C.-P. Yuan, *Phys. Rev.* D **63**, 014018 (2000).
33. J. C. Collins, D. E. Soper and G. Sterman, *Nucl. Phys.* B **263**, 37(1986).
34. H. M. Georgi et al., *Ann. Phys.* **114**, 273 (1978); L. M. Jones and H. W. Wyld, *Phys. Rev.* D **17**, 1782 (1978); M. Gluck, J. F. Owens and E. Reya, *Phys. Rev.* D **17**, 2324 (1978); J. Babcock, D. Sivers and S. Wolfram, *Phys. Rev.* D **18**, 162 (1978); K. Hagiwara and T. Yoshino, *Phys. Lett.* B **80**, 282 (1979); B. L. Combridge, *Nucl. Phys.* B **151**, 429 (1979); W. Beenakker et al., *Nucl. Phys.* B **411**, 343 (1994).
35. P. Nason, S. Dawson and R. Ellis, *Nucl. Phys.* B **303**, 607 (1988); W. Beenakkeret al., *Phys. Rev.* D **40**, 54 (1989).
36. W. Beenakker, et al., *Nucl. Phys.* B **351**, 507 (1991).
37. G. Sterman, *Nucl. Phys.* B **281**, 310 (1987).
38. S. Catani and L. Trentadue, *Nucl. Phys.* B **327**, 323 (1989); S. Catani and L. Trentadue, *Nucl. Phys.* B **353**, 183 (1991).
39. N. Kidonakis and G. Sterman, *Phys. Lett.* B **387**, 867 (1996); N. Kidonakis and G. Sterman, *Nucl. Phys.* B **505**, 321 (1997).
40. R. Bonciani, S. Catani, M. Mangano and P. Nason, *Nucl. Phys.* B **529**, 424 (1998).
41. M. Cacciari, et al., *J. High Energy Phys.* **04**, 068 (2004).
42. N. Kidonakis, F. Laenen, S. Moch, and R. Vogt, *Phys. Rev.* D **64**, 114001 (2001); N. Kidonakis, *Phys. Rev.* D **64**, 014009 (2001).
43. N. Kidonakis and R. Vogt,*Phys. Rev.* D **68**, 114014 (2003).
44. K. Lane and E. Eichten, *Phys. Lett.* B **352**, 382 (1995); *Phys. Lett.* B **433**, 96 (1998).
45. Z. Sullivan, *Phys. Rev.* D **70**, 114012 (2004).
46. N. Kidonakis,*Phys. Rev.* D **74**, 114012 (2006); N. Kidonakis, *Phys. Rev.* D **75**, 071501 (2007).
47. T. M. P. Tait, *Phys. Rev.* D **61**, 034001 (2000).
48. S.Eidelman et al., *Phys. Lett.* B **592**, 1 (2004).
49. M. Mangano et al., *J. High Energy Phys.* **07**, 001 (2003)
50. T. Sjostrand et al.,*Comput. Phys. Commun.* **135**, 238 (2001).
51. G. Marchesini et al., *Comput. Phys. Commun.* **67**, 465 (1992); G. Corcella et al., *J. High Energy Phys.* **01**, 010 (2001).
52. M. Mangano, *http://cepa.fnal.gov/patriot/mc4run2/MCTuning/061104/mlm.pdf* (2004).
53. S. Mrenna and P. Richardson, *J. High Energy Phys.* **05**, 040 (2004).
54. S. Catani et al., *J. High Energy Phys.* **0111**, 063 (2001); CERN-TH-2000-367 (2000).
55. S. Jadach et al., *Comp. Phys. Commun.* **76**, 361 (1993).
56. P. Avery, K. Read and G. Trahern, *CLEO Report* **CSN-212**, 1985 (unpublished).
57. H. T. Edwards, *Ann. Rev. Nucl. Part. Sci.* **35**, 605 (1985).

58. DØ Collab. (S. Abachi, et al.), *Nucl. Instrum. Meth.* A **338**, 185 (1994).
59. CDF. Collab. (J. Antos et al.), *Nucl. Instrum. Meth.* A **360**, 118 (1995).
60. CDF Collab. (C. Newman-Holmes et al.), The CDF Upgrade, *Fermilab-CONF-* **96-218-E**, 1996 (unpublished); R. Blair et al., Technical Design Report, *Fermilab-PUB-* **96-390-E**,1996 (unpublished).
61. DØ Collab. (V. Abazov et al.), The Upgraded D0 Detector, *Nucl. Instrum. Meth.* A **565**, 463 (2006).
62. DØ Collab. (V. Abazov, et al.), *FERMILAB-PUB-* **05-034-E** (2005).
63. CDF Collab.(F. Abe et al.), *Phys. Rev.* D **45**, 1448 (1992); G. C. Blazey et al., RunII Jet Physics, in *Proc. Workshop: QCD and Weak Boson Physics in RunII*, eds. U. Bauer, R. K. Ellis, D. Zappenfeld (FERMILAB-PUB-**00-297**, 2000).
64. DØ Collab.(B. Abbott et al.), *Phys. Rev. Lett.* **86**, 1707 (2001); *Nucl. Instrum. Methods Phys. Res. Sect.* A **424**, 352 (1999).
65. D. Lange, *Nucl. Instrum. Meth. Phys. Res.* A **462**, 152 (2001).
66. S. R. Slabopitsky, Event generators for top quark production and decays, in *Proc. Int. Workshop Top Quark Physics* (Coimbra, Portugal, 2006), Proc. of Sci. TOP2006:019, 2006, **hep-ph/0603124**.
67. M. Dobbs et al., Les Houches Guidebook to Monte Carlo Generators for Hadron Collider Physics, **hep-ph/0403045**.
68. E.E. Boos et al., *Phys. Atom. Nucl.* **69**, 1317 (2006).
69. CompHEP Collab. (E. Boos *et al.*), *Nucl. Instrum. Methods Phys. Res.* A **534**, 250 (2004).
70. T. Stelzer and W.F. Long, *Comput. Phys. Commun.* **81**, 337 (1994); F. Maltoni and T. Stelzer, *J. High Energy Phys.* **02**, 027 (2003).
71. R. Brun *et al.*, GEANT Detector Description and Simulation Tool, *CERN Program Library* **W5013** (1994).
72. V. Barger, J.Ohnemus and R. J.N. Phillips, *Phys. Rev.* D **48**, 3953 (1993).
73. DØ Collab. (V. Abazov et al.), *Phys. Lett.* B **626**, 55 (2005).
74. DØ Collab.(V. Abazov, et al.), *Phys. Rev.* D **67**, 012004 (2003); *Phys. Rev. Lett.* **79**, 1203 (1997).
75. LEP Electroweak Working Group: *http://lepewwg.web.cern.ch/LEPEWWG/plots/summer2005.*
76. CDF Collab. (D. Acosta et al.), *Phys. Rev. Lett.* **95**, 022001 (2005).
77. DØ Collab. (V. Abazov, et al.), *Phys. Rev.* D 76, 052006 (2007).
78. DØ Collab. (V. Abazov, et al.), *D0-CONF-5477* (2007); DØ Collab. (V. Abazov, et al.), *DØ -CONF-5465* (2007); DØ Collab. (V. Abazov, et al.), *DØ -CONF-5371* (2007).
79. CDF Collab. (D. Acosta et al.), *Phys. Rev. Lett.* **93**, 142001 (2004).
80. CDF Collab. (F. Abe et al.), *Phys. Rev. Lett.* **80**, 2773 (1998).
81. CDF Collab. (D. Acosta et al.), subm. to *Phys. Rev.* D Rapid. Comm. (2006).
82. CDF Collab. (D. Acosta et al.), in Proc. of Lepton-Photon Conf. (2007); *CDF-CONF-8802,8770.*
83. F. A. Berends et al., *Phys. Lett.* B **357**, 32 (1991).
84. DØ Collab. (V. Abazov, et al.), *DØ -CONF-5234* (2006).
85. J. C. Pati and A. Salam, *Phys. Rev.* D **10**, 275 (1974); R. N. Mohapatra and J. C. Pati, *Phys. Rev.* D **11**, 566 (1975); G. Senjanovic and R. N. Mohapatra, *Phys. Rev.* D **12**, 1502 (1975); T. G. Rizzo, *Phys. Rev.* D **25**, 1355 (1982);D **27**, 657(A) (1983).
86. CDF Collab., (D. Acosta, et al.), *Phys. Rev.* D **52**, 052003 (2005).
87. DØ Collab. (V. Abazov, et al.), *Phys. Lett.* B **626**, 45 (2005).
88. DØ Collab. (V. Abazov, et al.), *Phys. Rev.* D **76**, 092007 (2007).

89. DØ Collab. (V. Abazov, et al.), *DØ -CONF-5262* (2007).
90. F. Berends et al., *Nucl. Phys.* B **357**, 32 (1991).
91. CDF Collab. (T. Affolder, et al.), *Phys. Rev.* D **64**, 032002 (2001).
92. CDF Collab. (D. Acosta, et al.), *Phys. Rev.* D **72**, 032002 (2005).
93. CDF Collab. (D. Acosta, et al.), *CDF-CONF-8565* (2006).
94. DØ Collab. (R. Harrington), in *Proceedings of Lake Louise Winter Institute 2007* (Alberta, Canada, Feb 2007) World Scientific Publ. Co., Singapore, (in press).
95. CDF Collab. (D. Acosta, et al.), *Phys. Rev.* D **71**, 072005 (2005).
96. CDF Collab. (D. Acosta, et al.), *Phys. Rev.* D **71**, 052003 (2005).
97. CDF Collab. (D. Acosta, et al.), *Phys. Rev.* D **71**, 052003 (2005).
98. CDF Collab. (D. Acosta, et al.), *Phys. Rev.* D **71**, 052003 (2005).
99. CDF Collab. (D. Acosta, et al.), *CDF-CONF-8795*, (2007).
100. DØ Collab. (V. Abazov, et al.), *Phys. Lett.* B **626**, 35 (2005).
101. CDF Collab. (A. Abulencia, et al.), *Phys. Rev. Lett.* **97**, 082004 (2006).
102. CDF Collab. (A. Abulencia, et al.), *Phys. Rev.* D **74**, 072006 (2006).
103. DØ Collab. (V. Abazov et al.), *Phys. Rev.* D **74**, 112004 (2006).
104. DØ Collab. (V. Abazov et al.), *DØ -CONF-5355* (2007).
105. DØ Collab. (B. Abbott, et al.), *Phys. Rev. Lett.* **83**, 1908 (1999); *Phys. Rev.* D **60**, 012001 (1999).
106. CDF Collab. (F. Abe et al.), *Phys. Rev. Lett.* **79**, 1992 (1997).
107. CDF Collab. (D. Acosta et al.), *Phys. Rev.* D **74**, 072005 (2006).
108. DØ Collab. (V. Abazov et al.), *Phys. Rev.* D **76**, 072007 (2007).
109. R. Brun and F. Rademakers, *Nucl. Inst. Meth. in Phys. Res.* A **389**, 81 (1997).
110. DØ Collab. (V. Abazov et al.),**hep-ex/0612052**, acc. to *Phys. Rev. Lett.*.
111. DØ Collab. (V. Abazov et al.),**hep-ex/0604020**, subm. to *Phys. Rev.* D.
112. DØ Collab. (B. Abbott, et al.), *Phys. Rev. D Rapid Comm.* **63**, 031101 (2001); DØ Collab. (V. Abazov et al.), *Phys. Lett.* B **517**, 282 (2001).
113. CDF Collab. (D. Acosta et al.), Phys. Rev. D **65**, 091102 (2002); *Phys. Rev.* D **69**, 052003 (2004).
114. CDF Collab. (D. Acosta et al.), *Phys. Rev.* D **71**, 012005 (2005).
115. DØ Collab. (V. Abazov et al.), *Phys. Lett.* B **622**, 265 (2005).
116. E. Boos and L. Dudko, *Nucl. Instrum. Methods* A **502**, 486 (2003).
117. G. Mahlon and S. Parke, *Phys. Rev.* D **53**, 4886 (1996); S. Parke and Y. Shadmi, *Phys. Lett.* B **387**, 199 (1996); G. Mahlon and S. J. Parke, *Phys. Rev.* D **55**, 7249 (1997).
118. J. Schwindling, `http://schwind.home.cern.ch/schwind/MLPfit.html`.
119. M. Feindt, e-Print Archive physics/0402093 (2004).
120. L. Breiman *et al.*, *Classification and Regression Trees* (Wadsworth, Stamford, 1984).
121. Y. Freund and R.E. Schapire, in *Proceedings of the Thirteenth International Conference on Machine Learning*, ed. L. Saitta (Morgan Kaufmann, San Francisco, 1996), p. 148.
122. DØ , *Evidence for Single Top Quark Production and First Measurement of* —V_{tb}— presented on Dec 8th, 2006 at the Fermilab Joint Theory and Experimental Seminar.
123. R.M. Neal, *Bayesian Learning of Neural Networks* (Springer-Verlag, New York, 1996); Used "Software for Flexible Bayesian Modeling" package, `http://www.cs.toronto.edu/~radford/fbm.software.html`.
124. CDF Collab. (S. Leone), *Published Proceedings 15th International Conference on Supersymmetry and the Unification of Fundamental Interactions (SUSY07)*, (Karlsruhe, Germany, July 26-August 1, 2007), Librix Publishers, Budapest (in press),

FERMILAB-CONF-07-581-E.
125. DØ and CDF Collab. Top Quark Mass Combination, *The Tevatron Electroweak Working Group*, **hep-ex/0703034**; FERMILAB-TM-2380-E (2007).
126. S. Dimoupoulos and H. Georgi, *Nucl. Phys.* B **193**, 10 (1981).
127. CDF Collab. (F. Abe et al.), *Phys. Rev. Lett.* **80**, 2779 (1998).
128. DØ Collab. (B. Abbott, et al.), *Phys. Rev.* D **60**, 052001 (1999); *Phys. Rev. Lett.* **80**, 2063 (1998).
129. CDF Collab. (F. Abe et al.), *Phys. Rev. Lett.* **82**, 271 (1999).
130. CDF Collab. (A. Abulencia et al.), *Phys. Rev.* D **73**, 112006 (2006).
131. R. Dalitz and G. Goldstein, *Phys. Rev.* D **45**, 1531 (1992).
132. K. Kondo, *J. Phys. Soc. Jpn.* **57**, 4126 (1988); *J. Phys. Soc. Jpn.* **60**, 836 (1991).
133. CDF Collab. (A. Abulencia et al.), *Phys. Rev. Lett.* **96**, 152002 (2006); *Phys. Rev.* D **74**, 032009 (2006).
134. DØ Collab.(V. Abazov et al.), *Nature* **429**, 638 (2004).
135. DØ Collab.(V. Abazov, et al.), *Phys. Lett.* B, **655**, 7 (2007).
136. DØ Collab. (V. Abazov, et al.), *DØ -CONF-5347* (2007).
137. DØ Collab. (V. Abazov, et al.), *DØ -CONF-5171* (2006).
138. DØ Collab. (V. Abazov, et al.), *DØ -CONF-5463* (2007).
139. L. Holmstrom, R. Sain and H. E. Miettinen, *Comput. Phys. Commun.* **88**, 195 (1995).
140. CDF Collab. (A. Abulencia et al.), *Phys. Rev.* D **73**, 112006 (2006).
141. CDF Collab. (A. Abulencia, et al.), *Phys. Rev.* D **75**, 031105 (2007).
142. G. Mahlon and S. J. Parke, *Phys. Lett.* B **411**, 173 (1997).
143. "A Precision Measurement of the Top Quark Mass," K. M. Black, Ph.D. thesis, Boston University, Boston, USA, 2005.
144. CDF Collab. (A. Abulencia *et al.*), *Phys. Rev. Lett.* **96**, 022004 (2006).
145. CDF and DØ Collabs. (M. Zielinski), in *Proceedings of Physics at LHC* (Cracow, Poland, 2006), Acta Physica Polonica (2007), **hep-ex/0610017**.
146. DØ Collab. (S. Abachi, et al.), *Phys. Rev. Lett.* **79**, 1197 (1997);
DØ Collab. (B. Abbott, et al.), *Phys. Rev.* D **58**, 052001 (1998).
147. DØ Collab. (V. Abazov et al.), *Phys. Rev.* D **74**, 092005 (2006).
148. DØ Collab. (M. Wang),*Proceedings of 42nd Rencontres de Moriond on QCD and High Energy Hadronic Interactions*, (La Thuile, Aosta Valley, Italy, March 2007), The' Gioi Publishers (2007)..
149. CDF Collab. (E. Brubaker), in *Proceedings 41st Rencontres de Moriond on Electroweak Interactions and Unified Theories* (La Thuile, Aosta Valley, Italy, March 11-18, 2006), The' Gioi Publishers (2006), FERMILAB-CONF-06-124-E..
150. K. Kondo, Waseda University, *RISE Technical Report* **No.05-01** (2005), **hep-ex/0508035**.
151. CDF Collab. (A. Abulencia, et al.), *Phys. Rev.* D **73**, 092002 (2006).
152. DØ Collab. (V. Abazov et al.), *Phys. Rev.* D **75**, 092001 (2007); FERMILAB-PUB-07/039-E.
153. DELPHI Collab. (P. Abreu et al.), *Eur. Phys. J.* C **2**, 581 (1998); *Phys. Lett.* B **462**, 410 (1999); *Phys. Lett.* B **511**, 159 (2001); M. Mulders, *Ph.D. thesis* (FOM, Amsterdam & Amsterdam U.), Sep 2001, 226pp.
154. CDF Collab. (A. Abulencia et al.), *Phys. Rev.* D **75**, 071102 (2007);
155. CDF Collab. (A. Abulencia, et al.), *Phys. Rev.* D 76, 072009 (2007).
156. DØ Collab. (V. Abazov et al.), *Phys. Lett.* B **606**, 25 (2005).
157. CDF Collab. (A. Abulencia, et al.), *Phys. Rev. Let.* 98, 142001 (2007).
158. CDF Collab. (A. Abulencia, et al.), *CDF-CONF-8709* (2007).
159. *The LEP Electroweak Working Group*, LEPEWWG/2006-01,

http://lepewwg.web.cern.ch/LEPEWWG/stanmod/summer2006/s06.ew.ps.gz.
160. The LEP Working Group for Higgs Boson Searches*Phys. Lett.* B **565**, 61 (2003).
161. G. Kane, C.-P. Yuan, and G. Ladinsky, *Phys. Rev.* D **45**, 124, (1992).
162. CDF Collab. (D. Acosta et al.), *Phys. Rev.* D **71**, 031101(R) (2005)
163. CDF Collab. (T. Affolder et al.), *Phys. Rev. Lett.* **84**, 216 (2000)
164. CDF Collab. (A. Abulencia et al.), *Phys. Rev.* D **73**, 111103(R) (2006)
165. CDF Collab. (A. Abulencia et al.), *Phys. Rev. Lett.* **98**, 072001 (2007)
166. DØ Collab.(V. Abazov et al.), *Phys. Rev.* D **75**, 031102(R) (2007).
167. DØ Collab.(V. Abazov et al.), *Phys. Rev.* D **72**, 011104(R) (2005).
168. DØ Collab.(V. Abazov et al.), subm. to *Phys. Rev. Lett.*(2007); FERMILAB-PUB-07/588-E.
169. G.Eilam, J.L.Hewett, A.Soni, *Phys. Rev.* D **44**, 1473 (1991).
170. CDF Collab. (T. Affolder et al.), *Phys. Rev. Lett.* **86**, 3233 (2001).
171. CDF Collab.(D. Acosta et al.) , *Phys. Rev. Lett.* 95, 102002 (2005).
172. DØ Collab. (V. Abazov et al.), *Phys. Lett.* B **639**, 616 (2006).
173. DØ Collab. (V. Abazov, et al.), subm. to *Phys. Rev. Lett.*; FERMILAB-PUB-08-010-E, hep-ex/0801.1326.
174. D. Chang, W. Chang, and E. Ma, *Phy. Rev.* D **59**, 091503 (1999); **61**, 037301 (2000); D. Choudhary, T. M. Tait and C. E. Wagner, *Phy. Rev.* D **65**, 053002 (2005).
175. U. Baur, M. Buice and L. H. Orr, *Phy. Rev.* D **64**, 094019 (2001).
176. DØ Collab. (V. Abazov et al.), *Phys. Rev. Lett.* **98**, 041801 (2007).
177. C. T. Hill, *Phys. Lett.* B **345**, 483 (1995).
178. S. Weinberg, *Phys. Rev.* D **13**, 974 (1976); L. Susskind, *Phys. Rev.* D **20**, 2619 (1979); S. Dimopoulos and L. Susskind, *Nucl. Phys.* B **155**, 237 (1979); E. Eichten and K. Lane, *Phys. Lett.* B **90**, 125 (1980).
179. CDF Collab. (T. Affolder et al.), *Phys. Rev. Lett.* **85**, 2062 (2000).
180. DØ Collab. (V. Abazov et al.), *Phys. Rev. Lett.* **92**, 221801 (2004).
181. I. Bertram *et al.*, *FERMILAB-TM-* **2104** (2000).
182. DØ Collab. (C. Schwanenberger), in *Proceedings of International Europhysics Conference on High Energy Physics* (Lisboa, Portugal, 2005), Proc. of Sci. (2006), hep-ex/0602048.
183. DØ Collab. (V. Abazov, et al.), D0-CONF-5443 (2007).
184. CDF Collab. (A. Abulencia, et al.), subm. to *Phys. Rev. Lett.*, **hep-ex/0709.0705** (2007).
185. CDF Collab. (A. Abulencia, et al.), subm. to *Phys. Rev. D*, **hep-ex/0710.5335** (2007).
186. M. S. Alam et al., *Phys. Rev. Lett.* **74**, 2885 (1995).
187. S. Towers, submitted to *Phys. Lett.* B, **hep-ex/0004022**.
188. LEP Higgs Working Group, *LHWG Note* **2001-05**.
189. CDF Collab. (F. Abe, et al.), *Phys. Rev. Lett.* **79**, 357 (1997).
190. J. Coarasa, J. Guasch and J. Sola, *Preprint UAB-FT-451*, (1998); talk presented at IVth Intl. Symp. on Rad. Corr. (RADCOR), Barcelona, Sep. 8-12, 1998; **hep-ph/9903212**.
191. M. Carena, D. Garcia, U. Nierste and C. Wagner, *Nucl. Phys.* B **577**, 88 (2000).
192. CDF Collab. (T. Affolder, et al.), *Phy. Rev.* D **62**, 012004 (2000).
193. DØ Collab. (V. Abazov et al.), *Phys. Rev. Lett.* **88**, 151803 (2002).
194. JETNET package, http://www.thep.lu.se/public_html/jetnet_30_manual/jetnet_30_manual.html.
195. DØ Collab. (B. Abbott, et al.), *Phys. Rev. Lett.* **82**, 4975 (1999).
196. CDF Collab. (A. Abulencia et al.), *Phys. Rev. Lett.* **96**, 042003 (2006).

197. J. Lee et al.,*Comput. Phys. Commun.* **156**, 283 (2004).
198. Z. Sullivan, *Phys. Rev.* D **66**, 075011 (2002).
199. P. Langacker and S.U. Shankar, *Phys. Rev.* D **40**, 1569 (1989) and references therein.
200. CDF Collab. (T. Affolder et al.), *Phys. Rev. Lett.* **87**, 231803 (2001).
201. DØ Collab. (S. Abachi et al.), *Phys. Rev. Lett.* **76**, 3271 (1996).
202. CDF Collab. (F. Abe et al.), *Phys. Rev. Lett.* **84**, 5716 (2000).
203. UA2 Collab. (J. Alitti et al.), *Nucl. Phys.* B **400**, 3 (1993).
204. CDF Collab. (F. Abe et al.), *Phys. Rev.* D **55**, 5263 (1997).
205. DØ Collab. (V. Abazov et al.), *Phys. Rev.* D **69**, 111101 (2004).
206. CDF Collab. (D. Acosta et al.), *Phys. Rev. Lett.* **90**, 081802 (2003).
207. DØ Collab. (V. Abazov et al.), *Phys. Lett.* B **641**, 423 (2006).
208. CDF and DØ collab. (M. Datta), in *Proceedings of Hadron Collider Physics Symposium 2007* (La Biodola, Isola d'Elba, Italy, May 2007) Elsevier, Nucl. Phys. B: Proc. Suppl. (in press).
209. ATLAS Collab., ATLAS-TDR-15, CERN/LHCC/99-15 (1999).
210. S. Heinemeyer, W. Hollik, D. Stockinger, A.M. Weber and G. Weiglein, Journ. of High Energy Phys. 0608:052, (2006); S. Heinemeyer, W. Hollik and G. Weiglein, Phys. Rept. 425, 265 (2006).
211. A. Djouadi, P. Gambino, S. Heinemeyer, W. Hollik, C. Jnger and G. Weiglein, Phys. Rev. Lett. 78, 3626 (1997); Phys. Rev. D 57, 4179 (1998); S. Heinemeyer, G. Weiglein, JHEP 10, 072 (2002); J. Haestier, S. Heinemeyer, D. Stockinger and G. Weiglein, J. High Energy Phys. 12, 027 (2005).